



UCGE Reports
Number 20250

Department of Geomatics Engineering

Wavelet Representation of Geodetic Operators
(URL:<http://www.geomatics.ucalgary.ca/research/publications/GradTheses.html>)

by

Mohamed Mamdouh Elhabiby

January 2007



UNIVERSITY OF CALGARY

Wavelet Representation of Geodetic Operators

by

Mohamed Mamdouh Elhabiby

A THESIS

SUBMITTED TO THE FACULTY OF GRADUATE STUDIES
IN PARTIAL FULFILMENT OF THE REQUIREMENTS FOR THE
DEGREE OF DOCTOR OF PHILOSOPHY

DEPARTMENT OF GEOMATICS ENGINEERING
CALGARY, ALBERTA
JANUARY, 2007

© MOHAMED MAMDOUH ELHABIBY 2007

Abstract

The main objective of this research is to introduce an alternative to the FFT computational scheme using the wavelet transform for the numerical evaluation of different geodetic operators. The new wavelet representation is built on orthogonal wavelet base functions. Eight geodetic operators are evaluated in this thesis: they are classified into direct geodetic integrals, inverse geodetic integrals, and the inversion of integrals. The direct geodetic integrals are the Stokes, the Vening Meinesz, the Poisson (upward continuation), and the terrain correction integrals. The inverse geodetic integrals are the inverse Vening Meinesz integral and the deflection-geoid formula. The Stokes and Poisson (downward continuation) integrals are inverted in the wavelet domain by a conjugate gradient method.

In each case, the role of the kernel's singularity in the wavelet multi-resolution analysis is studied. The integrals are approximated in finite multi-resolution analysis subspaces. A new implementation is introduced to decrease the computational effort. The full solution with all equations requires a large computer memory. Multi-resolution properties of the wavelet transform are used to divide the full solution into parts. Each part represents a level of wavelet detail coefficients or the approximation coefficients. Hard thresholding is used for the compression of the kernels' wavelet detail coefficients. Global fixed thresholding and level/direction-wise thresholding is tested for different kernels. High compression levels are achieved with an acceptable accuracy, which leads to large savings in computer memory and storage space required for allocating the matrices, and also the ability to work with sparse matrices. In the case of the inversion of the integrals, a set of equations is formed and solved using an iterative gradient method. Soft thresholding is used for de-noising stationary and non-stationary noise because of its smoothing properties. Conclusions and recommendations are given with respect to the suitability, accuracy, and efficiency of these methods.

Preface

This is an unaltered version of the author's Doctor of Philosophy thesis of the same title. This thesis was accepted by the Faculty of Graduate Studies in December, 2006. The faculty supervisor of this work was Dr. M.G. Sideris and the other members of the examining committee were Dr. Nico Sneeuw, Dr. N. El-Sheimy, Dr. Abu Sesay, and Dr. C. K. Shum.

Acknowledgements

I would like to express my gratitude to my distinguished supervisor, Professor Dr. Michael Sideris, for his professional supervision, unwavering support, guidance, vision, proposed ideas and constructive suggestions during my graduate studies. His abundant cooperation, positive attitude, and understanding deserve everlasting appreciation. It was my deep pleasure to work under his supervision.

I wish to extend my appreciation and thanks to my supervising committee Professor Dr. Nico Sneeuw and Professor Dr. Naser El-Sheimy for their time, valuable support and discussions.

The work and thorough proofreading of Dr. Abu Sesay and Dr. C.K. Shum, the two other members of the examining committee, is also highly appreciated.

I would like to acknowledge Professor Dr. Wolfgang Keller and Professor Dr. Rod Blais for the beneficial guidance, advice and last long cooperation.

I would also like to thank deeply Dr. Alex Braun for the constructive discussions and assistance. Special thanks to Dr. Ahmed Osman for his advice and recommendations during the early stages of my research. I would like to thank Professor Dr. Will Featherstone for providing the synthetic data.

Many thanks go to all my colleagues in the gravity research group for the amazing time, friendship, and support for more than four years: Dr. Georgia Fotopoulos, Bihter, Dr. Claudia Tocho, Dr. Rossen Grebenitcharsky, Matthias, Chen, Balaji, Wouter, Elena, Vidya, Raymond, Daboor, and Ibrahim. My work and rich discussions with them were always a pleasure that created an ideal working environment. I would like to thank my dear friend Matthias for the cooperation and the moments we shared during writing our theses and the celebration of our success.

I would like to thank the entire faculty and staff members of the Geomatics department, Schulich School of Engineering for providing a wonderful educational environment.

Also, I would like to thank all the faculty and staff members of the Surveying group, Public Works department, Ain Shams University for their continuous support.

This research was funded in part by the Natural Sciences and Engineering Research council of Canada (NSERC) and The GEOimatic for Informed Decisions (GEOIDE) Canadian Centres of Excellences project grants of my supervisor. The Department of Geomatics Engineering Graduate Scholarships and travel grants, Special awards, C. F. Gauss award, F. R. Helmert award, and the University of Calgary Travel Grants.

I would like to express my sincere thanks to Dr. Sameh Nassar, Taher Hassan, Dr. Mohamed Abdelsalam, Dr. Walid Noureldin, Mahmoud El-Gizawy, Cecile Mongredien, Surendran, Katrin Zorn, Hatem Ibrahim, and Nora Ragab for their true friendship.

I owe all kinds of obligations to my beloved parents Mobshera and Mamdouh for their unlimited support, love, encouragement, and their faith in my dreams and me. My lovely parents I owe you everything I have achieved. My brothers, Mahmoud and Mostafa, you are my backbone; thank you very much for your unlimited support and congratulations.

My great wife Soha, I love you. Thank you very much for coming with me to Calgary and for your faith in me and for all the troubles, sacrifice, and hardships you took in order to help me in fulfilling my dreams. Your help and support cannot be described by words; you are always great as usual. My lovely twins Maged and Mazen, if life has a meaning this is because of you. I love you so much.

Dedication

To

My Parents, My Wife and My Sons

“Thank you”

Table of Contents

Approval Page.....	ii
Abstract.....	iii
Preface.....	iv
Acknowledgements.....	v
Dedication.....	vii
Table of Contents.....	viii
List of Tables.....	xi
List of Figures.....	xiii
List of Symbols.....	xix
CHAPTER ONE: INTRODUCTION.....	1
1.1 Background and motivation.....	1
1.2 Thesis objectives.....	4
1.3 Thesis outline.....	5
CHAPTER TWO: OVERVIEW OF IMPORTANT GEODETIC INTEGRALS.....	7
2.1 Regional geoid and deflection modeling.....	7
2.1.1 The Stokes integral.....	7
2.1.2 The Vening Meinesz integral.....	9
2.1.3 Terrain corrections integral.....	10
2.2 The Poisson integral for airborne gravimetry.....	13
2.3 Satellite altimetry integrals.....	14
2.3.1 Inverse Vening Meinesz' integral.....	14
2.3.2 Deflection-geoid formula.....	15
2.3.3 Inverting the Stokes integral.....	16
2.4 Summary.....	16
CHAPTER THREE: FUNDAMENTALS OF WAVELET TRANSFORM AND MULTI-RESOLUTION ANALYSIS.....	18
3.1 Overview of the Fourier transform and its convolution property.....	19
3.2 The wavelet transform.....	24
3.2.1 Continuous wavelet transform.....	24
3.2.2 Discrete wavelet transform.....	25
3.2.3 Multi-resolution analysis on wavelet basis.....	27
3.3 Wavelet thresholding.....	32
3.3.1 Hard thresholding compression.....	32
3.3.2 Soft thresholding de-noising.....	34
3.4 Standard and non-standard wavelet representation of operators.....	35
3.5 Implementation of the wavelet algorithm for geodetic integrals.....	36
3.6 Methodology of investigation.....	41
3.7 Summary.....	43
CHAPTER FOUR: APPLICATIONS OF WAVELETS AS ANALYSIS, COMPRESSION, AND DE-NOISING TOOLS.....	45
4.1 Selection of compactly supported orthogonal wavelets.....	45

4.2	Examples of analysis and localization properties	47
4.2.1	One-dimensional analysis of airborne gravimetry data	48
4.2.2	Two-dimensional analysis of Stokes's kernel and non-stationary noise	50
4.3	Examples of hard thresholding compression	53
4.3.1	Global fixed thresholding for kernel compression	54
4.3.2	Level/direction-wise thresholding	57
4.4	Examples of soft thresholding de-noising	58
4.4.1	One-dimensional de-noising of airborne gravity data	58
4.4.2	Two-dimensional de-noising of geoid undulations	60
4.4.2.1	Stationary noise	60
4.4.2.2	Non-stationary noise	62
4.5	Summary	63
CHAPTER FIVE: WAVELET EVALUATION OF DIRECT GEODETIC INTEGRALS		65
5.1	Evaluation of the Stokes integral	65
5.1.1	Data and wavelet used	66
5.1.2	Wavelet full matrix solution	66
5.1.3	Wavelet global fixed thresholding solution	70
5.1.4	Level/direction-wise thresholding solution	74
5.2	Evaluation of the Vening Meinesz integral	76
5.2.1	Data and wavelet used	76
5.2.2	Wavelet full matrix solution	77
5.2.3	Wavelet global fixed thresholding solution	79
5.2.4	Level/direction-wise thresholding solution	82
5.3	Evaluation of the terrain correction integral	84
5.3.1	Data and wavelet used	85
5.3.2	Wavelet full matrix solution	85
5.3.3	Wavelet global fixed thresholding solution	87
5.3.4	Level/direction-wise thresholding solution	87
5.4	Evaluation of the upward continuation integral	92
5.4.1	Data and wavelet used	92
5.4.2	Wavelet full matrix solution	93
5.4.3	Wavelet global fixed thresholding solution	94
5.4.4	Level/direction-wise thresholding solution	98
5.5	Summary	100
CHAPTER SIX: WAVELET EVALUATION OF INVERSE GEODETIC PROBLEMS		102
6.1	Evaluation of the inverse geodetic integrals	102
6.1.1	Evaluation of the inverse Vening Meinesz integral	102
6.1.1.1	Wavelet full matrix solution	103
6.1.1.2	Wavelet global fixed thresholding solution	105
6.1.1.3	Level/direction-wise thresholding solution	107
6.1.2	Evaluation of the deflection-geoid formula	109
6.1.2.1	Wavelet full matrix solution	109
6.1.2.2	Wavelet global fixed thresholding solution	111

6.1.2.3 Level/direction-wise thresholding solution	115
6.2 Inversion of geodetic integrals.....	117
6.2.1 Wavelet inversion of the Stokes integral.....	117
6.2.1.1 Wavelet full matrix solution	117
6.2.1.2 Wavelet global fixed thresholding solution	118
6.2.1.3 Wavelet as a regularization tool.....	121
6.2.2 Wavelet inversion of the Poisson's integral (downward continuation).....	124
6.2.2.1 Wavelet full matrix solution	125
6.2.2.2 Wavelet global fixed thresholding solution	127
6.3 Summary.....	130
CHAPTER SEVEN: CONCLUSIONS AND RECOMMENDATIONS	133
7.1 Summary	133
7.2 Conclusions.....	135
7.3 Recommendations and open problems	137
REFERENCES	140

List of Tables

Table 4.1: Estimated thresholding values (automated global fixed thresholding).....	55
Table 4.2: Estimated thresholding values (automated global fixed thresholding) for different gird spacings.....	56
Table 5.1: Wavelet global thresholding versus wavelet full matrix solution for the Stokes integral.....	71
Table 5.2: Level/direction-wise for case (c) global thresholding	75
Table 5.3: Level/direction-wise for case (d) global thresholding	75
Table 5.4: Wavelet global fixed thresholding versus wavelet full matrix solution for the vertical component of the deflection of the vertical.....	82
Table 5.5: Level/direction-wise for case (a) global thresholding	83
Table 5.6: Level/direction-wise for case (b) global thresholding	83
Table 5.7: Level/direction-wise for case (c) global thresholding	83
Table 5.8: Level/direction-wise for case (d) global thresholding	83
Table 5.9: Height statistics.....	85
Table 5.10: Wavelet global thresholding solutions versus wavelet full matrix solution for the terrain correction integral	88
Table 5.11: Level/direction-wise for case (c) global thresholding	90
Table 5.12: Level/direction-wise for case (e) global thresholding	90
Table 5.13: Level/direction-wise for case (f) global thresholding.....	90
Table 5.14: Wavelet global fixed thresholding versus wavelet full matrix solution for the evaluation of the upward continuation integral.....	97
Table 5.15 Level/direction-wise for case (a) global thresholding	99
Table 5.16: Level/direction-wise for case (d) global thresholding	100
Table 6.1: Wavelet global fixed thresholding versus wavelet full matrix solution for the inverse Vening Meinesz integral.....	107
Table 6.2: Level/direction-wise for case (a) global thresholding	107
Table 6.3: Level/direction-wise for case (d) global thresholding	109

Table 6.4: Wavelet global fixed thresholding versus wavelet full matrix solution for the deflection-geoid formula.....	115
Table 6.5: Level/direction-wise for case (a) global thresholding	116
Table 6.6: Level/direction-wise for case (d) global thresholding.....	116
Table 6.7: Global thresholding versus full matrix solution for the inversion of the Stokes integral.....	121
Table 6.8: Wavelet global fixed thresholding versus wavelet full matrix solution for the evaluation of the downward continuation operator.....	130

List of Figures

Figure 3.1: Windowed Fourier transforms [after Robertson et al., 1996]	23
Figure 3.2: Discrete wavelet Transform [after Griffiths et al., 1997].....	26
Figure 3.3: Multi-resolution analysis using nested sequence	27
Figure 3.4: Low and high pass wavelet filters	28
Figure 3.5: Block diagram of the one-dimensional wavelet decomposition	29
Figure 3.6: One level of decomposition of the two-dimensional wavelet transform of a grid of data	31
Figure 3.7: Block diagram of the two-dimensional wavelet decomposition algorithm....	31
Figure 3.8: Hard thresholding.....	33
Figure 3.9 Soft thresholding	35
Figure 3.10: The structure of the row vector representing each kernel required for the design matrix A	41
Figure 3.11: The structure of the column vector a_j representing the wavelet coefficients matrix of the data q	42
Figure 3.12: Methodology of investigation	43
Figure 4.1: Daubechies wavelets (db): scaling function (red) and wavelet function (blue).....	46
Figure 4.2: Meyer scaling function (red) and wavelet (blue).	47
Figure 4.3: Flight pattern for the second day of the University of Calgary test over the Rocky Mountains	48
Figure 4.4: Gravity disturbance with 1 Hz sampling rate.....	49
Figure 4.5: FFT spectrum shows number of undesired frequencies.....	49
Figure 4.6: Time-frequency analysis and localization using continuous wavelet transform [after Elhabiby and Sideris, 2006b].....	50
Figure 4.7: Stokes kernel in the space domain	51
Figure 4.8: Stokes kernel in the wavelet domain (db4) at four levels of decompositions	51

Figure 4.9: Simulated non-stationary noise (left) and geoid undulation after the addition of the noise (right).....	52
Figure 4.10: Two-dimensional wavelet decomposition of the noisy geoid undulations ..	52
Figure 4.11: Global fixed thresholding for Stokes, deflection-geoid, terrain correction, and Vening Meinesz kernels	55
Table 4.3: Estimated thresholding values (automated global fixed thresholding) for different grid sizes.....	56
Figure 4.12: level/direction-wise thresholding [Elhabiby and Sideris, 2006a]	58
Figure 4.13: Difference between reference data and wavelet de-noising output [Elhabiby and Sideris, 2006b].....	59
Figure 4.14: Difference between reference data and 90s low pass filter output.....	59
Figure 4.15: Difference between reference data and 120s low pass filter output.....	59
Figure 4.16: Simulated stationary random noise	60
Figure 4.17: Contaminated geoid undulations by simulated stationary random noise.....	61
Figure 4.18: De-noised geoid undulations by soft thresholding.....	61
Figure 4.19: Difference between de-noised geoid undulations and original data.....	62
Figure 4.20: Difference between recovered geoid undulations after de-noising and the reference data	62
Figure 5.1: Synthetic gravity anomalies and geoid undulations over Greece and Italy ...	66
Figure 5.2: The two-dimensional wavelet transform of the gravity anomalies using db4 with four levels of decomposition.....	67
Figure 5.3: The two-dimensional wavelet transform of the centre point Stokes kernel of the gridded data using db4 with four levels of decomposition.....	67
Figure 5.4: Stokes kernels' A design matrix (unitless)	68
Figure 5.5: Wavelet full matrix solution for the Stokes integral	68
Figure 5.6: FFT and wavelet full matrix solutions in comparison to reference data for the Stokes integral.....	69
Figure 5.7: Difference between wavelet full matrix solution and the numerical integration solution for the Stokes integral.....	70

Figure 5.8: Design matrix A with 1.5×10^{-7} global thresholding value; each blue spot represents a nonzero value in the Stokes kernel.	71
Figure 5.9: Difference between the wavelet global thresholding (1.5×10^{-7}) solution and the numerical integration solution for the Stokes integral	72
Figure 5.10: A matrix at four thresholding values (1.5×10^{-6} , 1.5×10^{-5} , 1.5×10^{-4} , and 1.5×10^{-3}); each blue spot represents a nonzero value in the Stokes kernel.....	72
Figure 5.11 : Wavelet global fixed thresholding solution in comparison to the numerical integration solution for the Stokes integral.....	73
Figure 5.12: Global fixed thresholding versus level/direction-wise thresholding for the Stokes integral.....	76
Figure 5.13: Synthetic horizontal and vertical components of the deflection of the vertical over Greece and Italy	77
Figure 5.14: Vening Meinesz kernels' A design matrix (unitless).....	78
Figure 5.15: Difference of horizontal component (left) and vertical component (right) wavelet full matrix solution from the reference data	78
Figure 5.16: Difference between wavelet full matrix solution and numerical integration solution for horizontal and vertical component of the deflection of the vertical.....	79
Figure 5.17: The difference between the global thresholding solution and numerical integration solution for the vertical component of the Vening Meinesz integral	80
Figure 5.18: A matrix at four thresholding values (7.2×10^{-12} , 7.2×10^{-11} , 7.2×10^{-10} , and 7.2×10^{-9}); each blue spot represents a nonzero value in the Vening Meinesz kernel.....	80
Figure 5.19: Wavelet global fixed thresholding solution for the vertical component of the deflection of the vertical in comparison to the numerical integration solution ..	81
Figure 5.20: Global fixed thresholding versus level/direction-wise thresholding for the Vening Meinesz integral (vertical component).....	84
Figure 5.21: Point heights (m)	85
Figure 5.22: Wavelet full matrix solution of the terrain correction integral.....	86
Figure 5.23: Difference between wavelet full matrix solution and the numerical integration solution for the terrain correction integral.....	86
Figure 5.24: Difference between wavelet global thresholding and numerical integration solution for the terrain correction	88

Figure 5.25: A matrix at six thresholding values (6.7×10^{-6} , 6.7×10^{-5} , 6.7×10^{-4} , 6.7×10^{-3} , 6.7×10^{-2} and 6.7×10^{-1}); each blue spot represents a nonzero value in the terrain correction kernel.	89
Figure 5.26: Wavelet global thresholding fixed solution in comparison to numerical integration solution for the terrain correction integral.....	91
Figure 5.27: Global fixed thresholding versus level/direction-wise thresholding for the terrain correction integral.....	92
Figure 5.28: Gravity disturbances at the Kananaskis region at 4370 m (up) and 7288 m (down) altitudes.	93
Figure 5.29: Poisson kernels' A design matrix (unitless)	94
Figure 5.30: Wavelet full matrix solution for upward continuation (Poisson integral) from 4370 m to 7288 m	95
Figure 5.31: Wavelet full matrix solution differences from reference data (up) and numerical integration solution (down).....	95
Figure 5.32: Design matrix A of the global thresholding values (6.3×10^{-8}); each blue spot represents a nonzero value for the upward continuation integral.....	96
Figure 5.33: Global hard thresholding solution (up) and difference from numerical integration solution (down) for the upward continuation integral.....	96
Figure 5.34: A matrix at different thresholding values (6.3×10^{-7} , 6.3×10^{-6} , 6.3×10^{-5} , and 6.3×10^{-4}); each blue spot represents a nonzero value in the Poisson kernel.	97
Figure 5.35: Global thresholding solutions at four compression levels in comparison to the numerical integration solution for the upward continuation integral.....	98
Figure 5.36: Global fixed thresholding versus level/direction-wise thresholding for the evaluation of the upward continuation integral.....	99
Figure 6.1: Inverse Vening Meinesz kernels' A design matrix (vertical component)	103
Figure 6.2: Wavelet full matrix solution of the inverse Vening Meinesz integral	104
Figure 6.3: Wavelet full matrix solution differences from and the reference data (left) and the numerical integration solution (right) for the inverse Vening Meinesz integral	105
Figure 6.4: The wavelet global fixed thresholding solution with 76% compression (left) and the difference from the numerical integration solution (right) for the inverse Vening Meinesz integral	106

Figure 6.5: The difference between the wavelet global fixed thresholding solutions and numerical integration solution for the inverse Vening Meinesz integral.....	108
Figure 6.6: Global fixed thresholding versus level/direction-wise thresholding for the evaluation of the inverse Vening Meinesz integral.....	109
Figure 6.7: Deflection-geoid kernels' A design matrix.....	110
Figure 6.8: Wavelet full matrix solution of the deflection-geoid formula.....	110
Figure 6.9: Difference between wavelet full matrix solution and the reference data (left), and numerical integration solution (right) for the deflection-geoid formula	111
Figure 6.10: Design matrix A of the global fixed thresholding (0.12); each blue spot represents a nonzero value in the vertical component kernel (deflection-geoid) ...	112
Figure 6.11: Difference between wavelet global fixed solution and numerical integration solution for the deflection-geoid formula.....	112
Figure 6.12: A matrix at four different thresholding values (1.23, 12.3, 123.3, and 1233.5); each blue spot represents a nonzero value in the vertical component kernel.....	113
Figure 6.13: The difference between the wavelet global fixed thresholding and numerical integration solutions for the deflection-geoid formula	114
Figure 6.14: Global fixed thresholding versus level/direction-wise thresholding for the deflection-geoid formula.....	116
Figure 6.15: Wavelet full matrix solution for the inversion of the Stokes integral (left) and the difference from the reference data (right)	118
Figure 6.16: Global fixed thresholding wavelet solution (left) and difference from reference data (right) for the inversion of the Stokes integral	119
Figure 6.17: Conjugate gradient iterations versus relative residuals (inversion of the Stokes integral)	119
Figure 6.18: The difference between the wavelet global fixed thresholding and reference data for the inversion of the Stokes integral.....	120
Figure 6.19: Difference between the solution from the noisy geoid undulations (stationary) and the reference data for the inversion of the Stokes integral	122
Figure 6.20: Difference between the solution from the de-noised geoid undulations (stationary) and the reference data for the inversion of the Stokes integral	122
Figure 6.21: Inversion of the Stokes integral with non-stationary noise	123

Figure 6.22: Inversion of the Stokes integral after de-noising the non-stationary noise	124
Figure 6.23: The wavelet full matrix inversion of the Poisson integral (downward continuation) before regularization (up) and after regularization (down)	125
Figure 6.24: L-curve of the normal matrix for the choice of the optimal regularization parameter	126
Figure 6.25: Wavelet full matrix regularized solution for the downward continuation operator	127
Figure 6.26: Difference between regularized global fixed solution and reference data for the downward continuation operator	128
Figure 6.27: Conjugate gradient iterations versus relative residuals for the inversion of Poisson integral (downward continuation)	128
Figure 6.28 The difference between the regularized wavelet global fixed thresholding solutions and reference data for the downward continuation operator	129

List of Symbols

Symbol	Definition
T	Disturbing potential
P	Computational point
Δg	Gravity anomalies
ψ	Spherical distance
α	Spherical azimuth
N	Geoid undulation
$S(\psi)$	Stokes function
R	Mean radius of the Earth.
s	Planar distance
E	Limited area
Δx and Δy	Grid spacing
x, y	Cartesian coordinates
K_N	Stokes integral kernel
ξ, η	Two components of the deflection of the vertical
K_ξ, K_η	Two components of the deflection of the vertical kernels
ρ	mean density of the topographic masses
h_{\max}	Highest topographic elevation
c	Terrain correction
K_T	Terrain correction integral kernel
r	Radial distance from point outside the sphere to the center of the sphere
$d\sigma$	surface element on the sphere
l	Spatial distance
δg_u	Upward continued gravity disturbances
δg_D	Gravity disturbances at level zero
K_P	Poisson integral kernel

f	Frequency
$q(x)$	Function in space domain
$Q(f)$	Function in the frequency domain
$Q(f_x, f_y)$	Two-dimensional Fourier transform
f_x, f_y	Frequencies corresponding to the x and y spatial coordinates
$M_x M_y$	Discrete values on a grid in x and y directions
T_x, T_y	Periods in x and y directions
F_2	Two-dimensional Fourier operator
$w(x)$	Window function
x_0	Delay parameter
Q_W	Wavelet transform
m	Scale parameter
x_n	Shifting parameter
C_ψ	Admissibility constant
ψ	Wavelet analyzing function
$\bar{\psi}$	Complex conjugate
d_n^m	Detailing coefficients
λ_0	Scale space parameter
n	Translation integer
V_m	Approximation subspace
$\varphi_{m,n}$	Scaling function
W_m	Detailing spaces
c_n^m	Approximation coefficients
h_n	Scaling coefficients
g_n	Detailed coefficients

$I_{\{ d_n^m >\delta\}}$	Indicator function
δ	Hard threshold value
δ'	Soft threshold value
A_{ij}	Design matrix of the wavelet coefficients of the kernels
b_i	Vector of the unknown signal
a_j	Column vector of the wavelet coefficients of the data
d^H	Two-dimensional wavelet transform horizontal set of coefficients
d^V	Two-dimensional wavelet transform vertical set of coefficients
d^D	Two-dimensional wavelet transform diagonal set of coefficients

Chapter One: Introduction

In recent years, the amount of data available for the solution of the boundary value problem has increased significantly. This availability demands the introduction of efficient numerical solutions for different types of geodetic problems. For a long time, the fast Fourier transform (FFT) has efficiently provided these numerical solutions and has become the main signal processing tool in the geodetic arsenal. In this research, an alternative approach is introduced for the solution of different boundary value problems and the evaluation of different geodetic operators; this technique is the wavelet transform.

1.1 Background and motivation

The first wavelet was derived from the Haar base function found around 1910 by Haar [Keller, 2004]. Morlet and Grossman created a large revolution in the wavelet world in the beginning of the 1980's when they introduced what is called the continuous wavelet transform. Their development was followed by the successful construction of an orthogonal wavelet with compact support by Daubechies [Daubechies, 1990]. This was combined by Mallat into a multi-resolution representation to introduce a solid system to be used in signal analysis [Mallat, 1989]. Since then, the wavelet has been used in a wide range and variety of scientific applications.

The wavelet transform evaluation of geodetic operators in planar approximation was studied by Salamonowicz [2000], Gilbert and Keller [2000], and Liu and Sideris [2003]. Salamonowicz [2000] used the wavelet transform for global representation of the gravity field. The Earth gravitation model (EGM) was represented on a wavelet basis. The motivation was to provide EGM coefficients that can be updated easily when new regional data is available. A geoid undulation map was produced, and a local update of these maps was introduced where new gravity anomalies became available. Gilbert and Keller [2000] introduced a combined wavelet-vaguelette technique for the evaluation of

convolution problems. The main disadvantage of this algorithm is that it depends on the length of the wavelet filters used, which is not global as in the case of FFT.

Liu and Sideris [2003] introduced a three-dimensional wavelet transform for the evaluation of Stokes and Vening Meinesz integrals. This approach allowed the evaluation of the integrals on a meridian-by-meridian basis. The paper concludes that, with Stokes integral, a geoid with millimetre, centimeter, and decimetre accuracy can be computed using compression levels of 70%, 74%, and 78%, respectively. In the case of the Vening Meinesz integral, deflections of the vertical with sub-arc-second, 1 arc-second, and 2 arc-second accuracy can be obtained using compression levels of 91%, 97% and 99%, respectively. The time required for the computations mentioned above, for a 64×64 grid, was around 2.5 seconds with a 99% kernel compression level.

The spherical wavelet theory and algorithms were initially developed by the Geomathematics Group at the University of Kaiserslautern [Freedon, 1999]. Harmonic wavelets representation algorithms were developed for recovering the external gravity potential of the Earth from discrete (spaceborne) data. Different solutions were introduced for different satellite missions' types such as satellite-to-satellite tracking and satellite gravity gradiometry.

Schaffrin et al. [2003] studied the advantages of 2-D planar wavelets for the representation of scalar-value signals on the sphere. The study focused on the division of the sphere surfaces into regional patches. A Mercator map projection system at the equator was combined with pseudo-wavelets in order to capture regional phenomena. The proposed algorithm can be used with any type of planar wavelets for geodetic applications on the sphere. Schmidt et al. [2006] applied a spherical wavelet technique for the regional spatiotemporal gravity field determination over the Amazon region, using GRACE measurements. In this study, the Amazon hydrological signals were represented in a form of time series of level dependent detailed signals. The spherical wavelet solution was compared to different hydrology models and a promising agreement was achieved.

Soltanpour et al. [2006] used the second generation of the wavelet transform to combine the gravimetric model with GPS leveling for non-gridded data. The main target was to provide a better transformation of GPS ellipsoidal heights to normal heights. A lifting scheme, which does not require regularly spaced data, was used. The paper showed that the second generation wavelet method is better than the least squares collocation (LSC) because there is no need for removing the trend from the data and the assumption of stationarity of LSC is not required. The differences between the second generation wavelet solutions and the LSC solution in standard deviation were a few millimeters, but the wavelet was better in decreasing the maximum and minimum differences than the LSC in comparison with reference data.

From the previous discussion, it can be recognized that the research done on the evaluation of geodetic operators using wavelet transform requires further and more detailed investigation. The properties of the wavelet transform, such as having compact support, space and frequency localization, a wide variety of base functions (some of them with orthogonality properties), de-noising and thresholding, and multi-resolution analysis, are the main motivations for testing the wavelet transform as an alternative to the FFT in the planar approximation. These properties were always mentioned in the previous studies but was not fully implemented or tested. More specifically, the motivations behind the use of the wavelet transform in the representation of different geodetic operators are the following:

Orthogonality, localization, and compact support properties: Most geodetic kernels, such as Stokes, Vening Meinesz, etc., are singular and are decaying fast away from their origin. Due to the localization properties of the wavelet transform in the space and frequency domains, the location of the peaks can be efficiently determined in both domains. Moreover, many of the wavelet coefficients of the kernels are negligibly small. This will lead to sparse matrices in the evaluation of different geodetic operators, especially when using wavelet base functions with a number of vanishing moments.

Thresholding and compression of matrices: Because the location of the small wavelet coefficients is known in the frequency domain, these wavelet coefficients of the kernels of the geodetic operators can be significantly compressed using wavelet thresholding techniques. The thresholding value is estimated through an efficient system of equations that motivates testing the level of compression that can be reached with an acceptable accuracy of results.

Wavelet multiresolution analysis and de-noising of signals with non-stationary noise: The wavelet multiresolution analysis into independent levels of decomposition can help probe inside the data and separate the noise from the signals. Consequently, this leads to a detailed analysis and interpretation of the signal. The main disadvantage of the FFT technique is its assumption that the signal to be processed has invariant statistical properties (stationarity). Conversely, most of the data and applications deviate from this assumption and have a non-stationary behavior. Wavelet analysis can be used in detecting this behavior and the removal of non-stationary noise.

All these motivations support the use of wavelets as an alternative to FFT in many applications in different fields that require the analysis of non-stationary processes containing multi-scale features, singularities, transient phenomena, and signal compression.

1.2 Thesis objectives

The overall objective of the thesis is to introduce an efficient representation of the different geodetic operators on wavelet bases. More specifically, direct and inverse geodetic integrals will be evaluated, in addition to the numerical inversion of direct geodetic integrals. The following sub-objectives are addressed:

- Implementation of a new wavelet algorithm, requiring less computational effort than standard implementations, for the solution of

- direct and inverse geodetic integrals and testing its accuracy and efficiency in comparison to FFT and numerical integration.
- Investigation of the effects of the kernel properties on the wavelet compression technique used in the evaluation of different geodetic operators. Also, testing the adaptability of the suggested thresholding algorithm to a number of kernels with different properties.
 - Development of a new thresholding technique to optimize the wavelet compression level to an acceptable accuracy in the wavelet evaluation of geodetic operators.
 - Assessment of the performance of the wavelet soft thresholding technique as a regularization tool for de-noising stationary and non-stationary noise and its impact on the inversion of the geodetic integrals.

1.3 Thesis outline

In Chapter Two, a general overview of the important geodetic integrals used in the thesis is given in planar approximation, with an explicit definition of the kernel relevant to each integral.

Chapter Three starts with a brief overview of the FFT technique. The fundamentals of the wavelet transform and the multi-resolution analysis are then introduced. The properties of the wavelet multi-resolution analysis are listed. Soft and hard thresholding techniques are also discussed. An automated algorithm for the estimation of the thresholding value for both de-noising and compression applications is given. Standard and non-standard wavelet representations of operators are discussed. The wavelet algorithm developed for the representation of different geodetic operators is illustrated in detail.

Chapter Four gives the procedure for the selection of base wavelets. Practical examples of the analysis and localization properties of the wavelet transform are given in one-dimensional (airborne gravimetry data) and two-dimensional (Stokes's kernel and non-stationary noise) applications. Examples of hard thresholding compression of

different kernels are introduced. Two different techniques for applying the thresholding values are described. Examples of soft thresholding in one and two dimensions are also given.

Chapter Five contains the results of the wavelet evaluation of four direct geodetic integrals: the Stokes, the Vening Meinesz, the Poisson (upward continuation), and the terrain correction integrals. For each integral, the wavelet solutions are compared to the FFT and the numerical integration solutions. Hard thresholding is applied for the compression of the wavelet coefficients of the kernels of the four geodetic integrals. Two different compression procedures are tested.

Chapter Six provides an evaluation of the inverse geodetic problems. Two different kinds of problems are studied. The first one is inverse geodetic integrals, namely the inverse Vening Meinesz integral and the deflection-geoid formula. Hard thresholding is again applied for the compression of the kernels' wavelet coefficients. The second is the numerical inversion of direct integrals, namely the inversion of the Stokes and the Poisson integral (downward continuation). The solution is done with noise-free data, and then the solution is repeated afterwards with the addition first of stationary and then non-stationary noise. The solution is repeated after de-noising, and results are compared.

Finally, Chapter Seven summarizes the work done in this research and draws conclusions. It also gives recommendations for further developments.

Chapter Two: Overview of important geodetic integrals

Gravity measurements are commonly used for solving problems in physical geodesy. Data describing the gravity field of the Earth, such as geoid undulations, deflection of the vertical, gravity anomalies, and gravity disturbances, are the information sources used in different geophysical studies. Gravity measurements are taken at discrete points on the surface of the Earth. The modeling, continuation, and transformation of these data from one form to another is the main focus in this chapter. The main geodetic integrals used for this purpose are briefly introduced.

The chapter is divided into three main parts. The first part is about regional geoid and deflection modeling through the Stokes, Vening Meinesz, and terrain correction integrals. The second gives the Poisson integral for upward and downward continuation in airborne or spaceborne gravimetry. The third discusses the inverse problems that are most used in satellite altimetry applications; the inverse Vening Meinesz integral, the deflection-geoid formula, and the inversion of the Stokes integral are introduced. All representations are given in planar approximation. A literature review about the different techniques used for solving all these models is included.

2.1 Regional geoid and deflection modeling

In this section, the equations for the solution of the classical boundary value problem are presented. The Stokes, Vening Meinesz, and terrain correction integrals are given in planar approximation.

2.1.1 The Stokes integral

The disturbing potential T at a point P on the surface of a sphere can be represented in spherical approximation, using free-air gravity anomalies Δg , as follows:

$$T(P) = \frac{R}{4\pi} \int_{\alpha=0}^{2\pi} \int_{\psi=0}^{\pi} \Delta g(\psi, \alpha) S(\psi) \sin \psi \, d\psi \, d\alpha \quad (2.1)$$

where

$$S(\psi) = \frac{I}{\sin(\psi/2)} - 6 \sin(\psi/2) + 1 - 5 \cos(\psi) \ln \left[\sin \frac{\psi}{2} + \sin^2 \left(\frac{\psi}{2} \right) \right] \quad (2.2)$$

ψ and α are spherical distance and azimuth. From Bruns' theorem [Moritz, 1980], the geoidal undulation N can be computed from T by the following formula:

$$N(P) = \frac{T(P)}{\gamma} \quad (2.3)$$

In limited areas, as is the case in this thesis, the spherical surface can be approximated by the plane tangent at point P ; therefore, ψ is small and the Stokes function is approximated as follows:

$$S(\psi) \approx \frac{I}{\sin(\psi/2)} \approx \frac{I}{\psi/2} \approx \frac{2}{\psi} \approx \frac{2R}{s} \quad (2.4)$$

where s is the planar distance (and forms a coordinate system with α), and R is the mean radius of the Earth.

In the new coordinate system, the differential area $d\sigma = \sin \psi d\psi d\alpha$ becomes

$$d\sigma = \frac{I}{R^2} s ds d\alpha \quad (2.5)$$

Therefore, Stokes' formula takes the following form in planar approximation:

$$N(P) = \frac{T(P)}{\gamma} = \frac{I}{2\pi\gamma} \int_{s=0}^{s_{max}} \int_{\alpha=0}^{2\pi} \frac{\Delta g(s, \alpha)}{s} s ds d\alpha \quad (2.6)$$

By transforming the polar coordinates to rectangular coordinates to describe a limited area E , Equation (2.6) takes the following form:

$$N(x_p, y_p) = \frac{1}{2\pi\gamma} \iint_E \Delta g(x, y) [(x_p - x)^2 + (y_p - y)^2]^{-1/2} dx dy \quad (2.7)$$

The error from planar approximation is negligible for small areas [Sideris, 1987]. For gridded data of equal spacing (Δx and Δy), which is the case in this research study, the elements of the kernel are as follows [Schwarz et al., 1990]:

$$K_N = \begin{cases} \frac{\Delta x \Delta y}{2\pi\gamma} [(x_p - x)^2 + (y_p - y)^2]^{-1/2} & , x_p \neq x \text{ or } y_p \neq y \\ \frac{1}{\gamma} \sqrt{\frac{\Delta x \Delta y}{\pi}} & , x_p = x \text{ and } y_p = y \end{cases} \quad (2.8)$$

The second value compensates for the singularity of K_N at the computational point. The relative error of the approximation of the singularity ranges between 1% to 2% for an inner zone of radius between 10 km and 20 km [Heiskanen and Moritz, 1967]. It is actually much smaller when residual Δg are used.

The Stokes integral has been evaluated successfully by fast Fourier transform (FFT) techniques; a detailed representation of the integral in the Fourier domain can be found in Schwarz et al. [1990], Strang van Hees [1990], and Sideris [2005]. Evaluation is possible in the planar and spherical approximation. Fast evaluation of the Stokes integral by the one-dimensional FFT was developed by Haagmans et al. [1993]. Sideris and Li [1993] showed how to solve the integral as a convolution using FFT without windowing and edge effects. Salamonowicz [2000] introduced a wavelet representation of the global gravity field through the evaluation of the Stokes integral. Liu and Sideris [2003] evaluated the Stokes integral by a three-dimensional wavelet transform algorithm.

2.1.2 The Vening Meinesz integral

The Vening Meinesz integral is used to determine the two components of the deflection of the vertical. The integral is derived by the differentiation of Equation (2.7) in the x and y directions, as follows:

$$\xi(x_p, y_p) = -\frac{\partial N(x_p, y_p)}{\partial y_p} \quad (2.9)$$

$$\eta(x_p, y_p) = -\frac{\partial N(x_p, y_p)}{\partial x_p} \quad (2.10)$$

By using Equation (2.7) in Equations (2.9) and (2.10),

$$\xi(x_p, y_p) = \frac{1}{2\pi\gamma} \iint_E \Delta g(x, y) [(x_p - x)^2 + (y_p - y)^2]^{-3/2} (y_p - y) dx dy \quad (2.11)$$

$$\eta(x_p, y_p) = \frac{1}{2\pi\gamma} \iint_E \Delta g(x, y) [(x_p - x)^2 + (y_p - y)^2]^{-3/2} (x_p - x) dx dy \quad (2.12)$$

For gridded data with equal spacing (Δx and Δy), which is the case in this research study, the elements of the kernels are as follows [Heiskanen and Moritz, 1967]:

$$K_\xi = \begin{cases} \frac{\Delta x \Delta y}{2\pi\gamma} [(x_p - x)^2 + (y_p - y)^2]^{-3/2} (y_p - y) & , x_p \neq x \text{ or } y_p \neq y \\ -\frac{1}{2\gamma} \sqrt{\frac{\Delta x \Delta y}{\pi}} \frac{g_x(x, y)}{\Delta g(x, y)} & , x_p = x \text{ and } y_p = y \end{cases} \quad (2.13)$$

$$K_\eta = \begin{cases} \frac{\Delta x \Delta y}{2\pi\gamma} [(x_p - x)^2 + (y_p - y)^2]^{-3/2} (x_p - x) & , x_p \neq x \text{ or } y_p \neq y \\ -\frac{1}{2\gamma} \sqrt{\frac{\Delta x \Delta y}{\pi}} \frac{g_y(x, y)}{\Delta g(x, y)} & , x_p = x \text{ and } y_p = y \end{cases} \quad (2.14)$$

where $g_x(x, y)$ and $g_y(x, y)$ are the first derivatives of the gravity anomaly $\Delta g(x, y)$ at the computation point in the x and y direction, respectively. The second value, in both Equations (2.13) and (2.14), compensates for the singularity at the computational point [Li, 1993].

The Vening Meinesz integral has been evaluated by two-dimensional FFT in both planar [Schwarz et al., 1990; Sideris, 2005] and spherical approximation [Liu et al., 1997]. Liu and Sideris [2003] evaluated the Vening Meinesz integral by a three-dimensional wavelet transform algorithm.

2.1.3 Terrain corrections integral

In rough terrain, topography represents the short-wavelength part of the gravity field variation. The terrain effects can be modeled by assuming a known topographic density ρ (for example, the mean density of the topographic masses is assumed equal to 2.67 g cm^{-3}), leading to a smoother residual field for gravity modeling. After the

estimation of terrain-reduced gravity field quantities, the terrain effects must be added back to obtain the final quantity. This remove-restore technique is essential when working with gravity field modeling in rough topography because the resolution of the gravity data used cannot usually represent the short wavelengths of the gravity field.

Two main cases can be distinguished for the computation of the terrain effects. The first one is the computation of the terrain effects at a level surface above the terrain at height $z_0 > h_{\max}$, where h_{\max} is the highest topographic elevation in the area E . The topographic effect on gravity at P_0 , Δg_h is computed as follows [Forsberg, 1985]:

$$\Delta g_h(x_p, y_p, z_0) = -G\rho \iiint_{E h} [(x_p - x)^2 + (y_p - y)^2 + (z_0 - z)^2]^{-3/2} (z - z_0) dx dy dz \quad (2.15)$$

The integral in Equation (2.15) is expanded using the so-called multipole expansion about $z=0$ as follows [Schwarz et al., 1990]:

$$\frac{z - z_0}{[(x_p - x)^2 + (y_p - y)^2 + (z_0 - z)^2]^{3/2}} = -\frac{z_0}{r_0^3} + \frac{r_0^2 - 3z_0^2}{r_0^5} z + \dots, \quad (2.16)$$

where

$$r_0 = [(x_p - x)^2 + (y_p - y)^2 + z_0^2]^{1/2} \quad (2.17)$$

Integrating Equation (2.15) with respect to z , Δg_h is represented as a sum of convolutions as follows:

$$\Delta g_h = G\rho \left[\left(\frac{z_0}{r^3} * h \right) + \left(-\frac{(r^2 - 3z_0^2)}{2r^5} * h^2 \right) + \dots \right] \quad (2.18)$$

The second case is the computation of the terrain effects at the physical surface of the Earth. The total gravity topographic effect at a certain point P can be split into a Bouguer plate effect and the terrain correction c , as follows:

$$\Delta g_h = 2\pi G\rho h - c, \quad (2.19)$$

$$c(x_p, y_p) = G\rho \iiint_{E h} [(x_p - x)^2 + (y_p - y)^2 + (h_p - z)^2]^{-3/2} (z - h_p) dx dy dz \quad (2.20)$$

By expanding Equation (2.20) using Equation (2.16) about $z = h_p$, ignoring the second term and higher, and performing the z integration, the following equation is obtained [Sideris, 1984]:

$$c(x_p, y_p) \approx \frac{G\rho}{2} \iint_E (h - h_p)^2 [(x_p - x)^2 + (y_p - y)^2]^{-3/2} dx dy \quad (2.21)$$

Equation (2.21) is the linear approximation of the terrain correction integral.

Equation (2.21) is divided into three parts and each part is a discrete convolution:

$$c(x_p, y_p) = \frac{G\rho}{2} [c_1 + c_2 + c_3] \quad (2.22)$$

where

$$c_1(x_p, y_p) = \iint h^2(x, y) [(x_p - x)^2 + (y_p - y)^2]^{-3/2} dx dy \quad (2.23)$$

$$c_2(x_p, y_p) = -2h(x_p, y_p) \iint h(x, y) [(x_p - x)^2 + (y_p - y)^2]^{-3/2} dx dy \quad (2.24)$$

$$c_3(x_p, y_p) = h^2(x_p, y_p) \iint [(x_p - x)^2 + (y_p - y)^2]^{-3/2} dx dy \quad (2.25)$$

Equations (2.23), (2.24), and (2.25) are evaluated as direct convolution problems. The convolution in Equation (2.25) is done between a unit grid (has a value of 1 for the all the grid points) and the kernel. The kernel used in the evaluation of the three equations is defined as follows:

$$K_T = \begin{cases} (\Delta x \Delta y) [(x_p - x)^2 + (y_p - y)^2]^{-3/2} & , x_p \neq x \text{ or } y_p \neq y \\ 0 & , x_p = x \text{ and } y_p = y \end{cases} \quad (2.26)$$

The zero value compensates for the singularity at the computational point [Sideris, 1984]. The output from the three equations are added together to get the terrain corrections at the computational point.

The terrain correction integral has been solved and evaluated by two-dimensional FFT by Sideris [1984] and [1990].

2.2 The Poisson integral for airborne gravimetry

The Poisson integral is used for the upward continuation problem and is inverted for the downward continuation problem. It is based on the first boundary value problem of physical geodesy, Dirichlet's problem. The Poisson integral is applied in this thesis to the harmonic continuation of the gravity disturbance as follows [Heiskanen and Mortiz, 1967]:

$$\delta g_u(\varphi_p, \lambda_p) = \frac{R(r_p^2 - R^2)}{4\pi r_p} \iint \frac{1}{l^3} R \delta g_D(\varphi, \lambda) d\sigma \quad (2.27)$$

where R is the radius of the sphere, r is the radial distance from point outside the sphere to the center of the sphere, $d\sigma$ the surface element on the sphere and l is the spatial distance between a point on the sphere and a point outside the sphere. Equation (2.27) is presented in the planar approximation as follows [Bláha et al., 1996]:

$$r^2 - R^2 = (r - R)(r + R) = z_0(r + R) \approx 2z_0R, \quad (2.28)$$

$$l = [(x_p - x)^2 + (y_p - y)^2 + z_0^2]^{1/2}, \text{ and} \quad (2.29)$$

$$d\sigma = \frac{1}{R^2} dx dy \quad (2.30)$$

$$\delta g_u(x_p, y_p, z_0) = \frac{1}{2\pi} \iint_E z_0 [(x_p - x)^2 + (y_p - y)^2 + z_0^2]^{-3/2} \delta g_D(x, y, 0) dx dy \quad (2.31)$$

where δg_u is the upward continued gravity disturbances at $h = z_0$, δg_D is the gravity disturbances at level zero, and z_0 is the flight elevation.

The downward continuation is evaluated through the inversion of Equation (2.31), where δg_D will be the unknown and δg_u will be given. The inversion of the Poisson integral will be through an optimization procedure (gradient method). The Poisson kernel will be the input of the design matrix to be used in the optimization procedure. For gridded data with equal spacing (Δx and Δy), which is the case in this research study, the kernel of the upward and downward continuation is as follows:

$$K_P = \frac{z_0}{2\pi} (\Delta x \Delta y) [(x_p - x)^2 + (y_p - y)^2 + z_0^2]^{-3/2} \quad (2.32)$$

The Poisson integral for downward and upward continuation is evaluated by two-dimensional FFT by Bláha et al. [1996] and Wu [1996]. Forsberg [2002] tested different operational methods based on collocation and FFT and applied these to downward continuation of surface data merging of airborne surveys over Greenland and Svalbard. Keller [1995] introduced a theoretical harmonic downward continuation technique using a Haar Wavelet.

2.3 Satellite altimetry integrals

Two main formulae are used in the determination of geoid undulations and gravity anomalies from satellite altimetry: the inverse Vening Meinesz integral and the deflection-geoid formula. These two integrals are presented in planar approximation [Hwang, 1998; Hwang et al., 2002].

2.3.1 Inverse Vening Meinesz' integral

The key in deriving the inverse Vening Meinesz formula is to find a suitable kernel for converting deflection of the vertical components to gravity anomalies. The derivation is mainly based on the approach of Meissl [1971]. The formula is approximated on the plane as follows [Hwang, 1998]:

$$\begin{aligned} \Delta g(x_p, y_p) &= \frac{\gamma}{4\pi} \iint_E \frac{-2}{s^3} [\xi(x, y)(s \cos \alpha) + \eta(x, y)(s \sin \alpha)] dx dy \\ &= \frac{-\gamma}{2\pi} \left\{ \begin{aligned} &\iint_E (y_p - y) [(x_p - x)^2 + (y_p - y)^2]^{-3/2} \xi(x, y) dx dy + \\ &\iint_E (x_p - x) [(x_p - x)^2 + (y_p - y)^2]^{-3/2} \eta(x, y) dx dy \end{aligned} \right\} \quad (2.33) \end{aligned}$$

For gridded data with equal spacing (Δx and Δy), which is the case in this research study, the elements of the kernels are as follows:

$$K_{\xi} = \begin{cases} \frac{-\gamma}{2\pi} (\Delta x \Delta y) [(x_p - x)^2 + (y_p - y)^2]^{-3/2} (y_p - y) & , x_p \neq x \text{ or } y_p \neq y \\ \frac{\gamma}{2\sqrt{\pi}} \frac{\sqrt{\Delta x \Delta y}}{\xi(x, y)} \xi_y(x, y) & , x_p = x \text{ and } y_p = y \end{cases} \quad (2.34)$$

$$K_{\eta} = \begin{cases} \frac{-\gamma}{2\pi} (\Delta x \Delta y) [(x_p - x)^2 + (y_p - y)^2]^{-3/2} (x_p - x) & , x_p \neq x \text{ or } y_p \neq y \\ \frac{\gamma}{2\sqrt{\pi}} \frac{\sqrt{\Delta x \Delta y}}{\eta(x, y)} \eta_x(x, y) & , x_p = x \text{ and } y_p = y \end{cases} \quad (2.35)$$

The second value in Equations (2.34) and (2.35) are to compensate for the singularity at the computational point, where $\xi_y(x, y)$ and $\eta_x(x, y)$ are the first derivatives of the two components of the deflection of the vertical.

Hwang [1998] used the inverse Vening Meinesz formula, which converts the deflections of the vertical to gravity anomalies, and evaluated it by the two-dimensional FFT method. Sandwell and Smith [1997] computed gravity anomalies from a dense network of satellite altimetry profiles of geoid heights and a grid of the two components of the deflection of the vertical also by using two-dimensional FFT. The previously mentioned approaches rely on stationary noise assumptions.

2.3.2 Deflection-geoid formula

The planar approximation of the deflection-geoid formula based on the approach of Meissl [1971] is the following [Hwang, 1998]:

$$N(x_p, y_p) = \frac{1}{4\pi} \iint_E \frac{-2}{s^2} [\xi(x, y)(s \cos \alpha) + \eta(x, y)(s \sin \alpha)] dx dy$$

$$= \frac{-1}{2\pi} \left\{ \begin{aligned} & \iint_E (y_p - y) [(x_p - x)^2 + (y_p - y)^2]^{-1} \xi(x, y) dx dy + \\ & \iint_E (x_p - x) [(x_p - x)^2 + (y_p - y)^2]^{-1} \eta(x, y) dx dy \end{aligned} \right\} \quad (2.36)$$

For gridded data with equal spacing (Δx and Δy), which is the case in this research study, the elements of the kernels are as follows:

$$K_{\xi} = \begin{cases} \frac{-1}{2\pi} (\Delta x \Delta y) [(x_p - x)^2 + (y_p - y)^2]^{-1} (y_p - y) & , x_p \neq x \text{ or } y_p \neq y \\ \frac{\Delta x \Delta y}{4\pi} \frac{\xi_y(x, y)}{\xi(x, y)} & , x_p = x \text{ and } y_p = y \end{cases} \quad (2.37)$$

$$K_{\eta} = \begin{cases} \frac{-1}{2\pi} (\Delta x \Delta y) [(x_p - x)^2 + (y_p - y)^2]^{-1} (x_p - x) & , x_p \neq x \text{ or } y_p \neq y \\ \frac{\Delta x \Delta y}{4\pi} \frac{\eta_x(x, y)}{\eta(x, y)} & , x_p = x \text{ and } y_p = y \end{cases} \quad (2.38)$$

The second value in Equations (2.37) and (2.38) is to compensate for the singularity at the computational point.

Hwang [1998] and Hwang et al. [2002] evaluated the deflection geoid formula by two-dimensional FFT for satellite altimetry applications.

2.3.3 Inverting the Stokes integral

Equation (2.7) for the Stokes integral in planar approximation is inverted by an optimization procedure. In this case, the gravity anomalies are unknown and the geoid undulations are given. The Stokes kernel, Equation (2.8), forms the design matrices used in the optimization procedure for determining the gravity anomalies. More details of the algorithm and the implementation will be given in Chapter Three.

Rauhut [1992] tested different regularization methods for the solution of the inverse Stokes' problem using simulated and observed data.

2.4 Summary

In this chapter, seven different operators were presented. The operators are Stokes', Vening Meinesz', terrain corrections, Poisson', inverse Vening Meinesz', deflection-geoid formula, and the inversion of the Stokes integral. For many years, the classical approach used for the efficient evaluation of geodetic operators has been based on the fast Fourier transform (FFT). This approach is well established and is now a standard tool in the geodetic arsenal. With the same gridded data as inputs, the FFT

evaluation accuracy is identical to that of numerical integration. The main advantage of the FFT approach is its speed. Concerning the wavelet domain, few evaluations have been introduced. Only the Stokes and the Vening Meinesz operators have been evaluated by three-dimensional wavelet transform [Liu and Sideris, 2003]. Salamonowicz [2000] introduced a wavelet-based gravity model through the evaluation of the Stokes' integral.

Chapter Three: Fundamentals of wavelet transform and multi-resolution analysis

For many years, digital signal processing has been governed by the theory of Fourier transform and its numerical implementation. The main disadvantage of Fourier theory is the underlying assumption that the signals have time-wise or space-wise invariant statistical properties. In many applications, the deviation from a stationary behavior is precisely the information to be extracted from the signals. Wavelets were developed to serve the purpose of analyzing such non-stationary signals; see Keller [2004].

Signal processing was and still is a very important tool for data analysis in geodetic applications, especially Physical Geodesy. The Fourier transform has been used as a reliable tool in signal analysis for many years. Invented in the early 1800s by Jean Fourier, the fast Fourier transform (FFT) has become a cornerstone of modern signal analysis. The FFT has proven incredibly versatile in a wide range of geodetic applications. Nevertheless, it suffers from certain limitations related to the assumption that the environment is stationary, which is not always the case. Recently, another type of transform, the wavelet transform, has been shown to be as powerful and versatile as the FFT, yet without some of its limitations.

Wavelets, as a mathematical tool, have been extensively used in research in the last two decades. From the mid 1980s until now, wavelet techniques have been used in many applications that involve signal processing, such as image processing, medical diagnostics, geophysical signal processing, pattern recognition, electromagnetic wave scattering, boundary value problems, and so on [Goswami and Chan, 1999].

The wavelet transform is the result of the work of a number of researchers. Initially, a French geophysicist, Jean Morlet, in 1985, came up with a method to model the process of sound waves traveling through the Earth's crust. Unlike Fourier analysis, he did not use sine or cosine base functions, but different ones, that he called *wavelets*. Yves Meyer, a mathematician, recognized this work to be part of the field of harmonic analysis and came up with a family of wavelets that he proved were most efficient for

modeling complex phenomena [Meyer, 1992]. This work was improved by two American researchers, Stephane Mallat of New York University [Mallat, 1998] and Ingrid Daubechies of Bell Labs [Daubechies, 1992]. Since 1998, there has been extensive activity in this area, as engineers and researchers have applied the wavelet transform to applications like signal analysis, detection of signal jumps, de-noising, image compression, and fingerprint analysis.

The starting point for the discussion of the wavelet transform and its properties is an overview to the Fourier analysis methods. In particular, the overview illustrates the advantages of using the former over the latter in the analysis of transient signals and also highlights its drawbacks. This chapter gives an overview of the Fourier transform and its properties. In addition, continuous and discrete wavelet transform in one and two dimensions are illustrated, and two wavelet thresholding techniques are discussed. The non-standard wavelet implementation for solving geodetic problems is described. Finally, the methodology of investigation used in the evaluation of geodetic integrals is introduced.

3.1 Overview of the Fourier transform and its convolution property

Traditionally, Fourier transform has been used extensively in the signal processing field for the analysis of stationary signals. It can be used to decompose a function in terms of a set of base functions. A set of complex sinusoids forms the set of base functions used in the Fourier transform.

The one-dimensional continuous Fourier transform is defined by [Brigham, 1988]:

$$Q(f) = \int_{-\infty}^{\infty} q(x) e^{-i2\pi fx} dx \quad (3.1)$$

f is the frequency, $q(x)$ is the function in the space domain and $Q(f)$ is its transformation in the frequency domain.

The inverse continuous Fourier transform determines a function from its Fourier transform as follows:

$$q(x) = \int_{-\infty}^{\infty} Q(f) e^{i2\pi fx} df \quad (3.2)$$

Since all the geodetic problems introduced in Chapter Two are two-dimensional problems, the definition of the two-dimensional continuous Fourier transform is essential and modeled as follows:

$$Q(f_x, f_y) = \int_{-\infty}^{\infty} \int_{-\infty}^{\infty} q(x, y) e^{-i2\pi(f_x x + f_y y)} dx dy \quad (3.3)$$

and the two-dimensional inverse continuous Fourier transform is

$$q(x, y) = \int_{-\infty}^{\infty} \int_{-\infty}^{\infty} Q(f_x, f_y) e^{i2\pi(f_x x + f_y y)} df_x df_y \quad (3.4)$$

where $Q(f_x, f_y)$ is the spectrum of the function $q(x, y)$, and f_x, f_y are the frequencies corresponding to the x and y spatial coordinates, respectively.

The discrete Fourier transform produces a sequence of complex values at discrete frequencies; because the transform is the result of a sum over the whole signal length, the resultant coefficients cannot indicate at what location in the signal the frequency existed. The Fourier transform provides perfect frequency resolution, but no space resolution [Keller, 2004]. In two-dimensional discrete Fourier transform, the function is given by $M_x M_y$ discrete values on a grid in x and y directions, where

$$\begin{aligned} x &= k\Delta x, k = 0, 1, 2, \dots, M_x - 1 \\ y &= l\Delta y, l = 0, 1, 2, \dots, M_y - 1 \end{aligned} \quad (3.5)$$

and for periods T_x and T_y the intervals are

$$\begin{aligned}\Delta x &= \frac{T_x}{M_x} \\ \Delta y &= \frac{T_y}{M_y}\end{aligned}\tag{3.6}$$

In the frequency domain, the frequencies f_x and f_y are expressed as follows:

$$\begin{aligned}f_x &= j\Delta f_x, \quad j = 0, 1, 2, \dots, M_x - 1 \\ f_y &= m\Delta f_y, \quad m = 0, 1, 2, \dots, M_y - 1\end{aligned}\tag{3.7}$$

The frequency intervals $(\Delta f_x, \Delta f_y)$ are related to the space periods (T_x, T_y) by

$$\begin{aligned}\Delta f_x &= \frac{1}{T_x} \\ \Delta f_y &= \frac{1}{T_y}\end{aligned}\tag{3.8}$$

Thus, Equations (3.3) and (3.4) can be discretized as follows:

$$Q(j, m) = \frac{T_x}{M_x} \frac{T_y}{M_y} \sum_{k=0}^{M_x-1} \sum_{l=0}^{M_y-1} q(k, l) e^{-i2\pi\left(\frac{jk}{M_x} + \frac{ml}{M_y}\right)} = F_2\{q(k, l)\}\tag{3.9}$$

$$q(k, l) = \frac{1}{T_x} \frac{1}{T_y} \sum_{j=0}^{M_x-1} \sum_{m=0}^{M_y-1} Q(j, m) e^{i2\pi\left(\frac{jk}{M_x} + \frac{ml}{M_y}\right)} = F_2^{-1}\{Q(j, m)\}\tag{3.10}$$

where F_2 is the two-dimensional Fourier operator. The detailed properties of the two-dimensional Fourier transform [Bracewell, 1986; Nawab and Quatieri, 1988; Brigham, 1988] and its implementation for the evaluation of different geodetic problems can be found in Sideris [1984], Sideris and Schwarz [1986], Sideris and Tziavos [1988], Schwarz et al. [1990], and Sideris and Li [1993].

More sophisticated Fourier-based transforms have been developed to reduce the effect of non-stationary signals on the discrete Fourier transform. One of these methods is the windowed discrete Fourier transform (WDFT). The difficulty of analyzing a non-stationary signal lies in determining at what location in space a given transient occurred

[Osman, 2003; Keller, 2004]. Because the frequencies in a non-stationary signal do not exist for every location throughout the signal, this space localization is important. If it is possible to divide the non-stationary signal into a number of smaller, stationary signals, then the Fourier transform of each sub-division is accomplished by applying a window function, $w(x)$, to the input signal before computing the Fourier transform [Harris, 1978]. If the window function $w(x)$ is translated in space by x_0 , which is called the *delay parameter*, the WDFT is defined to be

$$Q_{WDFT}(f) = \int_{-\infty}^{\infty} [q(x) w(x - x_0)] e^{-i2\pi fx} dx \quad (3.11)$$

Essentially, the Fourier transform is equivalent to the WDFT with a box window function of finite support. Figure 3.1 shows a WDFT, where the window is simply a square wave. The square wave window truncates the sine or cosine function to fit a window of a particular width. Because a single window is used for all frequencies in the WDFT, the resolution of the analysis is the same at all locations in the space frequency plane.

In Figure 3.1, the WDFT of a signal is represented in a two-dimensional grid where the divisions in the horizontal direction represent the extent for each window $w(x - x_0)$, the divisions in the vertical direction represent the frequencies f , and the shade of each rectangle is proportional to the corresponding frequency. As the width or support of the window function decreases, a smaller portion of the input signal is considered, guaranteeing greater space localization of frequency components in the signal. As the support of the window function increases, more accurate information about frequencies within the window is obtained, but the ability to determine at what location those transients occur within the input signal is lost [Chui, 1992]. Accordingly, it can be said that the major problem of WDFT is that the window width is fixed. This problem shows that a fine space resolution for short duration and high frequency signals, and fine frequency resolution for long duration and lower frequency signals, are needed. The

combination of different windows in one representation is one of the motivations for the move to the wavelet domain.

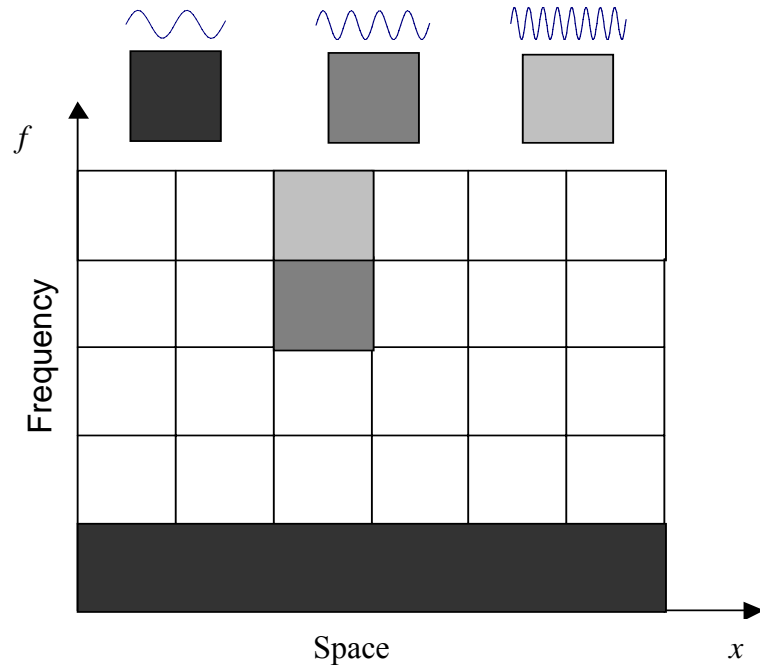


Figure 3.1: Windowed Fourier transforms [after Robertson et al., 1996]

The double integrals introduced in Chapter Two are solved by convolution “*”. *Convolution* is defined as the operation of filtering one of the functions by the other, as follows [Sideris, 1984]:

$$g(k,l) = h(k,l) * q(k,l) = \sum_{i=0}^{M_x-1} \sum_{j=0}^{M_y-1} h(i,j) q(k-i,l-j) \Delta x \Delta y \quad (3.12)$$

One of the main properties of the DFT is that convolution in the space domain is equivalent to multiplication in the Fourier (frequency domain) and use of inverse Fourier transform. Consequently, equation (3.12) is solved by two direct and one inverse Fourier transforms as follows [Sideris, 2005]:

$$g(k,l) = F_2^{-1} \{ F_2 \{ h(k,l) \} F_2 \{ q(k,l) \} \} \quad (3.13)$$

3.2 The wavelet transform

Wavelets are of interest in signal processing because of their localization properties. The use of the wavelet transform to decompose and reconstruct a one-dimensional signal requires the evaluation of single and double integrals, respectively. Wavelets have to fulfill a number of properties: e.g., have zero average, be normalized, oscillate, decay, and tend to zero with the increase of distance [Keller, 2004].

3.2.1 Continuous wavelet transform

In Section 3.1, the analyzing function was sinusoidal for the WDFT. The main drawback is its fixed envelope in the space and the frequency domain. This raises the interest in the wavelet transform and its localization properties. In the case of the continuous wavelet transform, the analyzing function is filled with oscillation, but the big difference from WDFT is the change of the envelope shape with the change of the scale. The shorter the scale, the more compressed is the envelope and the higher the frequency to be detected. The wavelets have a high space resolution for high frequencies and a low space resolution for low frequencies.

The continuous Wavelet Transform (CWT) of a signal $q(x)$ is defined as the inner product of the signal sequence with the family (analyzing) functions $\psi(x)$ [Goswami and Chan, 1999], as

$$Q_W(m, x_n) = \frac{1}{\sqrt{m}} \int_{-\infty}^{\infty} q(x) \bar{\psi}\left(\frac{x-x_n}{m}\right) dx \quad (3.14)$$

and the inverse CWT is as follows:

$$q(x) = \frac{1}{C_\psi} \int_{-\infty}^{\infty} \int_{-\infty}^{\infty} \frac{1}{\sqrt{m}} Q_W(m, x_n) \psi\left(\frac{x-x_n}{m}\right) dx_n \frac{dm}{m^2} \quad (3.15)$$

where m is the scale that determines the oscillating behaviour of a particular daughter wavelet, x_n is the shifting of the mother wavelet or the daughter wavelet (important for having space localization information of the original signal), C_ψ is the admissibility

constant, and $\bar{\psi}$ is the complex conjugate of ψ . The analyzing function $\psi(x)$ is not limited to the complex exponential as is the case of the Fourier transform. In fact, the only restriction on $\psi(x)$ is that it must be short and oscillatory to guarantee the localization properties. This restriction ensures that the integral is finite and leads to the wavelet transform, and $\psi(x)$ is named the mother wavelet. This mother wavelet dilates (or compresses) and translates simply as wavelets or daughter wavelets [Mallat, 1989].

The definition of the CWT shows that the wavelet analysis is a measure of the similarity between the basis function (wavelets) and the signal itself. The calculated coefficients refer to the closeness of the signal to the wavelet of the current scale. The determination of the CWT coefficients of a signal starts by using the most compressed wavelet that can detect the highest frequencies existing in that signal. This starts by choosing a scale value that represents the original signal. Then, the wavelet is shifted by x_n along the space axis until the end of the signal. The next step is to increase the scale m by some amount (thus expanding the wavelet window to detect lower frequencies) and repeat the shifting procedure. The whole procedure is repeated for each value of m until some “maximum” desired value of m is reached [Strang, 1989; Daubechies, 1990].

In a practical implementation of the CWT, there will be redundant information, because the wavelet coefficients are calculated for every possible scale, which will, of course, lead to a large amount of work and yield a lot of redundancy. It also presents difficulties in its practical application. For ease of computer implementation, the discrete wavelet transform (DWT) is implemented, which will be discussed in the next subsection.

3.2.2 Discrete wavelet transform

For the wavelet transform numerical implementation, a discrete procedure is required. The dyadic wavelets developed by Daubechies [1992] are the core of this implementation. A family of wavelet functions (daughter wavelets) is generated from a single prototype wavelet (mother wavelet). Although two-dimensional wavelets are used

in the evaluation of geodetic integrals, their implementation is based on the one-dimensional wavelet transform in two directions.

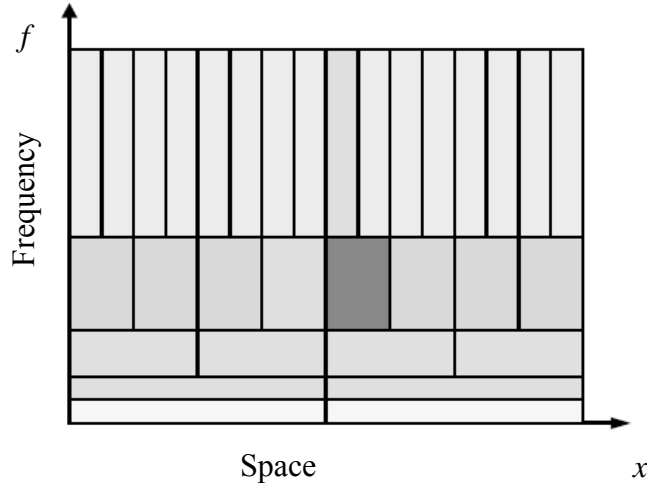


Figure 3.2: Discrete wavelet Transform [after Griffiths et al., 1997].

Every one-dimensional signal q can be represented using wavelet base functions as follows [Heil and Walnut, 1989; Chan, 1995; Torrence and Compo, 1998]:

$$q(x) = \sum_{m \in \mathbb{Z}} \sum_{n \in \mathbb{Z}} d_n^m \psi_{m,n}^{(\lambda_0, x_0)}(x) \quad (3.16)$$

where

$$d_n^m = \langle q(x), \psi_{m,n}^{(\lambda_0, x_0)} \rangle = \int q(x) \psi_{m,n}^{(\lambda_0, x_0)}(x) \quad (3.17)$$

$$\psi_{m,n}^{(\lambda_0, x_0)}(x) = \lambda_0^{-m/2} \psi(\lambda_0^{-m} x - n x_0) \quad (3.18)$$

d_n^m are detailing coefficients, $\psi_{m,n}$ is the wavelet function generated from the original mother wavelet function $\psi \in L^2(\mathbb{R})$, λ_0 is the scale space parameter, x_0 is the translation space parameter, m is the scale or level of decomposition integer, and n is the shifting or translation integer.

The scale and translation parameters form a wavelet frame, where the signal is completely represented by its spectrum (Figure 3.2). The representation is on a dense grid for small scales and on a wide grid for large scales. For practical reasons, a dyadic frame is used here with $\lambda_0 = 2$ and $x_0 = 1$. As mentioned before, the main drawback of the traditional decomposition of the CWT is the redundancy. The dyadic frame reduces this redundancy effectively. The coefficients for the scale m are recursively computed from scale $m-1$, which is the core of Mallat's algorithm [Mallat, 1998].

3.2.3 Multi-resolution analysis on wavelet basis

The concept of multi-resolution analysis (MRA) is introduced for the construction of orthogonal wavelet bases and for the fast decomposition of a signal into independent frequency bands through a nested sequence, as follows (Figure 3.3) [Keller, 2004]:

$$0 \subset \dots \subset V_2 \subset V_1 \subset V_0 \subset V_{-1} \subset \dots \subset L_2(\mathfrak{R}) \quad (3.19)$$

where

$$\overline{\bigcup_{m \in \mathbb{Z}} V_m} = L_2(\mathfrak{R}) \quad (3.20)$$

$$\bigcap_{m \in \mathbb{Z}} V_m = \{0\} \quad (3.21)$$

$$q(\bullet) \in V_m \Leftrightarrow q(2^m \bullet) \in V_0 \quad (3.22)$$

and the scaling function $\varphi_{m,n} \in L_2(\mathfrak{R})$ with

$$V_0 = \overline{\text{span}\{\varphi(\bullet - k) | k \in \mathbb{Z}\}} \quad (3.23)$$

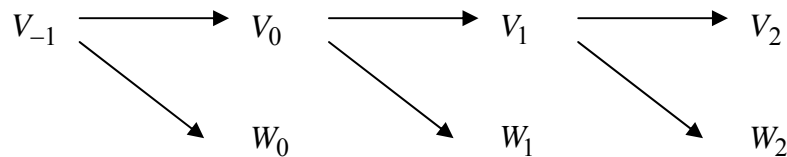


Figure 3.3: Multi-resolution analysis using nested sequence

Equation (3.19) and Figure 3.3 illustrate that all spaces of the MRA are a scaled version of the original space V_{-1} , which is spanned by a shifted version of the scaling function $\varphi_{m,n}$ into other V spaces (approximation) and the wavelet function $\psi_{m,n}$ into W spaces (detailing). Consequently, in addition to Equation (3.16), another inner product is used for the decomposition of the signal q using scaling functions $\varphi_{m,n}$ as

$$c_n^m = \langle q, \varphi_{m,n} \rangle = \int q(x) \varphi_{m,n}(x) dx \quad (3.24)$$

where c_n^m are the approximation coefficients.

From Equations (3.16) and (3.24), which form the wavelet frame, it can be seen that the signal is always represented by an approximation c_n^m and a detailed d_n^m part.

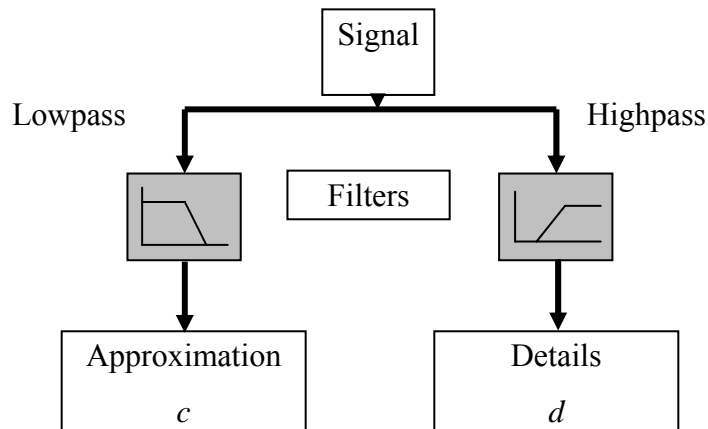


Figure 3.4: Low and high pass wavelet filters

A number of scaling coefficients (lowpass filter) h_n represent the scaling function, which is the base of space V_0 . That is,

$$\varphi(x) = \frac{1}{\sqrt{2}} \sum_{n \in \mathbb{Z}} h_n \varphi(2x - n) \quad (3.25)$$

The base of W_0 is represented by the detailing function ψ , where

$$\psi(x) = \sqrt{2} \sum_{n \in \mathbb{Z}} g_n \varphi(2x - n) \quad (3.26)$$

ψ is the wavelet function that is generated from the original mother wavelet function, and g_n are the detailed coefficients (highpass filter). Both filters are illustrated in Figure 3.4.

The relation between the scaling coefficients and detailed coefficients is

$$g_n = (-1)^n h_{1-n} \quad (3.27)$$

The wavelet procedure used is based on the Mallat algorithm, which consists of the following two equations [Mallat, 1998; Keller, 2004]:

$$c_n^m = \langle f, \varphi_{m,n} \rangle = \sum_{l \in \mathbb{Z}} h_l \langle f, \varphi_{m-1, 2n+l} \rangle = \sum_{l \in \mathbb{Z}} h_{l-2n} c_l^{(m-1)} \quad (3.28)$$

$$d_n^m = \langle f, \psi_{m,n} \rangle = \sum_{l \in \mathbb{Z}} g_l \langle f, \varphi_{m-1, 2n+l} \rangle = \sum_{l \in \mathbb{Z}} g_{l-2n} c_l^{(m-1)} \quad (3.29)$$

These two equations help in the fast computations of the wavelet coefficients of a given signal q that belong to V_{-1} ; the scheme is shown in Figure 3.5.

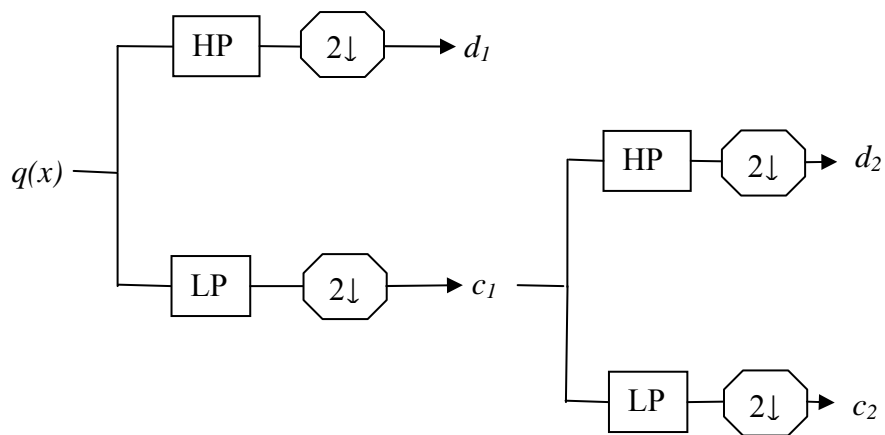


Figure 3.5: Block diagram of the one-dimensional wavelet decomposition

For the two-dimensional wavelet transform, the Mallat algorithm will go through a tensor product of two different directional one-dimensional wavelet transforms. Consequently, the two-dimensional wavelet transform can be derived from its one-dimensional counterparts [Chui et al., 1994; Mallat, 1998] as follows:

$$\varphi(x, y) = \varphi(x) \varphi(y) \quad (3.30)$$

$$\psi^H(x, y) = \psi(x) \varphi(y) \quad (3.31)$$

$$\psi^V(x, y) = \varphi(x) \psi(y) \quad (3.32)$$

$$\psi^D(x, y) = \psi(x) \psi(y) \quad (3.33)$$

Thus, the two-dimensional Mallat algorithm is (Figure 3.6)

$$c_n^m = \sum_{l_x \in z} h_{l_x-2n_x} \sum_{l_y \in z} h_{l_y-2n_y} c_l^{(m-1)} \quad (3.34)$$

$$d_n^{H^m} = \sum_{l_x \in z} g_{l_x-2n_x} \sum_{l_y \in z} h_{l_y-2n_y} c_l^{(m-1)} \quad (3.35)$$

$$d_n^{V^m} = \sum_{l_x \in z} h_{l_x-2n_x} \sum_{l_y \in z} g_{l_y-2n_y} c_l^{(m-1)} \quad (3.36)$$

$$d_n^{D^m} = \sum_{l_x \in z} g_{l_x-2n_x} \sum_{l_y \in z} g_{l_y-2n_y} c_l^{(m-1)} \quad (3.37)$$

where

$$l = (l_x, l_y), \quad n = (n_x, n_y) \quad (3.38)$$

The distribution of the four sets of coefficients (Equations (3.34) to (3.37)) is shown in the following figure.

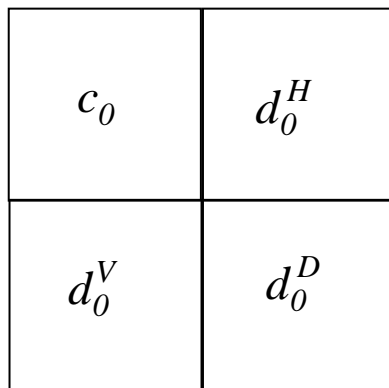


Figure 3.6: One level of decomposition of the two-dimensional wavelet transform of a grid of data

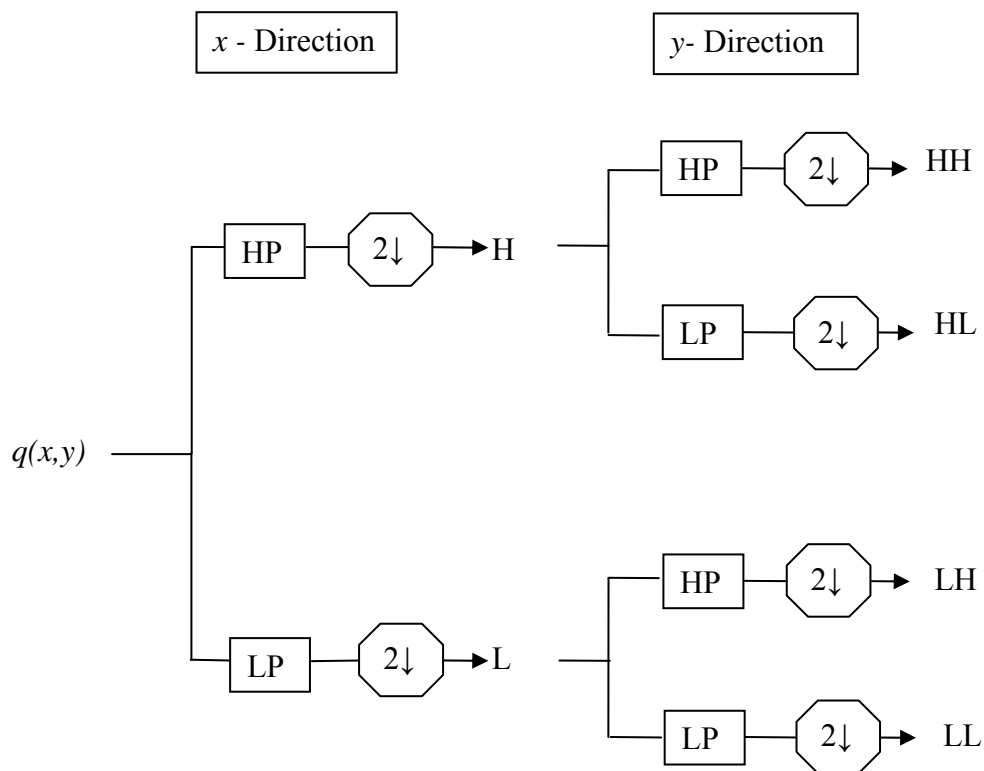


Figure 3.7: Block diagram of the two-dimensional wavelet decomposition algorithm

Figure 3.7 is a block diagram illustrating the two-dimensional wavelet transform. The highpass and lowpass filters are applied first in the x direction with down sampling (dyadic intervals). Then, through the tensor product, the highpass and lowpass filters are applied in the other direction (y direction). This leads to four sets of wavelet coefficients: high high (HH), high low (HL), low high (LH), and low low (LL).

3.3 Wavelet thresholding

Thresholding is the most common processing tool in wavelet multi-resolution analysis. The wavelet thresholding technique was mainly developed for removing noise and outliers, compression, and pattern recognition of the signal before wavelet reconstruction. In this thesis, two thresholding methods are presented: hard thresholding and soft thresholding. The former is for matrix compression and the latter for de-noising signals.

3.3.1 Hard thresholding compression

Hard thresholding is like a gate. If a value is below a certain thresholding value, it is set to zero. The same algorithm is used for the compression of matrices. Wavelet coefficients (absolute) larger than a certain specified threshold δ are the ones that should be included in the reconstruction. The reconstructed function can be expressed as [Ogden, 1997]:

$$\hat{q}(x) = \sum_m \sum_n I_{\{|d_n^m| > \delta\}} d_n^m \psi_{m,n} \quad (3.39)$$

where $I_{\{|d_n^m| > \delta\}}$ is the indicator function of this set. This function represents a keep or kill wavelet reconstruction; it assumes the value of one for the coefficients required in the reconstruction process (keep) and zero for the coefficients that should be removed (kill).

The hard thresholding is a kind of nonlinear operator on the wavelet coefficients' vector and leads to a resultant vector of the estimated coefficients \hat{d}_n^m , which can be involved in the reconstruction process, as follows [Barthelmes et al., 1994]

$$\hat{d}_n^m = \begin{cases} d_n^m, & \text{if } |d_n^m| \geq \delta \\ 0, & \text{otherwise} \end{cases} \quad (3.40)$$

The graphical representation of the hard thresholding is shown in Figure 3.8. It can be seen that the graph is non-linear and discontinuous [Goswami and Chan, 1999].

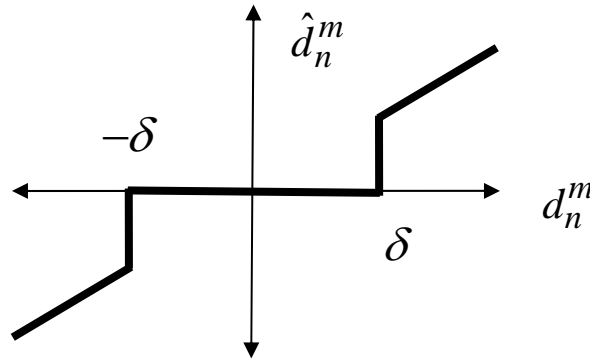


Figure 3.8: Hard thresholding

In making the decision, the problem is always about the thresholding value. In order to make this decision, one main parameter has to be taken into consideration: the wavelet coefficients of the first level of decomposition. Then, the estimated value of the median of the detailed wavelet coefficients can be used as a starting point for the compression of the matrices. Higher values than this estimated threshold can be used, depending on the degree of approximation required and the accuracy specification. Choosing the correct value of the threshold is a very important to avoid over smoothing or under smoothing. After testing different methods, such as the minimax method [Donoho and Johnstone, 1998], for the estimation of the thresholding value, the thresholding value is selected as follows [Donoho and Johnstone, 1994; Gao, 1997]:

$$\delta = \text{median}(|\text{detailed wavelet coefficients at level one}|) \quad (3.41)$$

If this is equal to zero, then

$$\delta = \frac{1}{20} * \max(|\text{detailed wavelet coefficients at level one}|) \quad (3.42)$$

The reason behind this choice is that this method achieved the best results in comparison to reference data in the compression and de-noising cases. The inversion of the Stokes integral will be evaluated numerically in Chapters Four and Six. Equations (3.41) and (3.42) assumes that for a piecewise smooth signal the noise will mainly be represented on the finest wavelet scale, the first wavelet decomposition detailed coefficients, leading to a simple method for the estimation of the thresholding values. This estimation will rely mainly on the median of the detailed coefficients of the finest wavelet decomposition [Donoho and Johnstone, 1994].

3.3.2 Soft thresholding de-noising

Soft thresholding is defined as

$$\hat{d}_n^m = \begin{cases} d_n^m - \delta', & \text{if } |d_n^m| \geq \delta' \\ 0 & , \text{if } |d_n^m| \leq \delta' \\ d_n^m + \delta', & \text{if } |d_n^m| < -\delta' \end{cases} \quad (3.43)$$

From Figure 3.9, it can be seen that it is generally linear (straight line with slope to be determined). Soft thresholding is used in de-noising signals hidden in background noise. The main objective is to attenuate the noise while amplifying the signal. The determination of the thresholding value is as follows [Donoho, 1995]:

$$\delta' = \delta \sqrt{2 \log(\text{dim}_1 \times \text{dim}_2)} / 0.6745 \quad (3.44)$$

where δ is computed from Equations (3.41) or (3.42), dim_1 and dim_2 are the two dimensions of the matrix, and 0.6745 is a value obtained from Gaussian calibration, assuming that the wavelet coefficients are normally distributed [Donoho and Johnstone, 1994].

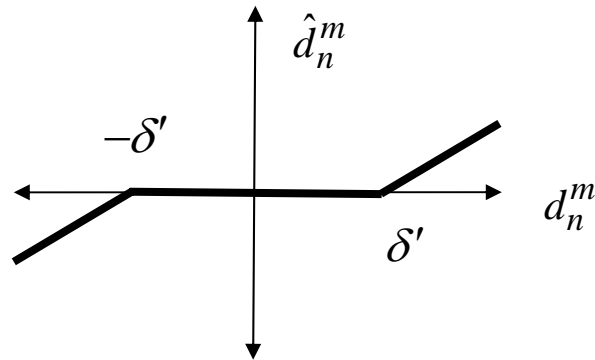


Figure 3.9 Soft thresholding

3.4 Standard and non-standard wavelet representation of operators

The wavelet bases in two-dimensional space can be constructed as a tensor product of the one-dimensional wavelet transform. Representing operators in such bases leads to the standard form [Beylkin et al., 1991]. Conversely, the non-standard representation is constructed using the scaling approximation function in addition to the wavelets' detailing functions. Beylkin [1992] developed a numerical algorithm that depended on the non-standard representation for fast computations of operators.

The algorithm is used for the representation of the integral operators of the form

$$s(x_p) = \int K(x_p, x) q(x) dx \quad (3.45)$$

The algorithm requires the one-dimensional wavelet transform of the data $q(x)$. The approximation part from the scaling coefficients is

$$c_{n \ q}^m = \langle q(x), \varphi_{m,n} \rangle = \int q(x) h_m(x) dx \quad (3.46)$$

The detailed part is from the wavelet detailing coefficients:

$$d_{n \ q}^m = \langle q(x), \psi_{m,n} \rangle = \int q(x) g_m(x) dx \quad (3.47)$$

The two-dimensional wavelet transform of the kernel is given by

$$c_{n \ K}^m = \iint K(x_p, x) h_m(x_p) h_m(x) dx_p dx \quad (3.48)$$

$$d_{nK}^{Hm} = \iint K(x_p, x) h_m(x_p) g_m(x) dx_p dx \quad (3.49)$$

$$d_{nK}^{Vm} = \iint K(x_p, x) g_m(x_p) h_m(x) dx_p dx \quad (3.50)$$

$$d_{nK}^{Dm} = \iint K(x_p, x) g_m(x_p) g_m(x) dx_p dx \quad (3.51)$$

Equations (3.48) to (3.51) are combined to represent the kernel on wavelet bases

$$\begin{aligned} K(x_p, x) = & \sum \sum c_{nK}^m h_m(x_p) h_m(x) + \sum \sum d_{nK}^{Hm} h_m(x_p) g_m(x) \dots \\ & + \sum \sum d_{nK}^{Vm} g_m(x_p) h_m(x) + \sum \sum d_{nK}^{Dm} g_m(x_p) g_m(x) \end{aligned} \quad (3.52)$$

Equation (3.52) is substituted in Equation (3.45) and yields

$$\begin{aligned} s(x_p) = & \int [\sum \sum c_{nK}^m h_m(x_p) h_m(x) + \sum \sum d_{nK}^{Hm} h_m(x_p) g_m(x) \\ & + \sum \sum d_{nK}^{Vm} g_m(x_p) h_m(x) + \sum \sum d_{nK}^{Dm} g_m(x_p) g_m(x)] q(x) dx \end{aligned} \quad (3.53)$$

Interchanging the integration and summation in Equation (3.53) and using Equations (3.46) and (3.47), Equation (3.45) is represented on a wavelet basis as

$$s(x_p) = \sum [c_{nK}^m c_{nq}^m + d_{nK}^{Hm} d_{nq}^m] h_m + \sum [d_{nK}^{Vm} c_{nq}^m + d_{nK}^{Dm} d_{nq}^m] g_m \quad (3.54)$$

The implementation here is for one-dimensional integrals like Equation (3.45). One-dimensional wavelet transform is required for the signal (Equations (3.46) and (3.47)) and two-dimensional wavelet transform is required for the kernel (Equations (3.48) to (3.51)). All the geodetic problems introduced in Chapter Two are two-dimensional integrals. The wavelet evaluation of these double integrals requires the extension of the Beylkin et al. [1991] algorithm to higher dimensions. Consequently, two-dimensional wavelet transform is required for the signal and four-dimensional wavelet transform for the kernel [Salamonowicz, 2000; Keller, 2002].

3.5 Implementation of the wavelet algorithm for geodetic integrals

In this thesis, a new implementation of the Beylkin et al. [1991] algorithm is developed for the wavelet representation of two-dimensional geodetic integrals.

Orthogonal wavelets are used in this implementation. The direct geodetic integrals can be generally formulated as follows:

$$s(x_p, y_p) = c \iint_E K(x_p, y_p, x, y) q(x, y) dx dy \quad (3.55)$$

where

s is the signal, K is the kernel (depending on the application), x_p, y_p, x, y are the local Cartesian coordinates of the computational points and the data points, q is the gridded data, and c is a constant (which changes according to the application).

The procedure used to evaluate the geodetic integrals is a combination of Beylkin's [1992] non-standard algorithm for fast wavelet computations of linear operators (Equations (3.45) to (3.54) and Mallat's algorithm Equations (3.34) to (3.37).

The procedure is described in the following steps:

The first step is the wavelet transform of the gridded data q :

$$\begin{aligned} c_q &= \iint q(x, y) \varphi(x) \varphi(y) dx dy \\ d_q^H &= \iint q(x, y) \varphi(x) \psi(y) dx dy \\ d_q^V &= \iint q(x, y) \psi(x) \varphi(y) dx dy \\ d_q^D &= \iint q(x, y) \psi(x) \psi(y) dx dy \end{aligned} \quad (3.56)$$

The second step is the wavelet transform of the kernel:

$$\begin{aligned} c_K &= \iint K(x_p, y_p, x, y) \varphi(x) \varphi(y) dx dy \\ d_K^H &= \iint K(x_p, y_p, x, y) \varphi(x) \psi(y) dx dy \\ d_K^V &= \iint K(x_p, y_p, x, y) \psi(x) \varphi(y) dx dy \\ d_K^D &= \iint K(x_p, y_p, x, y) \psi(x) \psi(y) dx dy \end{aligned} \quad (3.57)$$

The kernel is represented on wavelet basis using the wavelet decomposition coefficients and the approximation and the detailing coefficients of Equation (3.57), as follows:

$$\begin{aligned}
K = & \sum \sum c_K h(x)h(y) + \sum \sum d_K^H h(x)g(y) + \sum \sum d_K^V g(x)h(y) + \\
& \dots \sum \sum d_K^D g(x)g(y)
\end{aligned} \tag{3.58}$$

The summation is over dyadic intervals to avoid redundancy and decrease the computational effort. This reconstructed kernel formula (Equation (3.58)) is substituted in the general geodetic integral formula (Equation (3.55)) to yield the following equation:

$$\begin{aligned}
s(x_p, y_p) = & c \iint [\sum \sum c_K h(x)h(y) + \sum \sum d_K^H h(x)g(y) \\
& + \sum \sum d_K^V g(x)h(y) + \sum \sum d_K^D g(x)g(y)] q(x, y) dx dy
\end{aligned} \tag{3.59}$$

where

$s(x_p, y_p)$ is the solution at one computational point (signal).

By interchanging the order of the integration and the summation and subsequently integrating, the solution takes the following form:

$$s(x_p, y_p) = c (\sum \sum c_K c_q + \sum \sum d_K^H d_q^H + \sum \sum d_K^V d_q^V + \sum \sum d_K^D d_q^D) \tag{3.60}$$

This can be summarized as the element-by-element multiplication of the two-dimensional wavelet transform coefficients of the kernel and the data. The product output matrix is then summed up to get the results (signal) directly at the computational points. It should be mentioned that because of the orthogonal wavelets used, the step of inverse wavelet transform is done implicitly; therefore, there is no need to do it in a separate step. Consequently, using this algorithm, which skips this inverse step, decreases the computational effort. In fact, it will save 30% of the computations required by the standard algorithms.

Two different implementations of this procedure can be used. The first is the point-wise solution, where each unknown value $s(x_p, y_p)$ can be computed by multiplying the two-dimensional wavelet coefficients matrix of the kernel corresponding to this computational point with the two-dimensional wavelet coefficients matrix of the data $q(x, y)$ (known). Summing up the elements of the output matrix will lead directly to

the solution at one single point [Salamonowicz, 2000]. This procedure is extremely time consuming; however, it can be used successfully for evaluations over large areas on simple PCs.

Another approach can be implemented to overcome the extensive mathematical effort and decrease the time required. The problem is reformulated in the form of the following equation:

$$b_i = A_{ij} a_j \quad (3.61)$$

where

A_{ij} is the design matrix containing the wavelet coefficients of the wavelet transform of the kernels $K(x_p, y_p, x, y)$, a_j is a vector containing the wavelet coefficients of the data q , and b_i is a vector containing the unknown signal (results) s . In this approach, the design matrix A is first allocated in memory. Each row of this matrix contains the full coefficients of the kernel of one computational point as shown in Figure 3.10. The wavelet coefficients of the data are arranged in the column vector a_j , as shown in Figure 3.11.

Reallocating the design matrix A in memory speeds up the time required for the computations in comparison with the point-wise solution. However, the problem is in the large memory requirement for solving the problem, even for a small grid. For example, an area consisting of a grid of 64×64 elements requires allocating a matrix of 4096×4096 elements, which can be a problem for personal computers. Therefore, both approaches, the point-wise solution and the solution found by reallocating the design matrix in memory, yield unfavourable computation times compared to other spectral methods such as FFT. However, the numerous beneficial wavelet properties, like the localization properties and powerful capability to deal with non-stationary noise, prompted our effort to overcome the two previously mentioned problems (time and memory).

The solution of these two problems is derived through the combination of the wavelet thresholding techniques (Section 3.3.1) and the reallocation of the design matrix

in the memory. This combination aims to decrease the memory required for the design matrix and speed up the computations by decreasing the number of multiplications required.

The inversion of geodetic integrals is evaluated by the developed wavelet algorithm (Equation (3.61)) combined with an optimization procedure. In this case, the a_j vector will contain the unknown wavelet coefficients of the data q , b_i will be a vector containing the known signal. The problem is solved using the simple conjugate gradient method. The system of linear equations, Equation (3.61), has a nonsymmetric and possibly not positive definite coefficient matrix. It is obvious that the system has to be changed to a symmetric positive definite system. This is done by the formation of the normal equations as follows:

$$A_{ij}^T b_i = A_{ij}^T A_{ij} a_j \quad (3.62)$$

or

$$M_j = N_{jj} a_j \quad (3.63)$$

where $M_j = A_{ij}^T b_i$ and $N_{jj} = A_{ij}^T A_{ij}$.

The method starts with approximate values for the unknowns. It then proceeds by generating successive approximations to the solution, and the residuals corresponding to these iterations are computed. A linear search direction updates the iterations and the residuals. The iteration proceeds until the ratio between the $norm(M_j - N_{jj} a_j^{iter.})$ and $norm(M_j)$ is less than the predefined tolerance value. More details about the conjugate gradient algorithm can be found in Barrett et al. [1994]. The solution vector a_j is the output from the conjugate gradient iterative method. Two-dimensional inverse wavelet transform is applied to a_j to obtain the required data.

The combined wavelet-optimization algorithm for the inversion of the geodetic integrals is summarized in the following steps:

- The design matrix A is built by the two-dimensional wavelet transform of the kernels at all the computational points, as shown in Figure 3.10.
- The signal (known) vector b_i is built.
- The normal equations are formed and the solution a_j is obtained by the conjugate gradient method.
- Two-dimensional inverse wavelet transform is applied to a_j (Figure 3.11) after transforming it into a matrix to obtain the final data required at all the computational points.

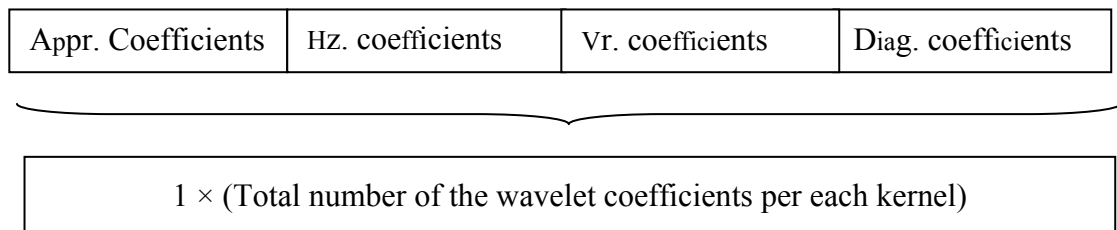


Figure 3.10: The structure of the row vector representing each kernel required for the design matrix A

3.6 Methodology of investigation

In the current study, the new implementation of the wavelet transform for solving the geodetic operators (Section 3.5) is tested. The geodetic operators are divided into direct geodetic integrals, inverse geodetic integrals, and the inversion of geodetic integrals. The efficiency of the wavelet evaluation methods is studied. The efficiency is determined through testing several testing parameters, such as the accuracy, speed, and memory required for allocating the matrices of the wavelet algorithm. Several wavelet thresholding cases are tested to reach the most efficient implementation for each integral. The wavelet full matrix solution is introduced first. Then, a number of global thresholding values are tested to reach the maximum compression level with an acceptable practical accuracy.

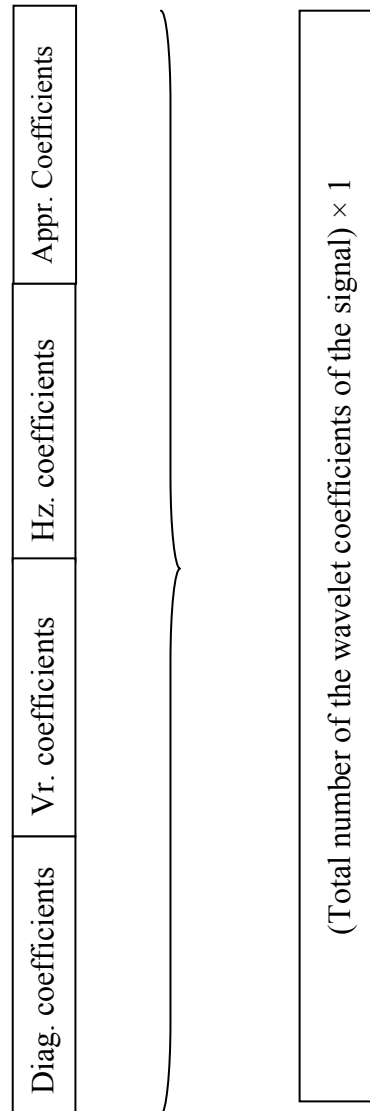


Figure 3.11: The structure of the column vector a_j representing the wavelet coefficients matrix of the data q

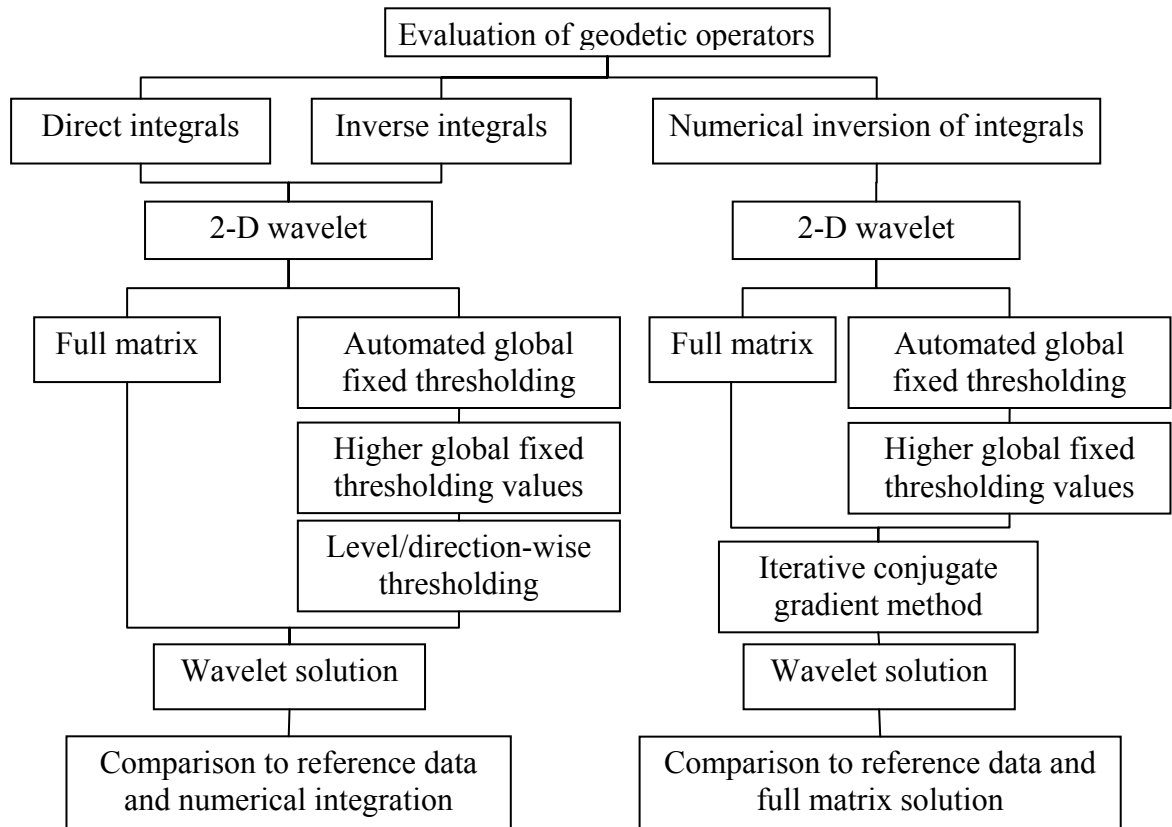


Figure 3.12: Methodology of investigation

Finally, a level/direction-wise thresholding technique is used to optimize the compression level reached while maintaining the target accuracy of each application. The efficiency of the direct and inverse geodetic integrals wavelet solutions is evaluated through a comparison to the FFT and the numerical integration solutions. In addition, a comparison to the reference data will be done, where such data are available. For the case of the inversion of geodetic integrals, the efficiency is tested through a comparison to the reference data. The three different wavelet implementations, mentioned before, will evaluate all integrals. The methodology of investigation is summarized in Figure 3.12.

3.7 Summary

The wavelet transform was introduced as an alternative spectral technique for the representations of geodetic operators. The main properties of the wavelet transform have

been briefly summarized in this chapter. Since the Fourier transform is the main spectral technique that is extensively used in the representation of different geodetic operators, the chapter started with an overview of the Fourier transform with its properties. A new implementation of the Beylkin et al. [1991] algorithm is developed for the wavelet representation of two-dimensional geodetic integrals. The development is through the extension of the algorithm from one to two-dimensions. A hard thresholding technique is introduced for the matrix compression and soft thresholding for de-noising signals.

Chapter Four: Applications of wavelets as analysis, compression, and de-noising tools

In this chapter, the numerical implementation of the wavelet theory presented in the previous chapter is introduced. The problem of the choice of the right wavelet family to suit the application and the implementation to be used are studied. Three main applications are presented: analysis and localization properties of wavelets, compression by hard thresholding, and de-noising by soft thresholding. The three applications are presented in one and two dimensions.

4.1 Selection of compactly supported orthogonal wavelets

One of the main points to be discussed is how to choose the wavelet from the large number of mother wavelets that are available now. As a preliminary choice, it can be said that the choice of the mother wavelet depends on the study of the previous trials done by different researchers and trying to find a way to a choice that satisfies a specific application. In other words, the researcher's experience helps him or her make the correct choice of which mother wavelet should be used in analyzing certain data for a certain application. Also, testing different wavelets can help in finding the right one that will give minimum value for the coefficients (non-zero coefficients), which can help in the compression or improve the efficiency of de-noising.

Most of the publications on wavelet bases exploit their ability to efficiently approximate a particular function that is used in particular applications with a few non-zero wavelet coefficients (sparse matrices). This is important not only for data compression but also for noise removal and fast matrix computations. The choice of the mother wavelet must therefore be optimized to produce a maximum number of wavelet coefficients that are close to zero. Generally, most of the functions have small wavelet coefficients at fine scale (high resolution) decompositions. This depends mostly on the regularity of this function, the number of the mother wavelet's vanishing moments, and the size of its support.

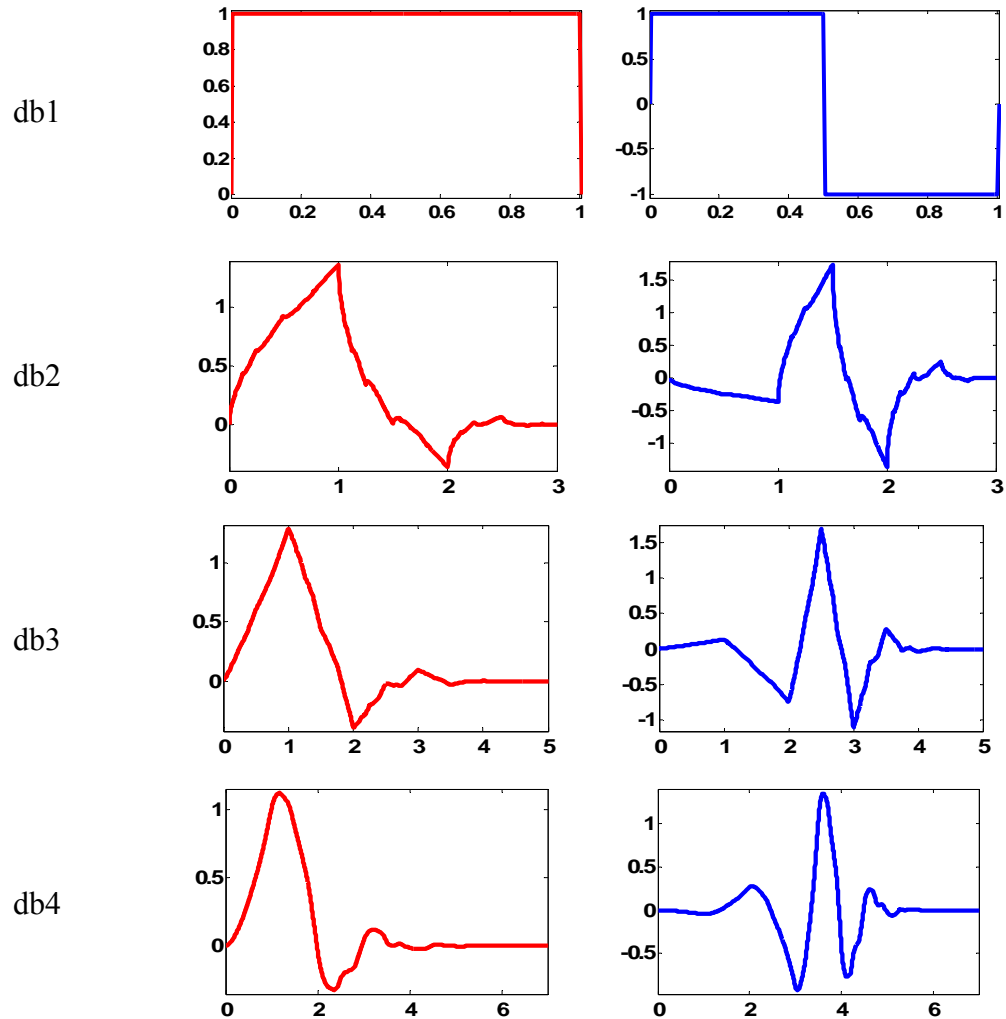


Figure 4.1: Daubechies wavelets (db): scaling function (red) and wavelet function (blue)

The choice of the wavelet family in the current thesis will be from the properties required for the wavelet representation of geodetic operators. The Beylkin et al. [1991] algorithm introduced in Section 3.4 requires orthogonal wavelets. Mallat's algorithm for the multi-resolution analysis is useful only if the wavelet filters h and g are finite and compact support. The ideal choice for fulfilling the three properties—orthogonal, finite, and compact support—is the Daubechies wavelets. The method for constructing such wavelets is found in Daubechies [1988]. The construction algorithm generates the scaling coefficients h and consequently g (Equation (3.27)). The Mallat algorithm is used for the

reconstruction of different wavelets from their scaling coefficients. The construction theory is rather complicated and is beyond the scope of this thesis. The inverse Mallat algorithm allows the reconstruction of the signal from the corresponding wavelet coefficients [Mallat, 1998]. Detailed wavelet coefficients for Daubechies wavelets can be found in a numerous references, such as Daubechies [1992], Daubechies [1988], and Keller [2004]. Figure 4.1 shows part of Daubechies' (db) wavelet family with vanishing moments from one to four.

The Meyer wavelet is used in de-noising the gravity disturbance from an airborne gravimetry experiment. Both the scaling and the wavelet functions are defined in the frequency domain, starting with an auxiliary function [Meyer, 1992]. The Meyer family is orthogonal. Although the Meyer family does not have finite support, the wavelet function decreases dramatically to zero when the input goes to infinity, faster than many other functions; this leads to a compactly supported wavelet (Figure 4.2).

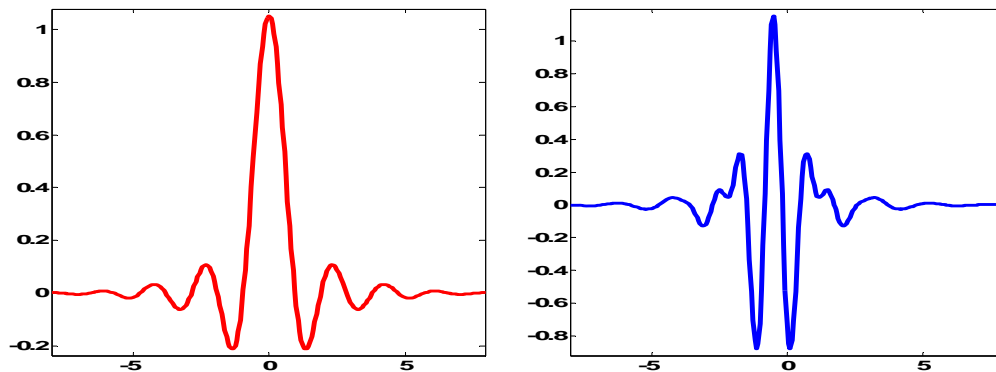


Figure 4.2: Meyer scaling function (red) and wavelet (blue).

4.2 Examples of analysis and localization properties

The main advantage of wavelet transform (Section 3.2) over the other spectral techniques, such as fast Fourier transforms, is its localization property [Daubechies, 1990; Keller, 2004]. The analysis and localization properties of the wavelet transform are demonstrated in one and two dimensions in the following subsections.

4.2.1 One-dimensional analysis of airborne gravimetry data

The one-dimensional wavelet analysis is applied to an airborne gravimetry application. The data used originates from a project collected by the University of Calgary on three days: September 9, 10, and 11, 1996. Only the data from the second day are tested in this thesis. The data was collected over the Rocky Mountains; the area covered was $100 \text{ km} \times 100 \text{ km}$ [Glennie and Schwarz, 1997]. This area was covered by 14 lines on the second day, as shown in Figure 4.3. The data analyzed is a gravity disturbance introduced as a sub-output from the KINGSPAD software [Glennie, 1999].

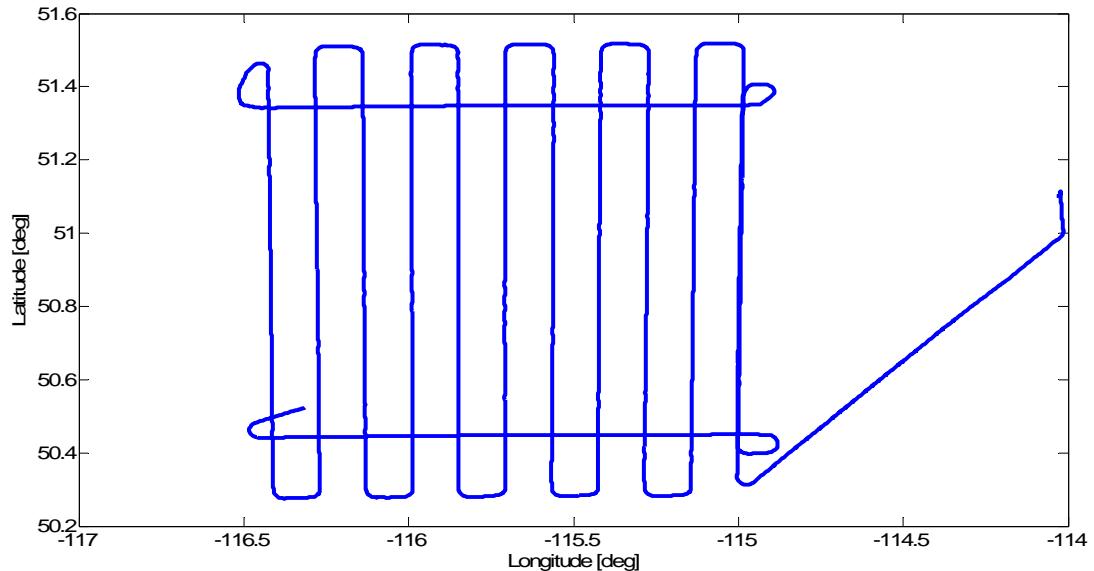


Figure 4.3: Flight pattern for the second day of the University of Calgary test over the Rocky Mountains

The gravity disturbance (Figure 4.4) analysis starts with the spectrum of the signal using Fourier analysis. The FFT was used to visualize the different frequency contents of the signal. The spectrum in Figure 4.5 shows that there are different errors at different frequencies, but the problem is that it is difficult to localize where these errors are.

The use of the continuous wavelet transform introduces time-frequency localization; this can be seen in Figure 4.6. Darker shades show large errors at a certain time and scale. For example, the takeoff and different manoeuvre periods between lines

can be easily identified in comparison to those in Figure 4.3. Each manoeuvre to turn from line to line can be easily recognized. In wavelet analysis, different types of errors can be tracked through the whole trajectory and interpreted in correspondence with different aircraft dynamics. Also, by the decomposition of the signal into several levels, stochastic errors and outliers can be detected and removed using a soft thresholding technique [Elhabiby and Sideris, 2006b]. This is discussed in Section 4.4.1.

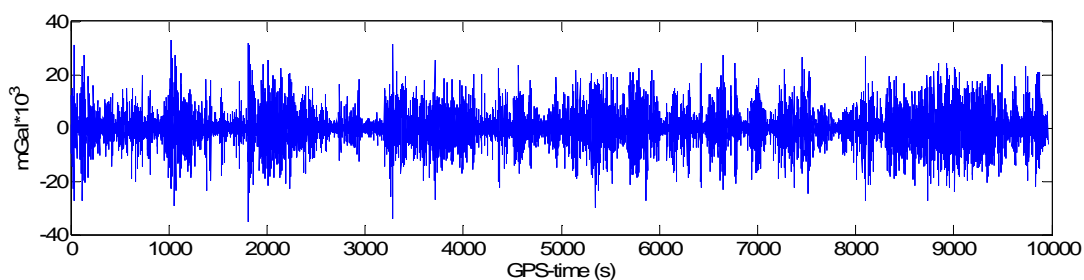


Figure 4.4: Gravity disturbance with 1 Hz sampling rate

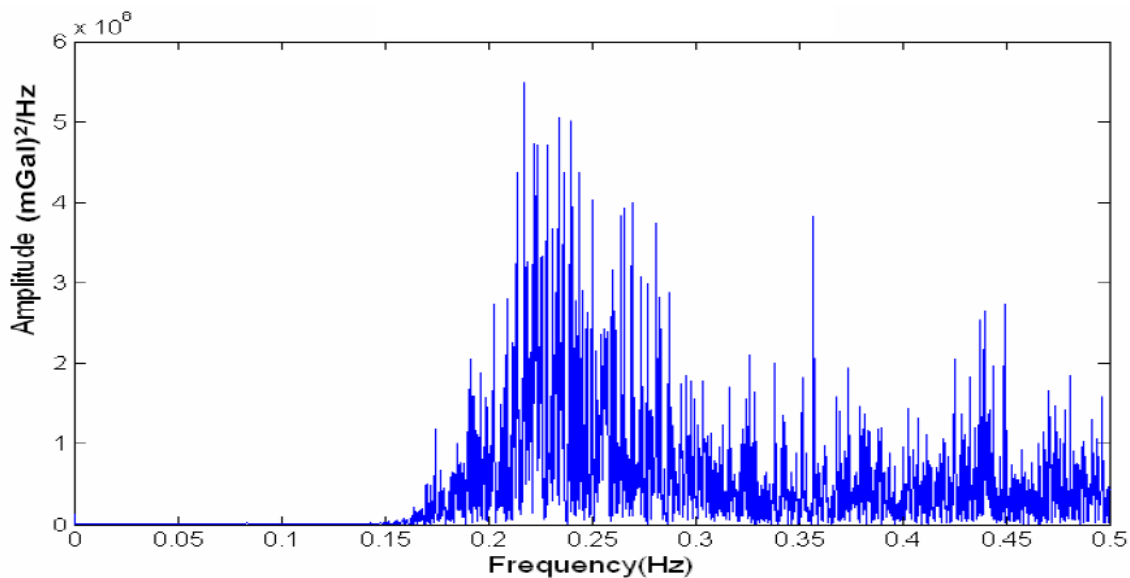


Figure 4.5: FFT spectrum shows number of undesired frequencies

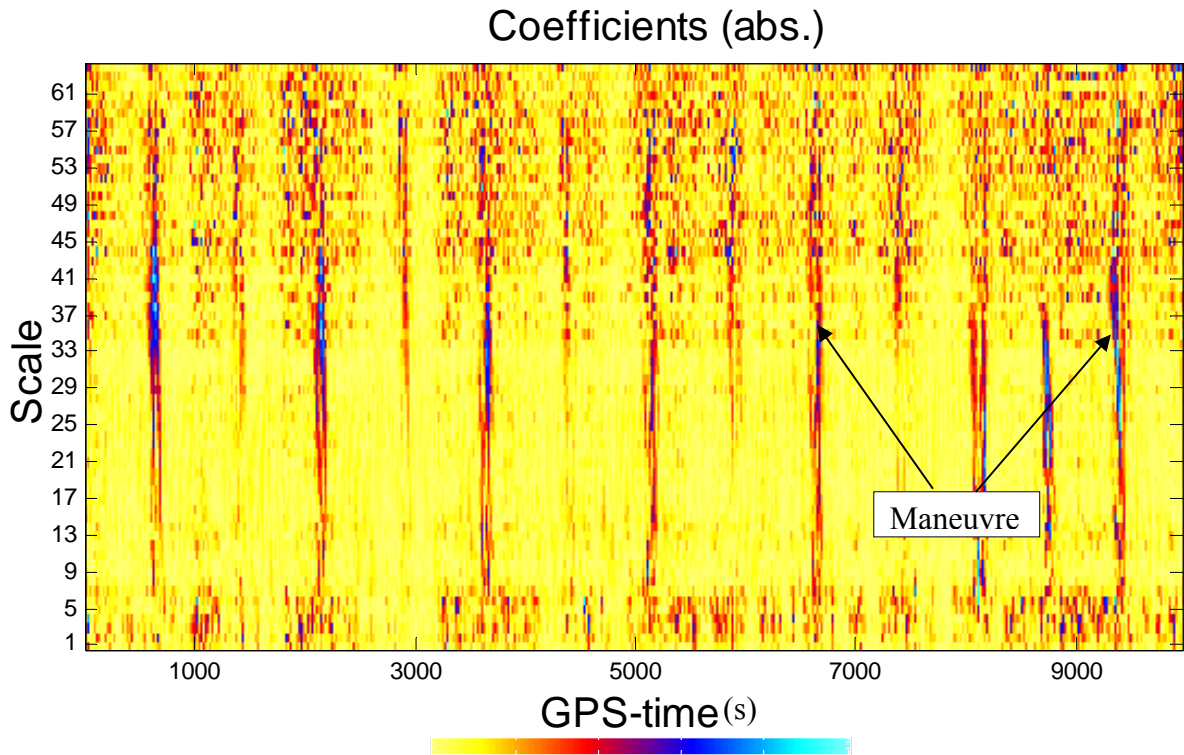


Figure 4.6: Time-frequency analysis and localization using continuous wavelet transform [after Elhabiby and Sideris, 2006b]

4.2.2 Two-dimensional analysis of Stokes's kernel and non-stationary noise

The two-dimensional wavelet transform, Equations (3.34) to (3.37), is used for the evaluation of the geodetic integrals, as will be seen in the next chapter. The wavelet transform is applied to the kernel and data. In Equation (2.7), the kernel and gravity anomalies are taken as an example of the demonstration of the localization properties of the wavelet transform in the two-dimensional domain.

The Stokes kernel at the midpoint of a $3' \times 3'$ grid is shown in Figure 4.7. The two-dimensional wavelet transform of the kernel by Daubechies wavelet with four vanishing moments (Figure 4.1), at four levels of decomposition, is shown in Figure 4.8. By comparing the two figures, it can be recognized that the same properties of the kernel (Figure 4.7), which has its peak at the centre and is dropping fast to zero in all directions,

are repeated at all the levels of decomposition: white spot at the centre (peak) and then turning dramatically to dark (dropping fast to very small values) and in all directions of decomposition at each level (Figure 4.8).

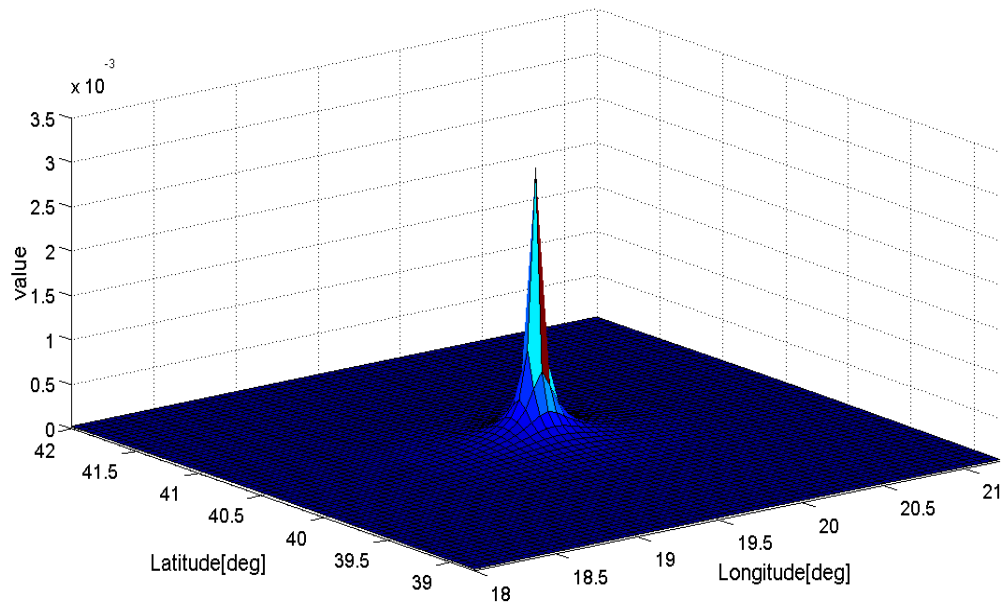


Figure 4.7: Stokes kernel in the space domain

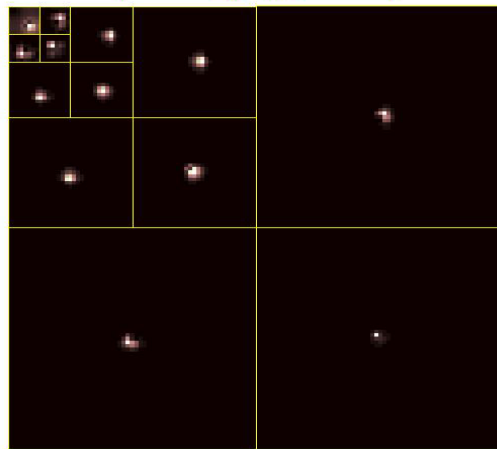


Figure 4.8: Stokes kernel in the wavelet domain (db4) at four levels of decompositions

Another example is the wavelet decomposition of geoid undulations with simulated non-stationary noise with four different noise levels. Each noise level is used for a quarter of the undulations matrix (Figure 4.9).

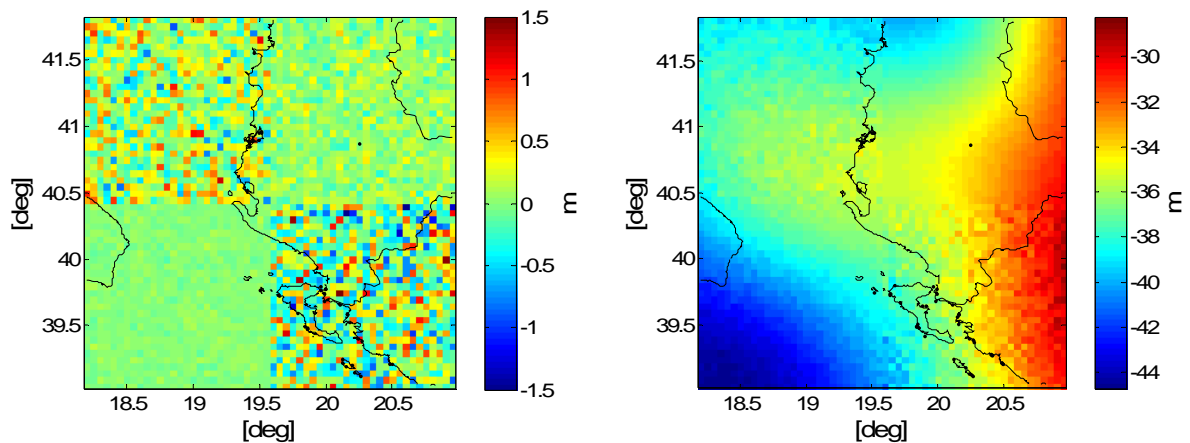


Figure 4.9: Simulated non-stationary noise (left) and geoid undulation after the addition of the noise (right)

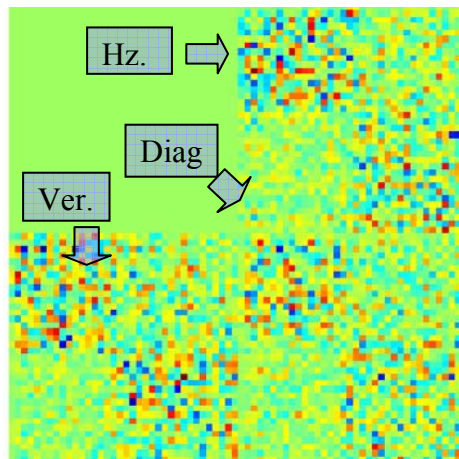


Figure 4.10: Two-dimensional wavelet decomposition of the noisy geoid undulations

Details of the data and the noise simulation and the effect of the noise on the inverse problem will be discussed in detail in Chapter Six. Wavelet localization properties are clearly seen in Figure 4.10. This figure shows one level of decomposition by db4 for the noisy geoid undulations. The pattern of the wavelet coefficients mirrors

the distribution of the non-stationary noise. In each wavelet coefficients' set (horizontal, vertical, and diagonal), the different noise levels in the four quarters of the data are reflected.

4.3 Examples of hard thresholding compression

Four direct geodetic and four inverse geodetic problems are evaluated in this thesis: the Stokes, Vening Meinesz, terrain correction, upward continuation, downward continuation, inverse Vening Meinesz, deflection-geoid formula, and inversion of the Stokes integral. Four different kernels are involved in the evaluation of these problems. These kernels are tested in this subsection for compression; the solution of the different operators will be presented in Chapters Five and Six. The four kernels to be tested are the Stokes kernel

$$\frac{1}{[(x_p - x)^2 + (y_p - y)^2]^{1/2}} \quad (4.1)$$

the deflection-geoid kernel

$$\frac{x_p - x}{[(x_p - x)^2 + (y_p - y)^2]} \quad \text{or} \quad \frac{y_p - y}{[(x_p - x)^2 + (y_p - y)^2]} \quad (4.2)$$

the terrain correction kernel

$$\frac{1}{[(x_p - x)^2 + (y_p - y)^2]^{3/2}} \quad (4.3)$$

and the Vening Meinesz kernel

$$\frac{x_p - x}{[(x_p - x)^2 + (y_p - y)^2]^{3/2}} \quad \text{or} \quad \frac{y_p - y}{[(x_p - x)^2 + (y_p - y)^2]^{3/2}} \quad (4.4)$$

The analysis for these equations shows that all the four kernels are decreasing rapidly away from the computational point (x_p, y_p) . Equation (4.1) has a denominator of distance to the power of $1/2$; this increases to 1.0 in Equation (4.2); 1.5 in Equation (4.3)

and (4.4). The higher the power, the faster the kernel drops to zero from the computation point. These properties will be tested numerically in the following section.

The testing procedure for the compression levels obtained by the hard thresholding wavelet technique, Equations (3.40) to (3.42), will be as follows:

- Testing the relation between the compression levels achieved and how fast the kernels decay to zero.
- Evaluation of the sensitivity of the automated thresholding value, estimated from Equation (3.41) or (3.42), to the grid size and spacing.

4.3.1 Global fixed thresholding for kernel compression

Different thresholding values are tested for the compression of the kernels of different operators. Twelve values between 1×10^{-12} and 1×10^{-1} are tested for all four kernels (Equations (4.1) to (4.4)). From Figure 4.11, it can be observed that the terrain correction, with the fastest dropping kernel, has the maximum compression level at all the thresholding values less than 1×10^{-4} . The compression is equal to 78% at 1×10^{-8} thresholding value. The Vening Meinesz kernel, with its slower dropping kernel, has smaller compression level percentages than the terrain correction. The compression is equal to 48% at 1×10^{-8} .

The Stokes and deflection-geoid kernels have almost identical behaviours. Although the deflection geoid denominator has a power equal to 1, which is higher than the Stokes kernel, its numerator (the distance in the y direction or x direction) reduces the rate of decrease of the kernel. Thus, the compression rate achieved by the deflection-geoid kernel is practically the same as that of the Stokes kernel; at 1×10^{-8} threshold, the compression is almost 20%. These results show the role of the rate of the kernels' decrease on the compression levels that can be achieved in the evaluation of geodetic integrals.

The thresholding values in Figure 4.11 were chosen empirically. As mentioned earlier, an automated thresholding algorithm (hard thresholding) will be implemented in the evaluation of the geodetic operators (Equations (3.41) or (3.42)). These two equations

were applied to the four kernels ($1 \text{ km} \times 1 \text{ km}$ and 65×65 grid size) and the following values were obtained:

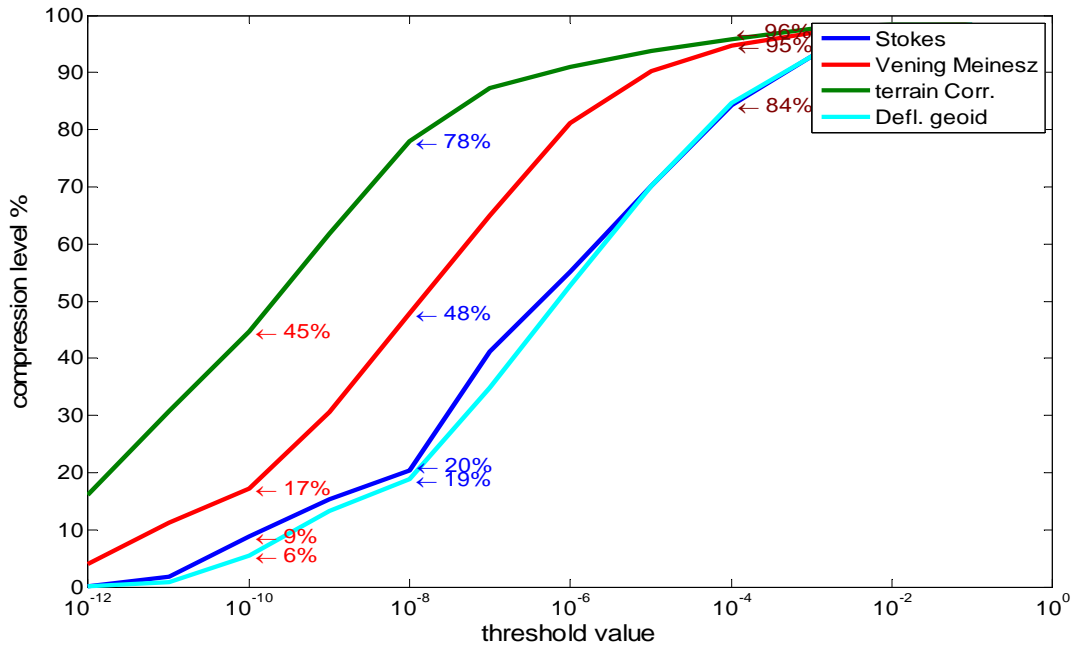


Figure 4.11: Global fixed thresholding for Stokes, deflection-geoid, terrain correction, and Vening Meinesz kernels

Table 4.1: Estimated thresholding values (automated global fixed thresholding)

Global fixed thresholding	Thresholding value	Compression level %
Stokes kernel	1×10^{-4}	84%
Deflection-geoid kernel	1×10^{-4}	84%
Vening Meinesz	1×10^{-6}	82%
Terrain correction kernel	1×10^{-8}	78%

Table 4.1 shows that Equations (3.41) or (3.42) lead to compression levels for all the kernels that are in the range of 78% to 84%. The adaptability of the thresholding technique can be seen from the change of the values according to the kernel properties, which emphasize the value of the wavelet coefficients to be thresholded. The algorithm that will be used in the evaluation of different geodetic operators will depend on the value estimated from Equations (3.41) or (3.42). This value is chosen as a reference value. Another four thresholding values higher in magnitude are tested. Each of these values

will be higher by one order of magnitude than the previous one, starting at the reference value (estimated).

Different grid spacings are tested by the same procedure for the Stokes kernel. The grid spacing varied from 1 km to 25 km for a 1000 km \times 1000 km area. Equation (3.41) or (3.42) is applied; very close thresholding values were obtained except for the first case but with different compression levels. From Table 4.2, it can be seen that the compression level decreases with the increase of the grid spacing for the same area. Also, different grids were tested (

Table 4.3) with the same spacing. The compression levels increased with the size of the grid because the wavelet coefficients that pass the threshold are almost the same at the centre while the rest are removed. For both cases, the accuracy will not be affected because the wavelet coefficients thresholded, using Equations (3.41) or (3.42), have an insignificant influence on the solution and consequently on the accuracy, as will be shown in Chapters Five and Six.

Table 4.2: Estimated thresholding values (automated global fixed thresholding) for different grid spacings

Grid spacing	Thresholding value	Compression level %
1 km	2×10^{-6}	98.7%
5 km	1×10^{-5}	94.6%
10 km	2×10^{-5}	89.2%
15 km	3×10^{-5}	84.7%
20 km	4×10^{-5}	80.4%
25 km	5×10^{-5}	74.1%

Table 4.3: Estimated thresholding values (automated global fixed thresholding) for different grid sizes

Grid Size	Thresholding value	Compression level %
50 \times 50	8×10^{-4}	80.4%
100 \times 100	2×10^{-4}	88.5%
150 \times 150	9×10^{-5}	93%
250 \times 250	3×10^{-5}	95.7%
500 \times 500	8×10^{-6}	97.7%
1000 \times 1000	2×10^{-6}	98.7%

4.3.2 Level/direction-wise thresholding

Another technique of applying wavelet thresholding is introduced here. The two-dimensional wavelet transform of the kernel and the signal divides the matrix into tiles (sub-matrices). In first level decomposition, the matrix is divided into four sub-matrices. Each sub-matrix is one quarter of the original matrix.

The global thresholding introduced in the previous subsection is applied to all three detailed decompositions (vertical, horizontal and detail parts) with the same value. The modification introduced here comes after applying the global thresholding to all three parts; extra higher thresholding values are applied to each decomposition sub-matrix individually.

As mentioned in the previous sections, there are four higher thresholding values from the reference value (estimated). The four values increase the compression level; consequently, degradation in the accuracy occurs. Some of these accuracies are acceptable and some are not. The target of level/direction-wise thresholding is to choose the best thresholding values' combination to optimize the maximum compression level with an acceptable accuracy. Different values can be introduced to the wavelet coefficients at each level of decomposition (level-wise). Also, at each level, different values can be introduced in each direction (direction-wise).

Figure 4.12 shows that the approximation part is kept without any change. The starting value is always the reference-estimated value from Equations (3.41) or (3.42). The large thresholding values are at the diagonal decomposition in the first levels. Then, different values (smaller than the diagonal) are applied in the horizontal and vertical directions. The higher the level of decomposition, the smaller the thresholding value applied. The practical testing of this approach will be introduced numerically in Chapter Five.

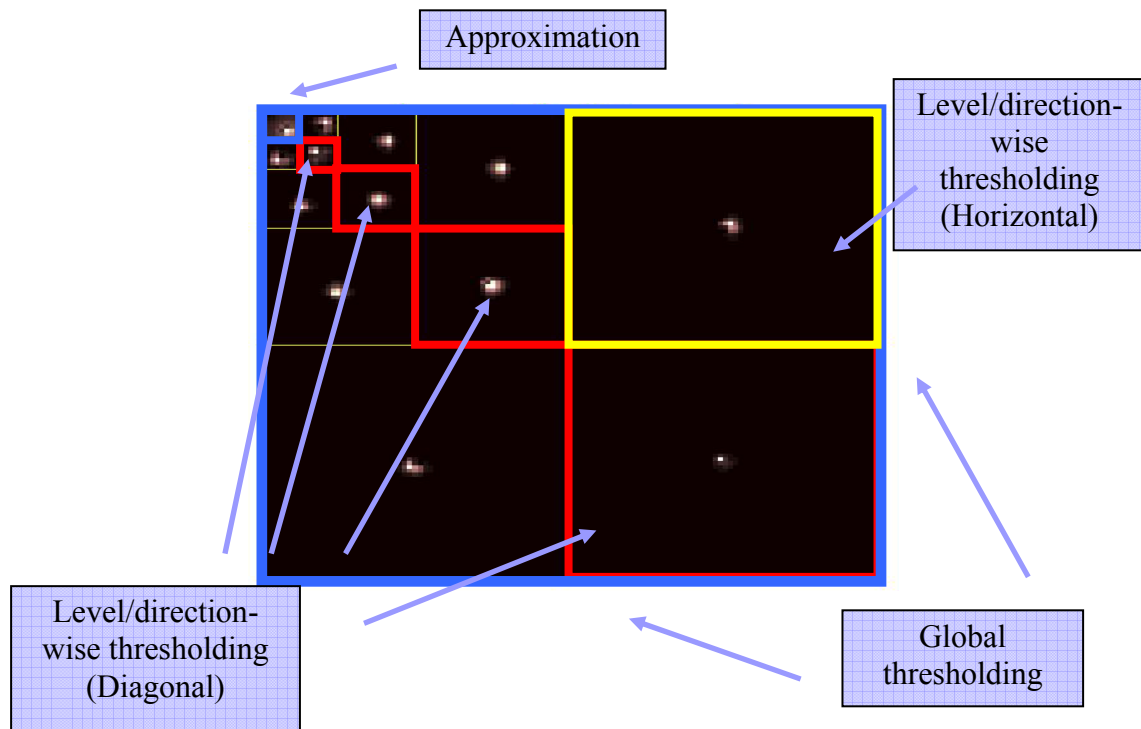


Figure 4.12: level/direction-wise thresholding [Elhabiby and Sideris, 2006a]

4.4 Examples of soft thresholding de-noising

The soft thresholding algorithm illustrated in Section 3.3.2 is applied for de-noising gravity disturbance in airborne gravimetry [Glennie, 1999] in one dimension. The algorithm is tested in two dimensions for de-noising the non-stationary simulated noise introduced in Section 4.2.2.

4.4.1 One-dimensional de-noising of airborne gravity data

The wavelets transform de-noising technique was used in the de-noising and the smoothing of the gravity disturbance, shown in Figure 4.4. The de-noising technique is compared to the outputs of the 90s and 120s low-pass filters. Figure 4.4 shows the presence of noise and outliers. The 90s and 120s low-pass filters are output from the KINGSPAD [Schwarz and El-Sheimy, 1998] and AGFILT software [Wei and Schwarz, 1998], developed by the University of Calgary. The Meyer wavelet is used. The

difference between the wavelet de-noising and the reference data is shown in Figure 4.13, with RMS value equal to 25.5 mGal [Elhabiby and Sideris, 2006b]. The difference between the 90s and 120s low-pass filters and the reference data is of RMS values equal to 26.68 and 23.71 mGal (Figure 4.14 and Figure 4.15), respectively. It can be recognized that the outliers (very high frequencies) caused by manoeuvres have been removed successfully using the wavelet de-noising algorithm, and it is better than the 90s low-pass filter and with 1.8 mGal RMS higher than the 120s.

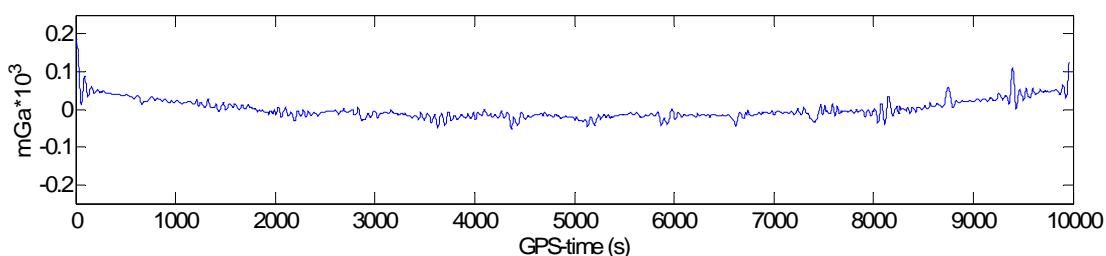


Figure 4.13: Difference between reference data and wavelet de-noising output [Elhabiby and Sideris, 2006b].

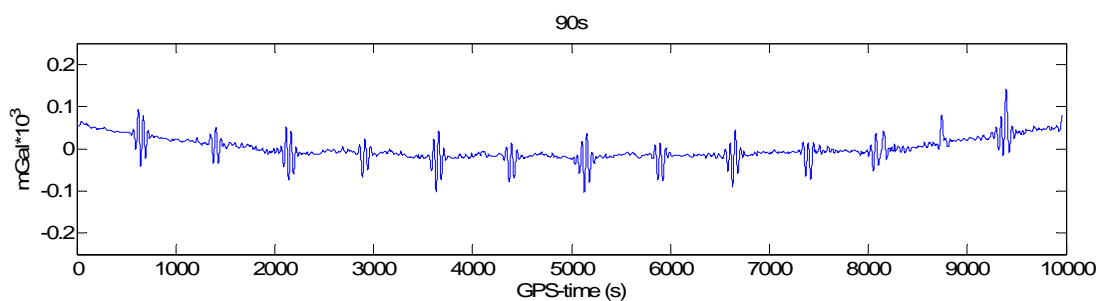


Figure 4.14: Difference between reference data and 90s low pass filter output

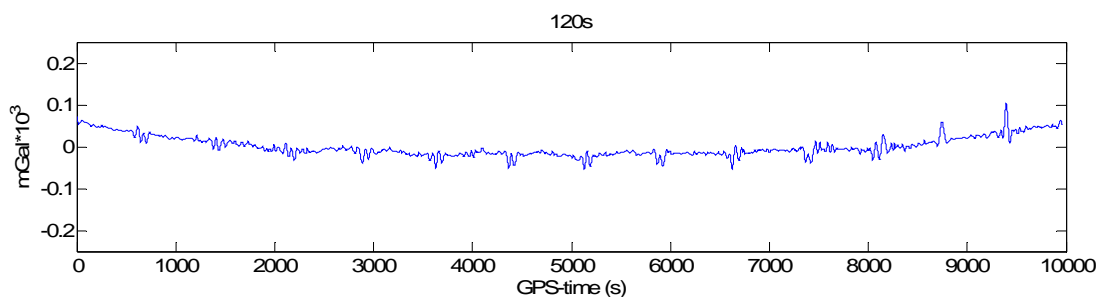


Figure 4.15: Difference between reference data and 120s low pass filter output.

4.4.2 Two-dimensional de-noising of geoid undulations

As mentioned before, all the geodetic operators evaluated in the current thesis are two-dimensional integrals. The de-noising algorithm is tested on stationary and non-stationary simulated noise in two dimensions. A grid of geoid undulations is used in the evaluation of the effectiveness of the de-noising algorithm. The simulated noise added to the geoid undulations will later be used as an input in the inversion of the Stokes integral in Chapter Six.

4.4.2.1 Stationary noise

For testing purposes, random noise is simulated and superimposed on the grid of undulations introduced in Section 4.2.2. The noise level was chosen to be $\sigma = \pm 50 \text{ cm}$. The simulated random noise is shown in Figure 4.16.

The contaminated geoid undulations are shown in Figure 4.17. The soft thresholding de-noising algorithm (Equations (3.43) and (3.44)) is applied with Daubechies wavelet with twelve vanishing moments and two levels of decomposition. The reason for the large number of vanishing moments is to smooth the signal and reduce the effect of the random noise. The de-noised geoid undulations are shown in Figure 4.18.

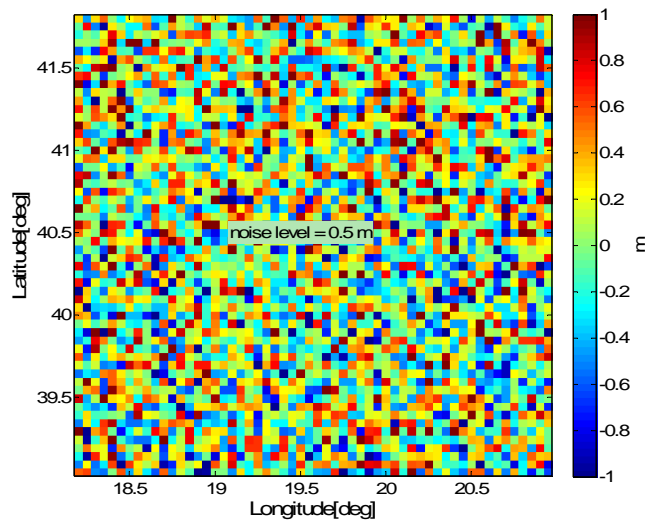


Figure 4.16: Simulated stationary random noise

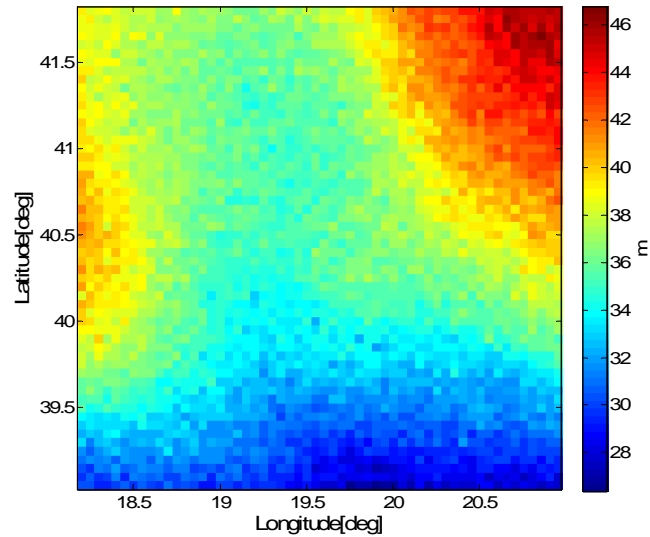


Figure 4.17: Contaminated geoid undulations by simulated stationary random noise

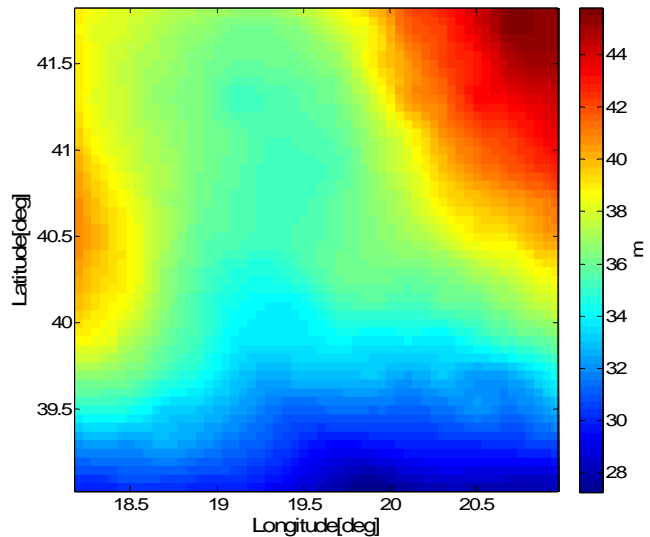


Figure 4.18: De-noised geoid undulations by soft thresholding

The difference between the recovered geoid undulations and the original clean data has a RMS value of 17 cm (Figure 4.19). The soft thresholding de-noised the simulated random noise and recovered the geoid undulations with a 66% improvement. In Chapter Six, this improvement will have a great effect on the inversion of the Stokes integral using the wavelet transform.

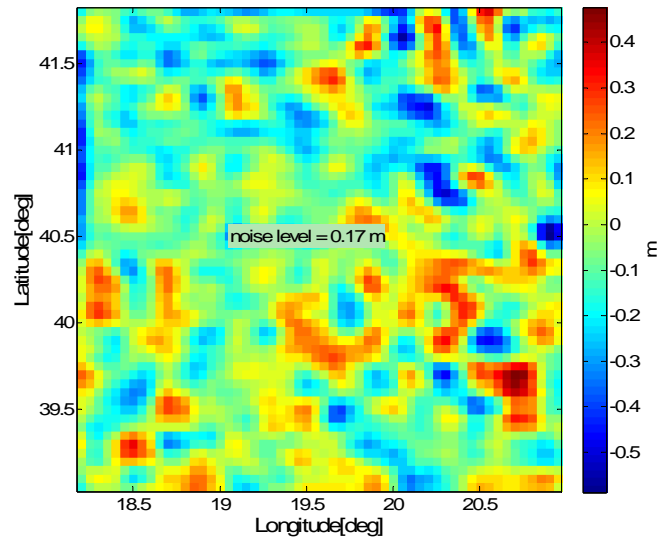


Figure 4.19: Difference between de-noised geoid undulations and original data

4.4.2.2 Non-stationary noise

The simulated non-stationary noise introduced in Section 4.2.2 and Figure 4.9 is de-noised by the soft thresholding (Equations (3.43) and (3.44)), as shown the following figure:

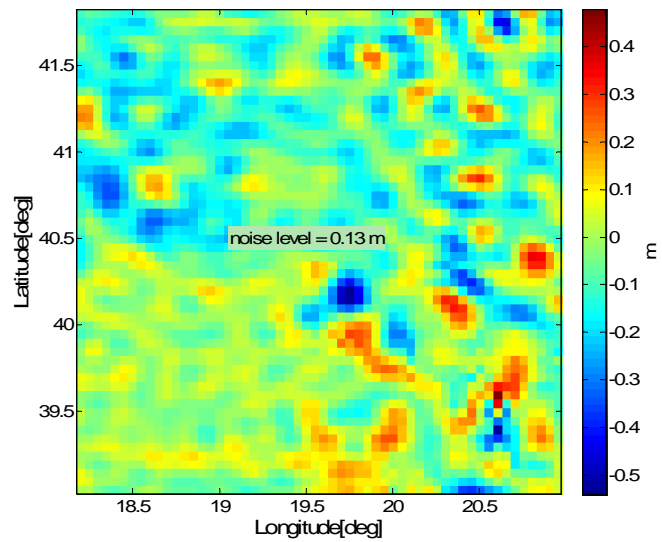


Figure 4.20: Difference between recovered geoid undulations after de-noising and the reference data

The difference between the contaminated geoid undulations and the reference data has a RMS value of 31 cm. After the de-noising, the RMS of the difference between the recovered de-noised data and clean data is reduced to 13 cm (Figure 4.20); an improvement in accuracy of almost 60%. The effect on the solution of the inversion of the Stokes integral will be discussed in detail in Chapter Six.

4.5 Summary

In this chapter, the localization properties of the wavelet transform in one and two dimensions were illustrated. The Stokes, Vening Meinesz, deflection-geoid, and terrain correction integrals kernels were also analyzed in this chapter. The rate of the kernels' decrease away from the computational point had a direct impact on the compression levels achieved at different thresholding values. Because the terrain correction kernel had the fastest dropping kernel, it achieved the highest compression level in comparison to the other kernels. On the other hand, both the Stokes and the deflection-geoid kernels with the slowest dropping kernels had the smallest compression level percentages achieved. The Vening Meinesz kernel compression levels were between the terrain correction and the Stokes percentages. An automated soft thresholding wavelet algorithm was introduced. The algorithm was tested in two dimensions with simulated stationary and non-stationary noise. The algorithm improved the data in both cases by almost 60%.

The main outcomes of this chapter can be connected to a number of practical applications as follows:

- Wavelet thresholding technique is very effective in the evaluation of different geodetic operators because of the geodetic operators' fast decaying kernel. This can help in real-time applications.
- The kernel can be pre-processed and compressed efficiently using the new wavelet technique. This compression, in addition to the new wavelet implementation that requires the use of the data set only once, will decrease the space required for the kernel and data storage.

- An example of these of applications is the terrain correction in case of airborne gravimetry applications.
- Also, the new wavelet compression implementation can effectively help in decreasing the amount of the space required for the backup of all the operations (data and kernels) used in different projects (e.g., Satellite altimetry, regional geoid modelling, and airborne gravimetry) because the solution can be efficiently recovered from only 90% of the size of the original kernels' matrices with an acceptable practical accuracy.
- The wavelet de-noising technique is efficient in de-noising non-stationary noise, which can be applied for the de-noising and the analysis of airborne gravimetry and satellite altimetry measurements, which have highly non-stationary properties.

Chapter Five: Wavelet evaluation of direct geodetic integrals

For many years, the classical approach used for the efficient evaluation of geodetic integrals has been based on the fast Fourier Transform (FFT) [Sideris and Tziavos, 1988]. A wavelet approach is used in this chapter, however, as an alternative to the FFT in order to evaluate the different geodetic integrals. The wavelet transform is a very powerful tool for evaluating geodetic integrals with singular and fast dropping kernels because of its localization power in the space and frequency domain [Gilbert and Keller, 2000]. Kernels with singularity decay from the singular point rapidly and smoothly [Vanicek and Christou, 1994]. All the geodetic integrals tested in this chapter have such kernels; thus, the wavelet transform of such kernels leads to a significant number of small value coefficients, as shown in Section 4.3. Therefore, high compression levels of the kernels can be achieved.

In this chapter, four geodetic problems will be evaluated using the new wavelet transform approach (Section 3.5): Stokes, Vening Meinesz, terrain correction, and the upward continuation integral. Their wavelet solutions will be compared to the FFT and the numerical integration approaches. This methodology of investigation will follow the flowchart shown in Figure 3.12. The advantages and disadvantages of the different wavelet approaches will also be examined.

5.1 Evaluation of the Stokes integral

The Stokes integral is evaluated using three different methods. First, the integral is evaluated using FFT and numerical integration. Then, the integral is evaluated using three wavelet algorithms shown in Figure 3.12: wavelet full matrix solution, wavelet global fixed thresholding, and wavelet level/direction-wise thresholding [Elhabiby and Sideris, 2006a].

5.1.1 Data and wavelet used

The data used in the evaluation of the Stokes integral are synthetic gravity anomalies and geoid heights over Greece [Novak et al., 2001]. These are on a 3' by 3' grid in the area (18°E-21.2°E, 38.8°N-42°N), as shown in Figure 5.1.

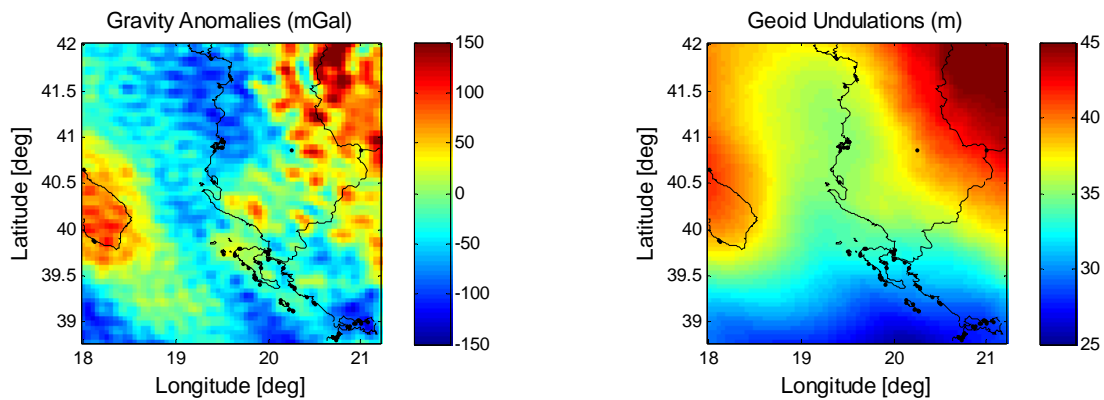


Figure 5.1: Synthetic gravity anomalies and geoid undulations over Greece and Italy

The Daubechies family of wavelet is chosen because of their orthogonality and compact support properties. Daubechies wavelets of order four are used; four vanishing moments (db4) lead to a significant number of coefficients with small values. Different Daubechies (db) wavelets with different vanishing moments were tested. However, with more than four vanishing moments, the signal started to be over smoothed.

5.1.2 Wavelet full matrix solution

The algorithm mentioned in Section 3.5 is used for the evaluation of the Stokes integral. The following steps are taken:

- First, the two-dimensional wavelet transform is applied to the gravity anomalies (Figure 5.2) after removing the long wavelengths using the EGM96 geopotential model (degree 360). The signal is decomposed into four levels of decomposition, then it is transformed to a column vector and the coefficients are arranged as shown in Figure 3.11.

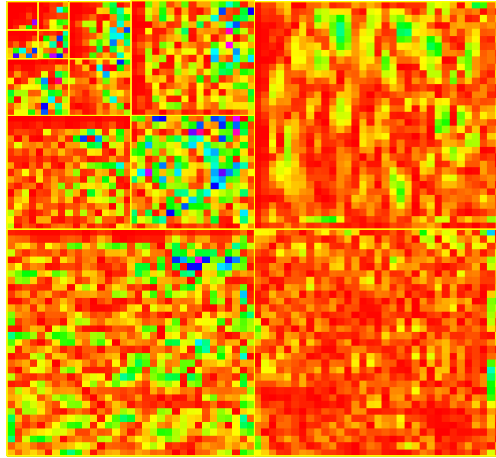


Figure 5.2: The two-dimensional wavelet transform of the gravity anomalies using db4 with four levels of decomposition

- Second, the two-dimensional wavelet transform with four levels of decomposition is applied to the kernels corresponding to all the computational points. An example of these kernels is the one corresponding to the midpoint of the grid; its corresponding two-dimensional wavelet transform is shown in Figure 5.3.

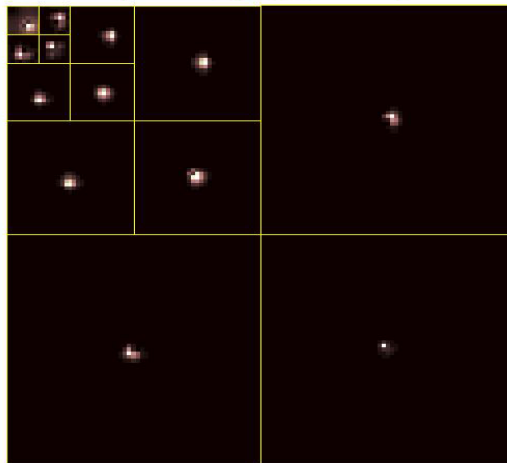


Figure 5.3: The two-dimensional wavelet transform of the centre point Stokes kernel of the gridded data using db4 with four levels of decomposition

- Third, the A design matrix is built using the wavelet coefficients corresponding to the geodetic integral kernels (Figure 3.10); each line corresponds to one kernel, as shown in Figure 5.4.

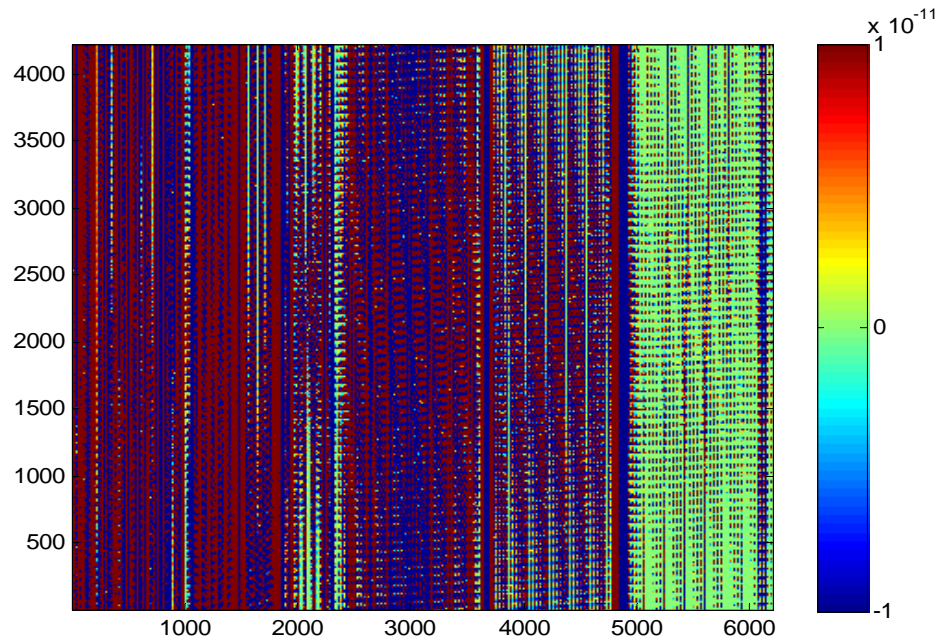


Figure 5.4: Stokes kernels' A design matrix (unitless)

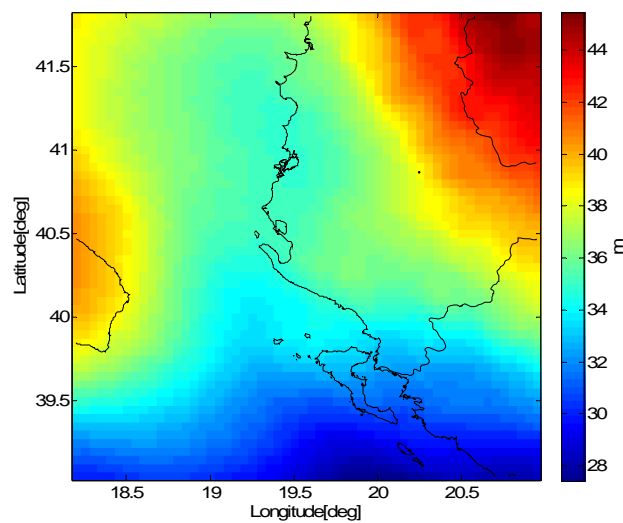


Figure 5.5: Wavelet full matrix solution for the Stokes integral

- Fourth, the solution is achieved by multiplying the A matrix with a_j vector (Equation (3.61)). The solution is illustrated in Figure 5.5.

The zero-padded FFT and the numerical integration solutions of the Stokes problem are identical [Sideris and Li, 1993]. The difference between both solutions and the reference data has RMS accuracy of 20 cm (Figure 5.6). The RMSE of the difference between the wavelet full matrix solution and FFT solution is less than 1 cm, which means that the wavelet full matrix, FFT, and the numerical integration are almost identical, as shown in Figure 5.6 and Figure 5.7. In the sequel, the different wavelet solutions are compared only to the numerical integration solution.

Figure 5.4 shows the Stokes kernels' wavelet transform coefficients (A design matrix). It is clear that the A matrix is a dense full matrix, with no zero elements. This leads to the main drawback of this algorithm; that is, the allocation of the large design matrix in memory, which is significant compared with the FFT approach. The memory required for this matrix is 186 MB, which is huge compared to the FFT approach, for solving the same area with zero padding (130×130 elements).

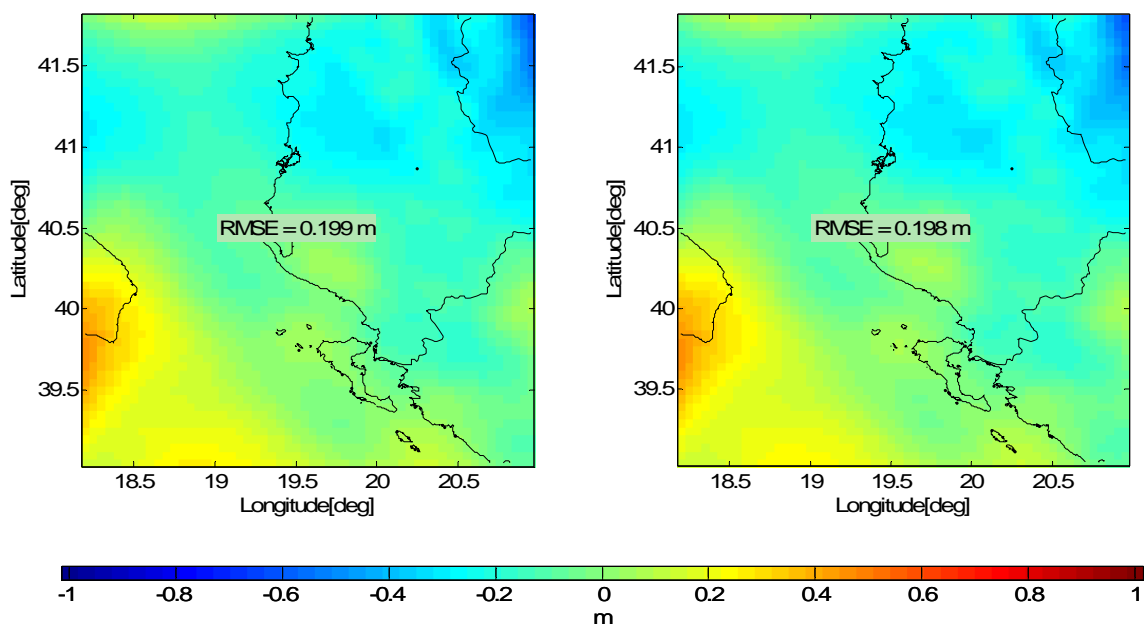


Figure 5.6: FFT and wavelet full matrix solutions in comparison to reference data for the Stokes integral

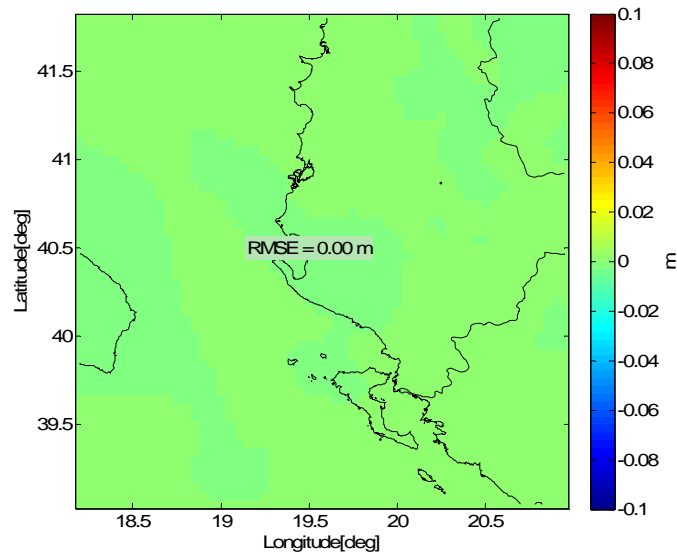


Figure 5.7: Difference between wavelet full matrix solution and the numerical integration solution for the Stokes integral

However, a significant number of elements are of very small values. This is mainly because of the fast decay of the kernel towards zero and the four vanishing moments of db4 (Section 4.3). If an efficient thresholding technique is applied, this will lead to a sparse matrix, as shown in the next sections.

5.1.3 Wavelet global fixed thresholding solution

First, the hard thresholding algorithm (Equations (3.41) and (3.42)) is used. For the Stokes integral with a 3' by 3' gridded kernel, the estimated threshold value is 1.5×10^{-7} . When applying this threshold value to the A design matrix, the matrix will be sparse as shown in Figure 5.8. The number of non-zero elements is dropped from 26,190,775 elements to 6,506,135 elements, with a compression level equal to 75% (Table 5.1), and with no loss of accuracy compared to the numerical integration solution (Figure 5.9).

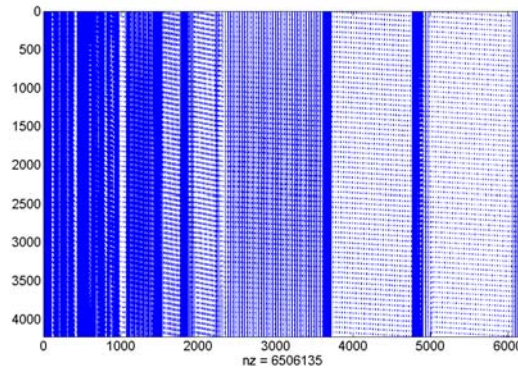


Figure 5.8: Design matrix A with 1.5×10^{-7} global thresholding value; each blue spot represents a nonzero value in the Stokes kernel.

Starting from the thresholding value obtained from Equation (3.41) or (3.42), four other larger values were tested for the Stokes kernel wavelet coefficients' compression. From Table 5.1 and Figure 5.10, it can be seen how the A design matrices corresponding to each of the thresholding values became sparse. By increasing the thresholding values to 1.5×10^{-6} , 1.5×10^{-5} , 1.5×10^{-4} , and 1.5×10^{-3} , the A matrix becomes more sparse with 83%, 93.5%, 97.6%, and 98.3% compression levels, respectively. Consequently, the storage requirement is reduced drastically. The sparse matrices are allocated in the memory by squeezing out all the zero elements and allocating only the non-zero elements with their indices.

Table 5.1: Wavelet global thresholding versus wavelet full matrix solution for the Stokes integral

Hard thresholding	Full matrix	Global Eq. (3.41) or (3.42)	(a)	(b)	(c)	(d)
Thresholding value	-	1.5×10^{-7}	1.5×10^{-6}	1.5×10^{-5}	1.5×10^{-4}	1.5×10^{-3}
Storage (MB)	186	50	36	16	8	6
RMSE (m)	-	0.0005	0.0005	0.0061	0.0604	0.3229
No. of elements	26190775	6506135	4460519	1696296	629575	445852
Comp%	0%	75%	83%	93.5%	97.6%	98.3%

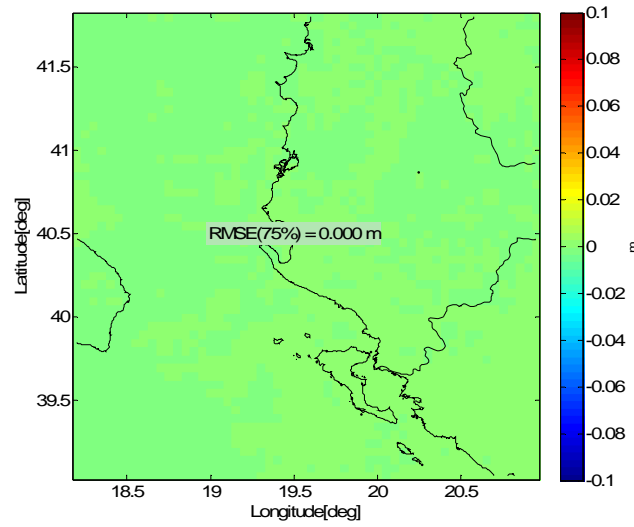


Figure 5.9: Difference between the wavelet global thresholding (1.5×10^{-7}) solution and the numerical integration solution for the Stokes integral

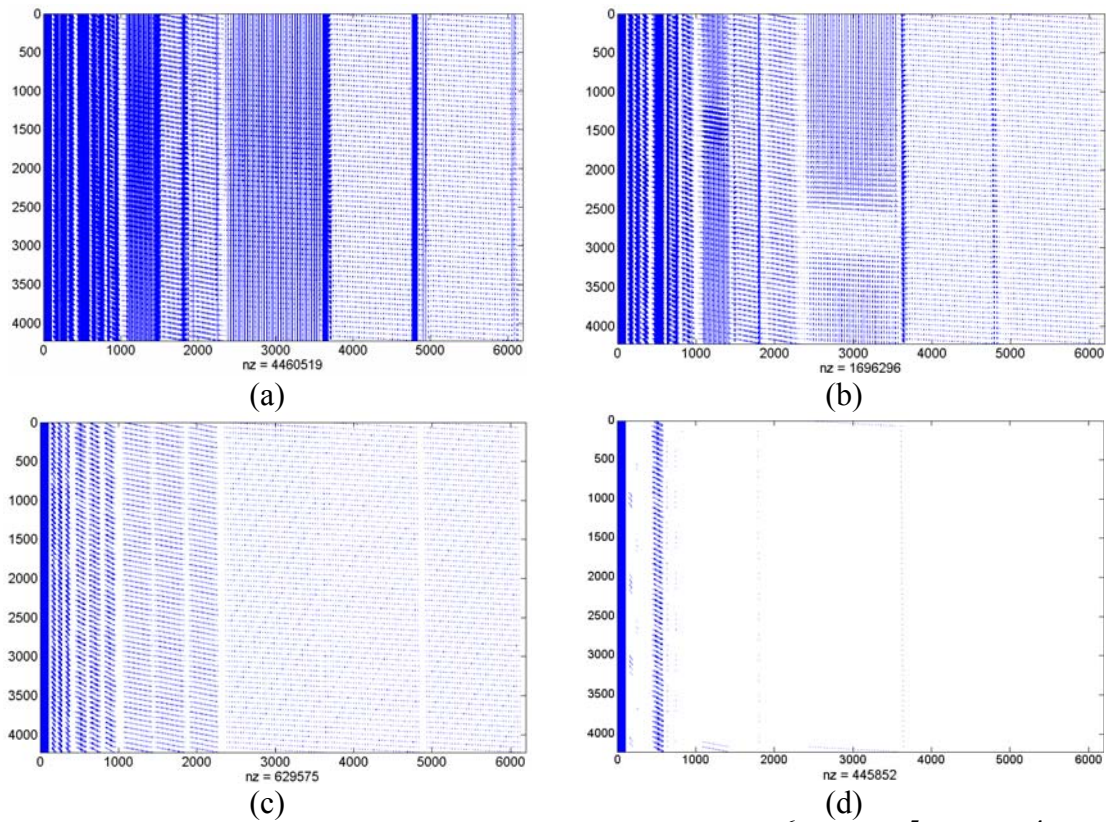


Figure 5.10: A matrix at four thresholding values (1.5×10^{-6} , 1.5×10^{-5} , 1.5×10^{-4} , and 1.5×10^{-3}); each blue spot represents a nonzero value in the Stokes kernel.

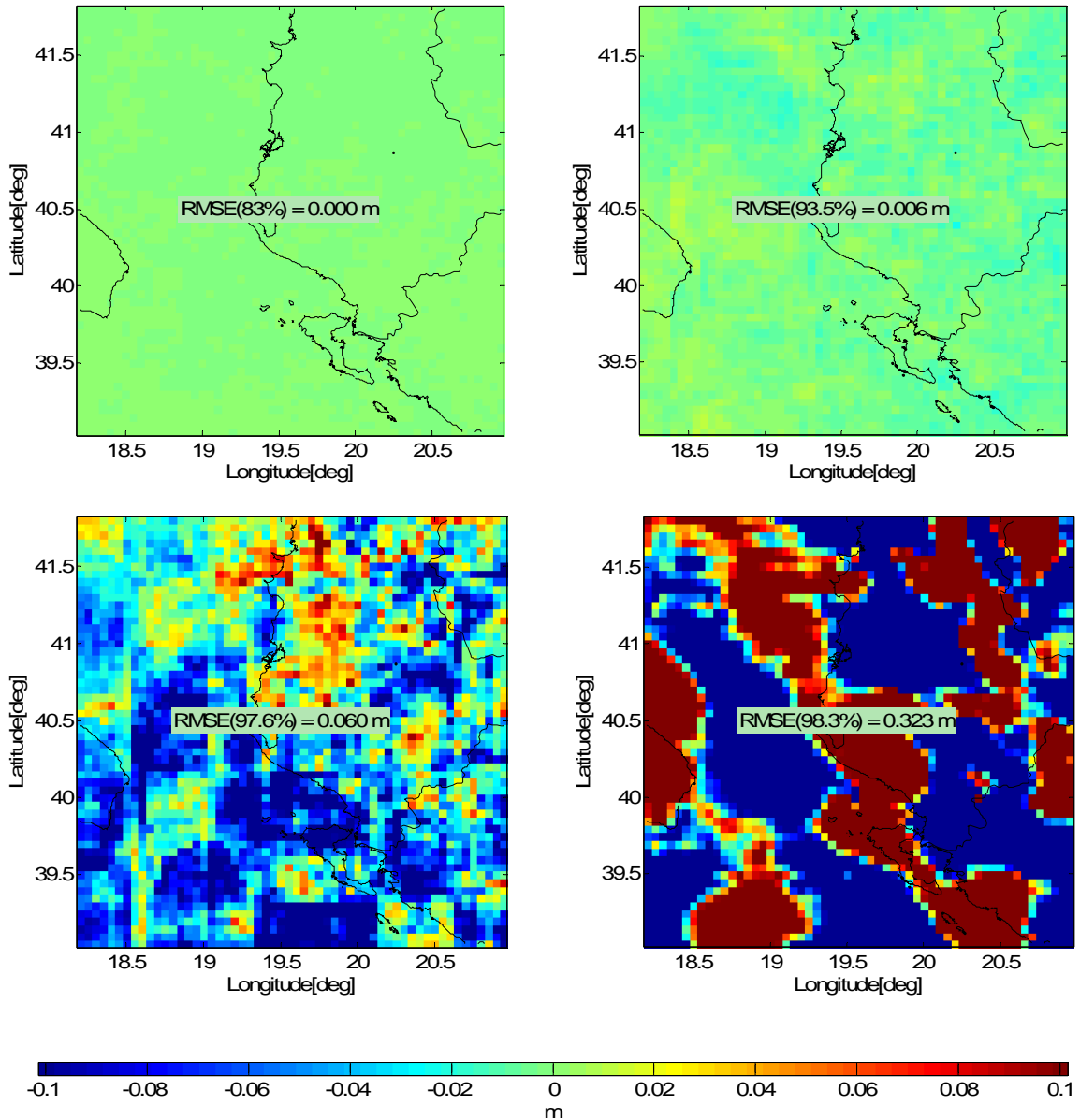


Figure 5.11 : Wavelet global fixed thresholding solution in comparison to the numerical integration solution for the Stokes integral

It can be seen in Table 5.1 that up to a 93.5% compression level, the error is less than 1 cm compared to the numerical integration solution. Although in the last two cases with thresholding values of 1.5×10^{-4} and 1.5×10^{-3} higher compression levels are achieved, there is a large degradation in the accuracy to 6 cm and 32 cm, respectively. The accuracy of the last two cases is not practically acceptable. Consequently, it can be

recognized that for this spacing using the global fixed thresholding, the maximum compression level to be achieved with the targeted accuracy required (1 cm) is 94%; see also Figure 5.11. This illustrates that the memory allocation problem can be overcome even on a personal computer. The computation CPU time required for obtaining the solution is almost the same for the four global thresholding cases—that is, less than one second.

5.1.4 Level/direction-wise thresholding solution

In this subsection, the level/direction-wise thresholding approach is introduced to increase the compression level while maintaining the required practical accuracy (Section 4.3.2). Different combinations of the four thresholding values, introduced in Table 5.1, are used in this approach. These values depend on the degree of compression required and its relevant accuracy. The combinations in Tables 5.2 and

Table 5.3 are examples of the choice of these values. The level/direction-wise approach is compared to the application of a single thresholding value.

The level/direction-wise approach can be used in two different ways. The first one is used at very high compression levels like cases (c) and (d) in Table 5.1. For case (c), instead of using a single thresholding value, a set of different thresholding values is used at the different levels and directions, as shown in Table 5.2. The use of this combination of thresholding values improves the accuracy from 6 cm (Table 5.1) to 1.3 cm (Table 5.2). This is a 77% improvement in the accuracy with only a 2.4% loss in the compression level. The same approach is repeated for the global thresholding case (d) (Table 5.1). Although the result is not as good as the targeted accuracy of 1 cm, this example is important for checking this algorithm's efficiency. The thresholding values, shown in Table 5.3, dropped the compression level from 98.3% to 96.2% but with a 90% improvement in accuracy (from 32 cm to 3 cm).

The second one is applied to the global cases (a) and (b); in this case, higher thresholding values are introduced to increase the compression percentage while

maintaining the accuracy in the acceptable range. From Figure 5.12, it can be seen that cases (a) and (b) reached higher compression levels (case (a) from 83% to 92.8% and case (b) from 93.5% to 94.8%), with no significant loss of accuracy. This finding illustrates that the level/direction-wise can be used efficiently for both cases. It is worth mentioning that the intersection of the two lines (Figure 5.12), the line for the global thresholding and the line for the level/direction-wise thresholding, is approximately equal to the optimum compression level for the required targeted accuracy.

Table 5.2: Level/direction-wise for case (c) global thresholding

Level/direction-wise	Horizontal	Diagonal	Vertical
Level 1	5.7×10^{-5}	5.7×10^{-3}	5.7×10^{-4}
Level 2	5.7×10^{-5}	5.7×10^{-4}	5.7×10^{-5}
Level 3	5.7×10^{-5}	5.7×10^{-5}	5.7×10^{-5}
Level 4	5.7×10^{-5}	5.7×10^{-5}	5.7×10^{-5}
RMSE(m)	0.013		
Comp. %	95.2%		
Storage (MB)	9.4		

Table 5.3: Level/direction-wise for case (d) global thresholding

Level/direction-wise	Horizontal	Diagonal	Vertical
Level 1	5.7×10^{-4}	5.7×10^{-3}	5.7×10^{-4}
Level 2	5.7×10^{-4}	5.7×10^{-3}	5.7×10^{-5}
Level 3	5.7×10^{-5}	5.7×10^{-4}	5.7×10^{-5}
Level 4	5.7×10^{-5}	5.7×10^{-4}	5.7×10^{-5}
RMSE(m)	0.03		
Comp. %	96.2%		
Storage (MB)	7		

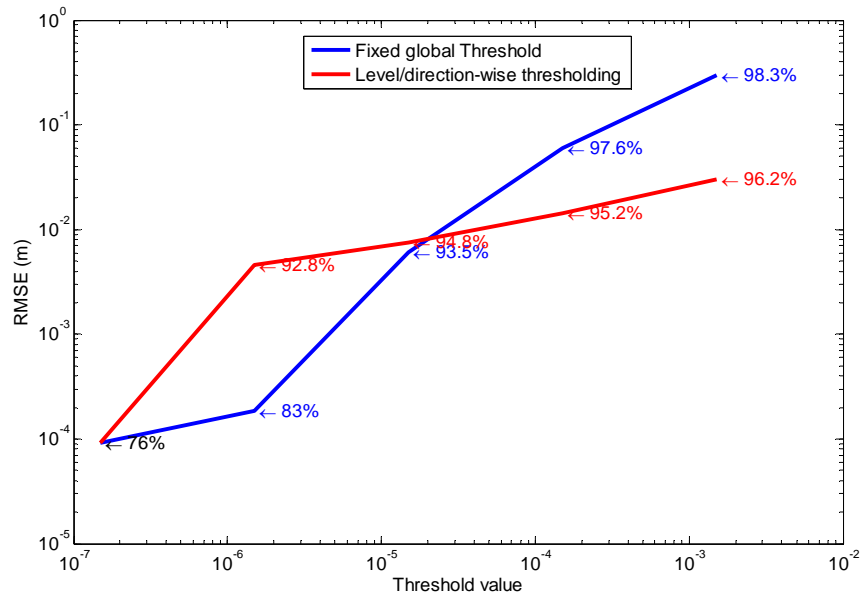


Figure 5.12: Global fixed thresholding versus level/direction-wise thresholding for the Stokes integral

5.2 Evaluation of the Vening Meinesz integral

The Vening Meinesz integral is evaluated by the methodology introduced in Section 3.6 using the wavelet full matrix solution, wavelet global thresholding, and level/direction-wise thresholding.

5.2.1 Data and wavelet used

The gravity anomaly data on a 3' by 3' grid, introduced in Subsection 5.1.1, is used in the evaluation of the Vening Meinesz integral. Figure 5.13 shows the reference data for the two components of the deflection of the vertical (horizontal and vertical components). The Daubechies wavelet with four vanishing moments is used in the evaluation of the Vening Meinesz integral.

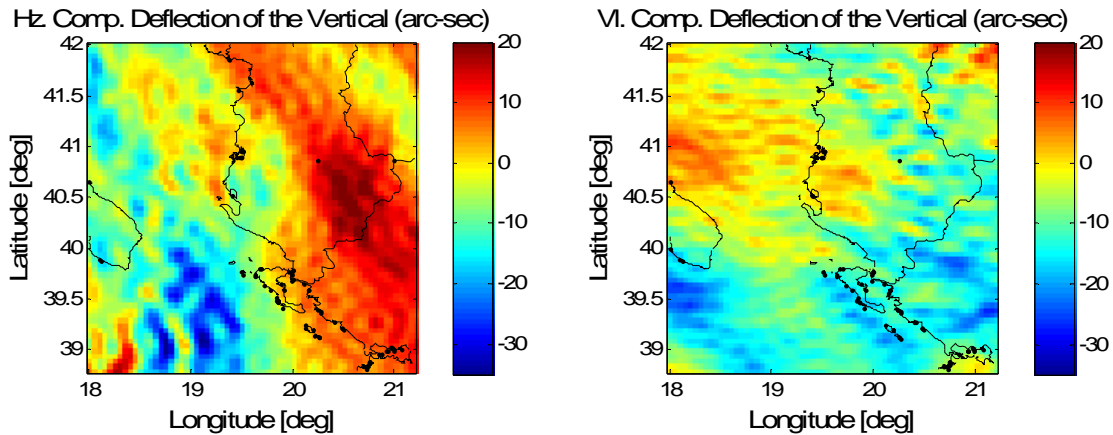


Figure 5.13: Synthetic horizontal and vertical components of the deflection of the vertical over Greece and Italy

5.2.2 Wavelet full matrix solution

The two Vening Meinesz integrals (Equations (2.11) and (2.12)) are evaluated using the wavelet full matrix algorithm, FFT, and numerical integration. The wavelet approach introduced in Subsection 5.1.2 is applied in this evaluation. The A design matrix is shown in Figure 5.14. In comparison to Figure 5.4, it can be seen that the differences between the values of both kernels (A design matrices) are significant. The values in the case of the Vening Meinesz A matrix are significantly less than in the case of the Stokes kernel; this difference is because the kernel is dropping faster towards zero in the case of the Vening Meinesz kernel than in the case of the Stokes kernel (Section 4.3).

The difference between the wavelet full matrix solution and reference data is illustrated in Figure 5.15. It is clear that the gravity anomalies are more self consistent with the horizontal component of the deflection of the vertical (RMSE=2.2") than in the case of the vertical component (RMSE=17"). This means that an improvement to the vertical component simulation is required, but this is out of the scope of this thesis. The wavelet full matrix and the numerical integration solutions of the vertical and horizontal components of the deflection of the vertical are almost numerically identical, as shown in Figure 5.16.

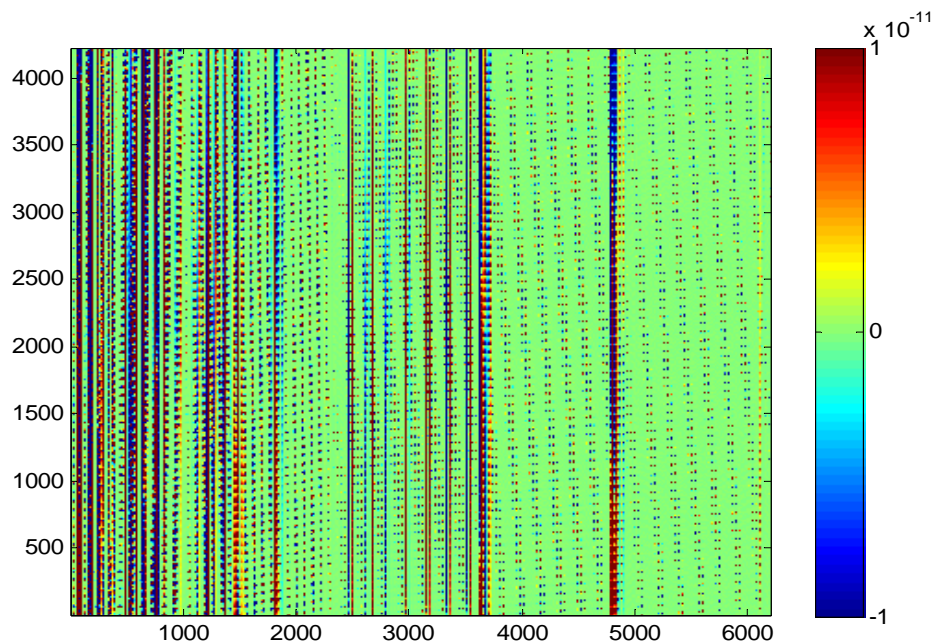


Figure 5.14: Vening Meinesz kernels' A design matrix (unitless)

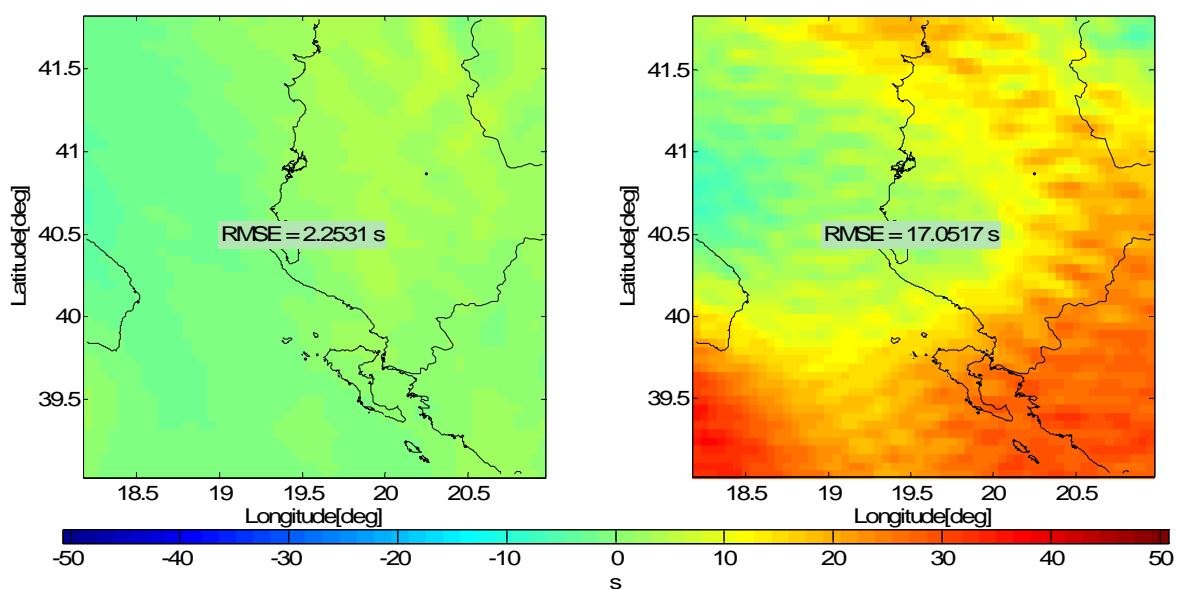


Figure 5.15: Difference of horizontal component (left) and vertical component (right) wavelet full matrix solution from the reference data

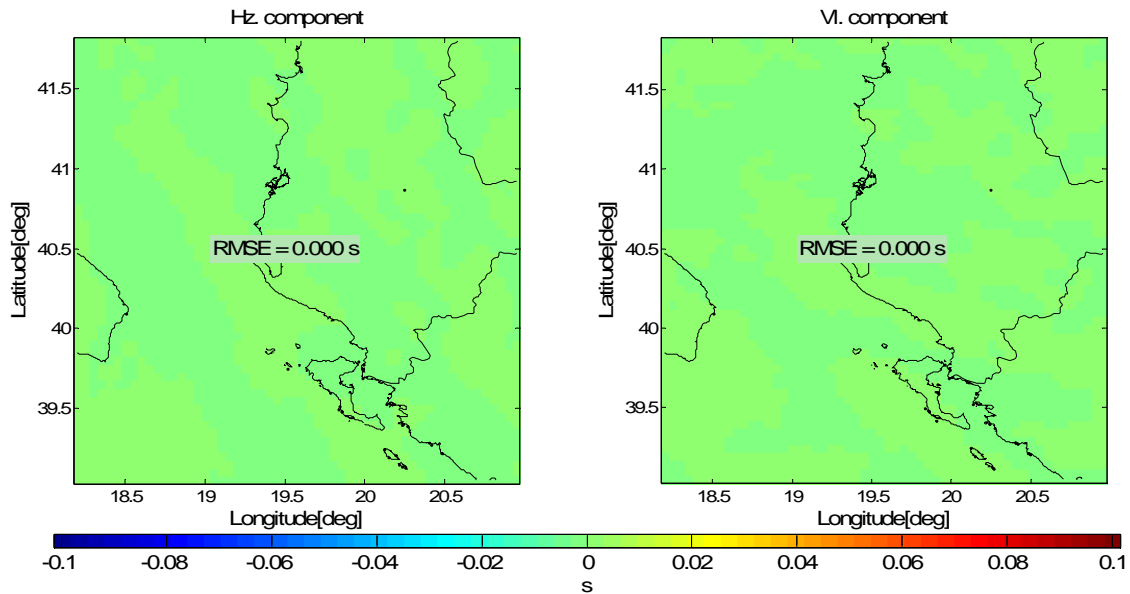


Figure 5.16: Difference between wavelet full matrix solution and numerical integration solution for horizontal and vertical component of the deflection of the vertical

5.2.3 Wavelet global fixed thresholding solution

For the Vening Meinesz integral, the threshold value estimated from Equations (3.41) or (3.42) is 7.2×10^{-13} . The solution using this global thresholding value is shown in Figure 5.17. It is clear that with a 76% compression level, there is almost no loss of accuracy and the results are numerically identical to the numerical integration approach.

From Figure 5.18 and Table 5.4, it can be seen that the design matrix A became sparser with the increase of the thresholding value (7.2×10^{-12} , 7.2×10^{-11} , 7.2×10^{-10} , and 7.2×10^{-9}). From Table 5.4 and Figure 5.19, a compression level of 95.5% is achieved with an RMSE of 0.07 arc-second, which is an outstanding practical accuracy. For the last thresholding value, a higher compression level is achieved but with a huge degradation in the accuracy, almost half arc-second RMSE, which is still quite acceptable for many applications. The case of the horizontal component of the deflection of the vertical is identical to the case of the vertical component introduced here.

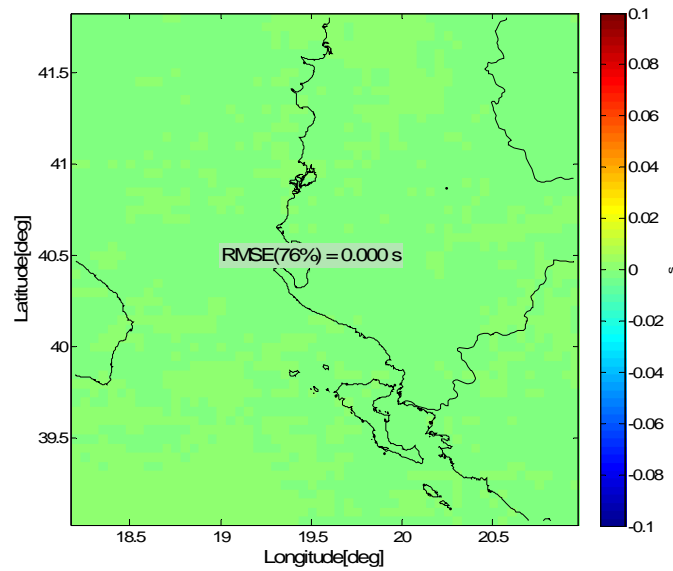


Figure 5.17: The difference between the global thresholding solution and numerical integration solution for the vertical component of the Vening Meinesz integral

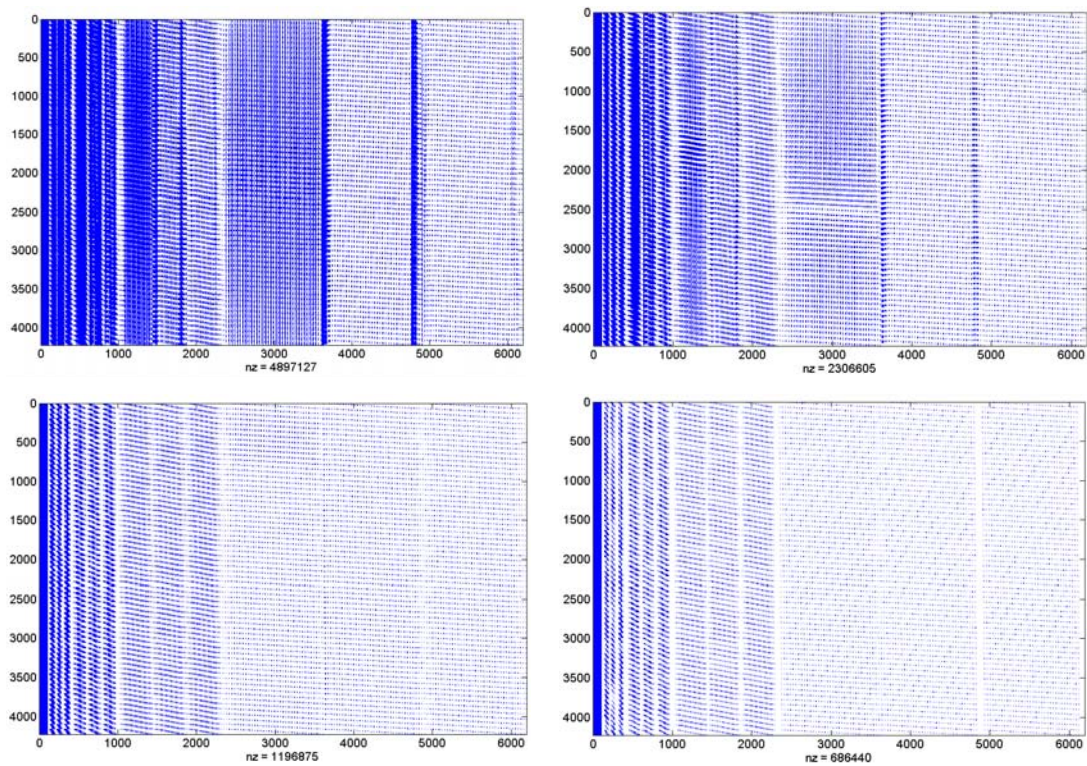


Figure 5.18: A matrix at four thresholding values (7.2×10^{-12} , 7.2×10^{-11} , 7.2×10^{-10} , and 7.2×10^{-9}); each blue spot represents a nonzero value in the Vening Meinesz kernel.

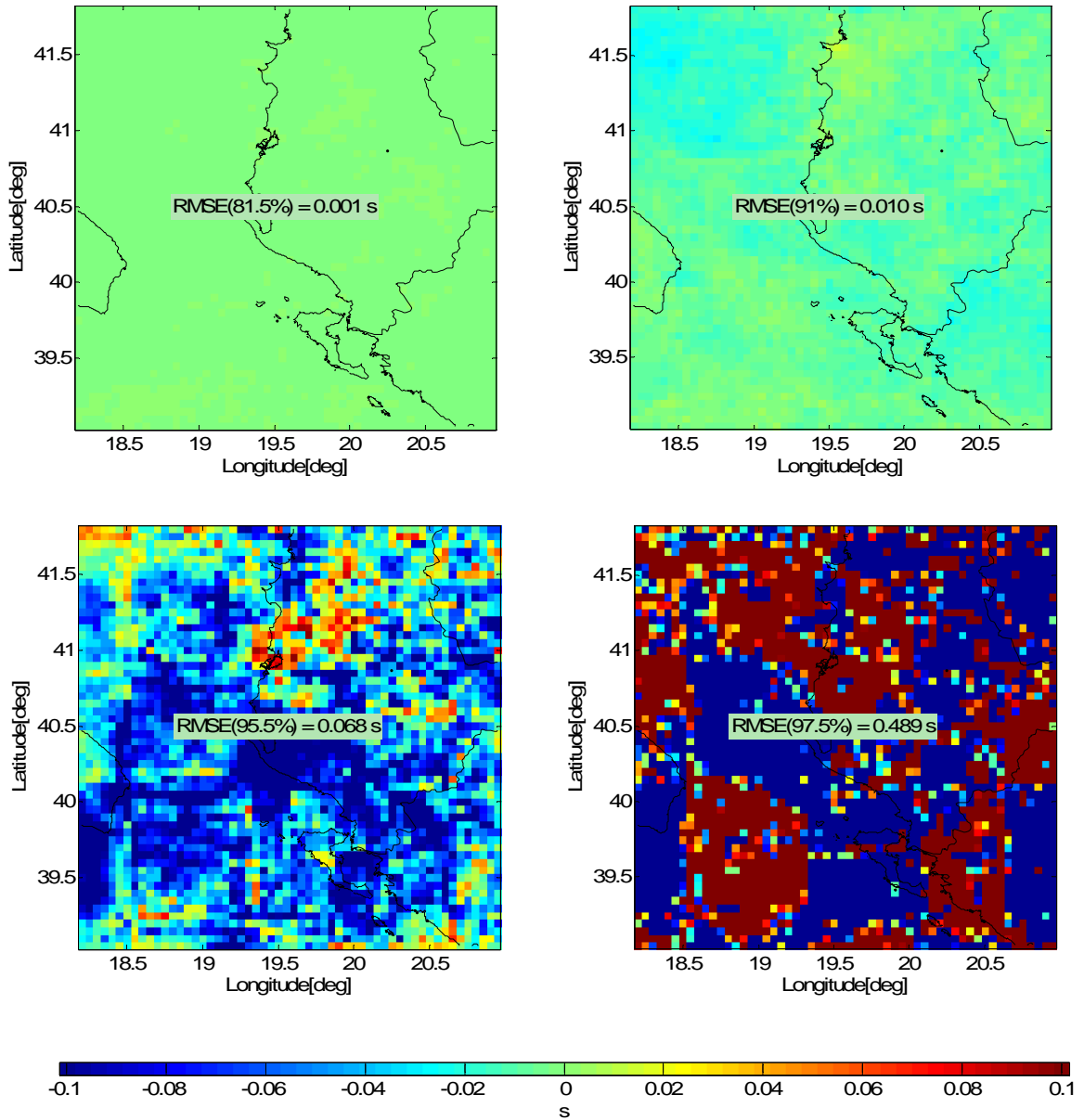


Figure 5.19: Wavelet global fixed thresholding solution for the vertical component of the deflection of the vertical in comparison to the numerical integration solution

Table 5.4: Wavelet global fixed thresholding versus wavelet full matrix solution for the vertical component of the deflection of the vertical

Hard thresholding	Full matrix	Global Eq. (3.41) or (3.42)	(a)	(b)	(c)	(d)
Thresholding value	-	7.2×10^{-13}	7.2×10^{-12}	7.2×10^{-11}	7.2×10^{-10}	7.2×10^{-9}
Storage (MB)	186	46	40	21	12	8
RMSE (arc-second)	-	0.000	0.001	0.01	0.07	0.48
No. of elements	26190775	6270318	4897127	2306605	1196875	686440
Comp%	0%	76%	81.5%	91%	95.5%	97.5%

5.2.4 Level/direction-wise thresholding solution

The four cases, (a), (b), (c), and (d), which are shown in Table 5.4, are modified using a combination of different thresholding values in each direction and at each level. The main aim behind the level/direction-wise algorithm is to reach the maximum compression level with less than a 0.5 arc-second RMSE. For the first three cases (a), (b), and (c), combinations of different thresholding values are applied, as shown in Table 5.5, Table 5.6, and Table 5.7. The compression level of global thresholding case (a) is improved from 81.5% to 92.2% with an insignificant (0.005 arc-second RMSE) loss in accuracy (Table 5.5). The global thresholding case (b) compression level is improved from 91% to 95.5% with an RMSE equal to 0.03 arc-second (Table 5.6).

In the case of the global thresholding case (d), level/direction-wise thresholding is used to improve the accuracy while maintaining the same high compression level. A small improvement in the accuracy is achieved: the RMSE is decreased from 0.49 to 0.38 arc-second (Table 5.8). The compression level is also slightly decreased from 97.5% to 97.1%. Consequently, there is a 23% gain in the accuracy with a 0.4% loss in the compression level.

Table 5.5: Level/direction-wise for case (a) global thresholding

Level/direction-wise	Horizontal	Diagonal	Vertical
Level 1	7.2×10^{-11}	7.2×10^{-11}	7.2×10^{-11}
Level 2	7.2×10^{-11}	7.2×10^{-11}	7.2×10^{-11}
Level 3	7.2×10^{-12}	7.2×10^{-11}	7.2×10^{-12}
Level 4	7.2×10^{-12}	7.2×10^{-11}	7.2×10^{-12}
RMSE (arc-second)	0.006		
Comp. %	92.2%		
Storage (MB)	9.4		

Table 5.6: Level/direction-wise for case (b) global thresholding

Level/direction-wise	Horizontal	Diagonal	Vertical
Level 1	7.2×10^{-10}	7.2×10^{-10}	7.2×10^{-10}
Level 2	7.2×10^{-10}	7.2×10^{-10}	7.2×10^{-10}
Level 3	7.2×10^{-11}	7.2×10^{-10}	7.2×10^{-11}
Level 4	7.2×10^{-11}	7.2×10^{-10}	7.2×10^{-11}
RMSE (arc-second)	0.03		
Comp. %	95.5%		
Storage (MB)	9.4		

Table 5.7: Level/direction-wise for case (c) global thresholding

Level/direction-wise	Horizontal	Diagonal	Vertical
Level 1	7.2×10^{-10}	7.2×10^{-9}	7.2×10^{-10}
Level 2	7.2×10^{-10}	7.2×10^{-10}	7.2×10^{-10}
Level 3	7.2×10^{-10}	7.2×10^{-10}	7.2×10^{-10}
Level 4	7.2×10^{-10}	7.2×10^{-10}	7.2×10^{-10}
RMSE (arc-second)	0.07		
Comp. %	96.4%		
Storage (MB)	9.4		

Table 5.8: Level/direction-wise for case (d) global thresholding

Level/direction-wise	Horizontal	Diagonal	Vertical
Level 1	7.2×10^{-9}	7.2×10^{-8}	7.2×10^{-9}
Level 2	7.2×10^{-10}	7.2×10^{-8}	7.2×10^{-10}
Level 3	7.2×10^{-10}	7.2×10^{-9}	7.2×10^{-10}
Level 4	7.2×10^{-10}	7.2×10^{-9}	7.2×10^{-10}
RMSE (arc-second)	0.38		
Comp. %	97.1%		
Storage (MB)	9.4		

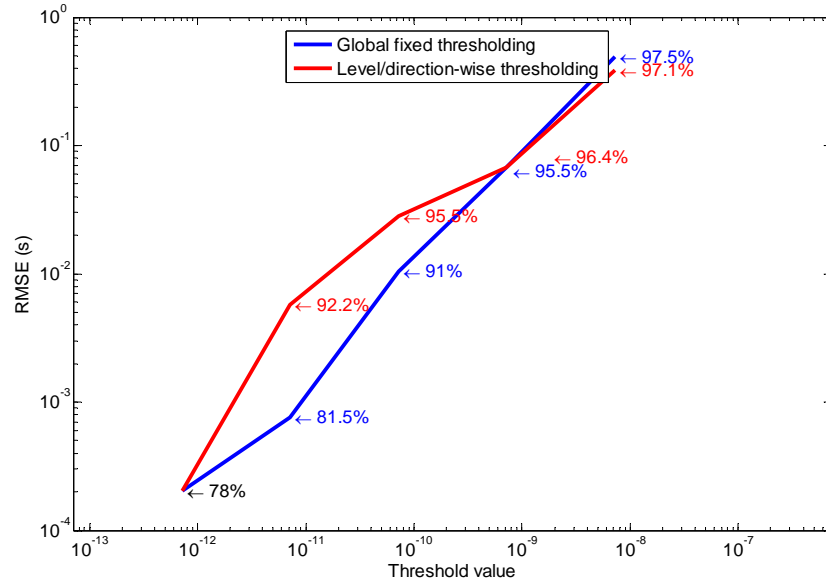


Figure 5.20: Global fixed thresholding versus level/direction-wise thresholding for the Vening Meinesz integral (vertical component)

The comparison between the global thresholding cases and level direction-wise thresholding are summarized in Figure 5.20. Again, it can be seen that the intersection between the two curves is close to the optimum compression level and accuracy.

As a concluding remark, the high thresholding values can be applied to the first and second levels of decomposition at the diagonal direction. These values are five orders of magnitude higher than the value obtained from Equation (3.41) or (3.42). In the other directions and levels, the thresholding values are chosen with values equal to two or three higher orders of magnitude than the one obtained from the empirical equations.

5.3 Evaluation of the terrain correction integral

The terrain correction integral was also evaluated using wavelet techniques; Equations (2.22) to (2.25) are used in this study. The methodology of investigation introduced in Section 3.6 is followed to evaluate the integral by the wavelet full matrix solution, wavelet global thresholding, and level/direction-wise thresholding.

5.3.1 Data and wavelet used

The data used is a set of point heights (Figure 5.21), on a 56×36 grid with $1 \text{ km} \times 1 \text{ km}$ spacing. The area is of very rough terrain; the statistics of the data heights are shown in Table 5.9. Again, the Daubechies wavelet with four vanishing moments is used.

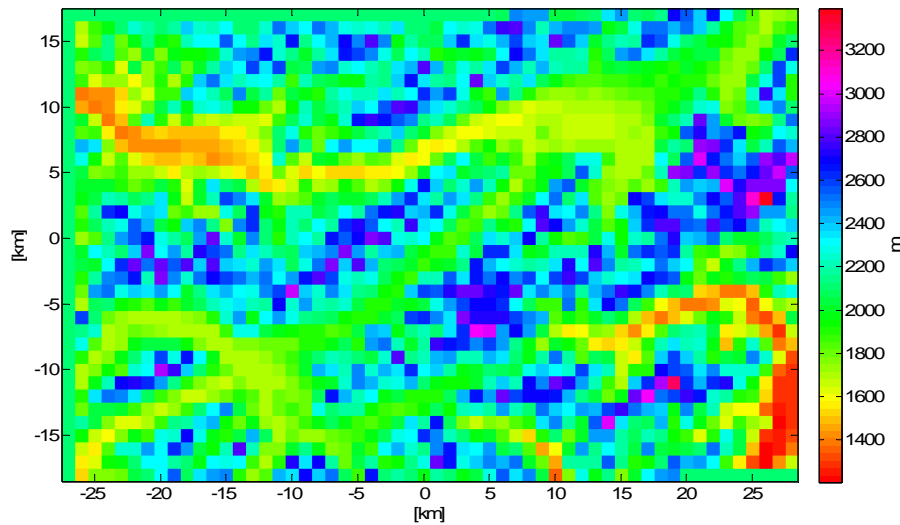


Figure 5.21: Point heights (m)

Table 5.9: Height statistics

Max. (m)	Min. (m)	Mean (m)	σ (m)
3395	1204	2115.08	2143.91

5.3.2 Wavelet full matrix solution

The design matrix A is formed from the wavelet coefficients of the terrain correction kernels at different computational points. The wavelet solution is shown in Figure 5.22. The wavelet full matrix solution is compared with the numerical integration solution (Figure 5.23). These two solutions are practically identical with an RMSE equal to 0.000 mGal.

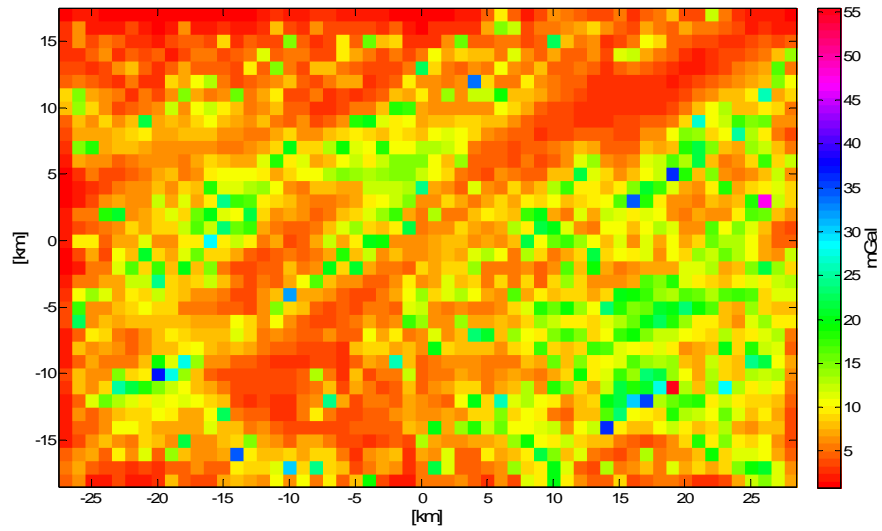


Figure 5.22: Wavelet full matrix solution of the terrain correction integral

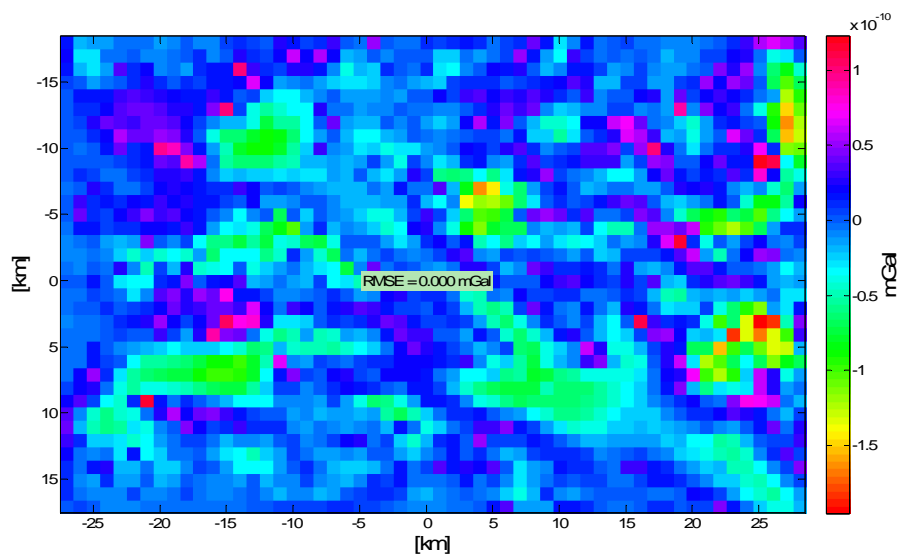


Figure 5.23: Difference between wavelet full matrix solution and the numerical integration solution for the terrain correction integral

5.3.3 Wavelet global fixed thresholding solution

For the terrain correction integral with 1 km by 1 km spacing kernel, the threshold value estimated from Equations (3.41) or (3.42) is 6.7×10^{-7} . The solution at 70% compression level is numerically identical to the numerical integration approach; see Figure 5.24. This value is used as reference for other larger thresholding values. Six other different thresholding values are globally tested to reach the maximum compression level with an acceptable RMSE in comparison to numerical integration: the target accuracy is 0.1 mGal.

In Table 5.10 and Figure 5.25, the design matrix A became sparser with the increase of the thresholding value by one order of magnitude (6.7×10^{-6} , 6.7×10^{-5} , 6.7×10^{-4} , 6.7×10^{-3} , 6.7×10^{-2} and 6.7×10^{-1}) until the maximum compression level was achieved. From Table 5.10 and Figure 5.26, the maximum compression level achieved by the global thresholding method within the range of the target accuracy is 93% with RMSE of 0.13 mGal (case (d)). For the thresholding values in cases (e) and (f), higher compression levels are achieved but with a huge degradation in the accuracy (1.42 and 9.56 mGal).

5.3.4 Level/direction-wise thresholding solution

In this subsection, an improvement is made to the six global thresholding cases, which were introduced in Subsection 5.3.3. The improvement is for both the compression levels and the accuracy. Three examples illustrate the efficiency of this algorithm. Case (c) is an example of improving the compression level without a significant loss of accuracy. Cases (e) and (f) are examples of improving the accuracy with a small decrease in the compression level.

For global thresholding case (c), the combination in Table 5.11 leads to a 3.4% gain in compression level with no significant loss in accuracy (0.09 mGal). The accuracy is still in the range of the target accuracy, which is 0.1 mGal RMS. For global thresholding cases (e) and (f), the target is to improve the accuracy by the level/direction-wise thresholding technique. In case (e), the RMS accuracy improved from 1.42 mGal to

0.21 mGal (85% improvement) with a 1.5% loss in the compression level; see Table 5.12. Another example can be seen in Table 5.13; although the accuracy does not meet the target accuracy, the example illustrates the effectiveness of the level/direction-wise algorithm. For case (f), a combination of three values improved the accuracy from 9.56 mGal to 1.35 mGal (85% improvement), with a 1.6% loss in the compression level (97.7% to 96.1%).

Table 5.10: Wavelet global thresholding solutions versus wavelet full matrix solution for the terrain correction integral

Hard thresholding	Full matrix	Global Eq. (3.41) or (3.42)	(a)	(b)	(c)	(d)	(e)	(f)
Thresholding value	-	6.7×10^{-7}	6.7×10^{-6}	6.7×10^{-5}	6.7×10^{-4}	6.7×10^{-3}	6.7×10^{-2}	6.7×10^{-1}
Storage (MB)	52	23.5	20.1	12.3	8.4	5.5	3.2	1.8
RMSE (mGal)	-	0.000	0.001	0.01	0.03	0.13	1.42	9.56
No. of elements	6662425	2006028	1713534	1047865	714946	470781	269414	157303
Comp%	0%	70%	75%	84.3%	89.3%	93%	96%	97.7%

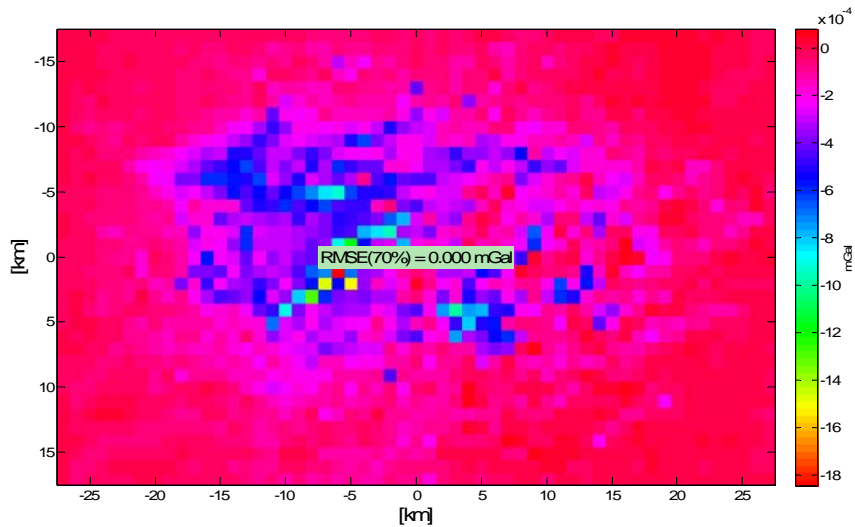


Figure 5.24: Difference between wavelet global thresholding and numerical integration solution for the terrain correction

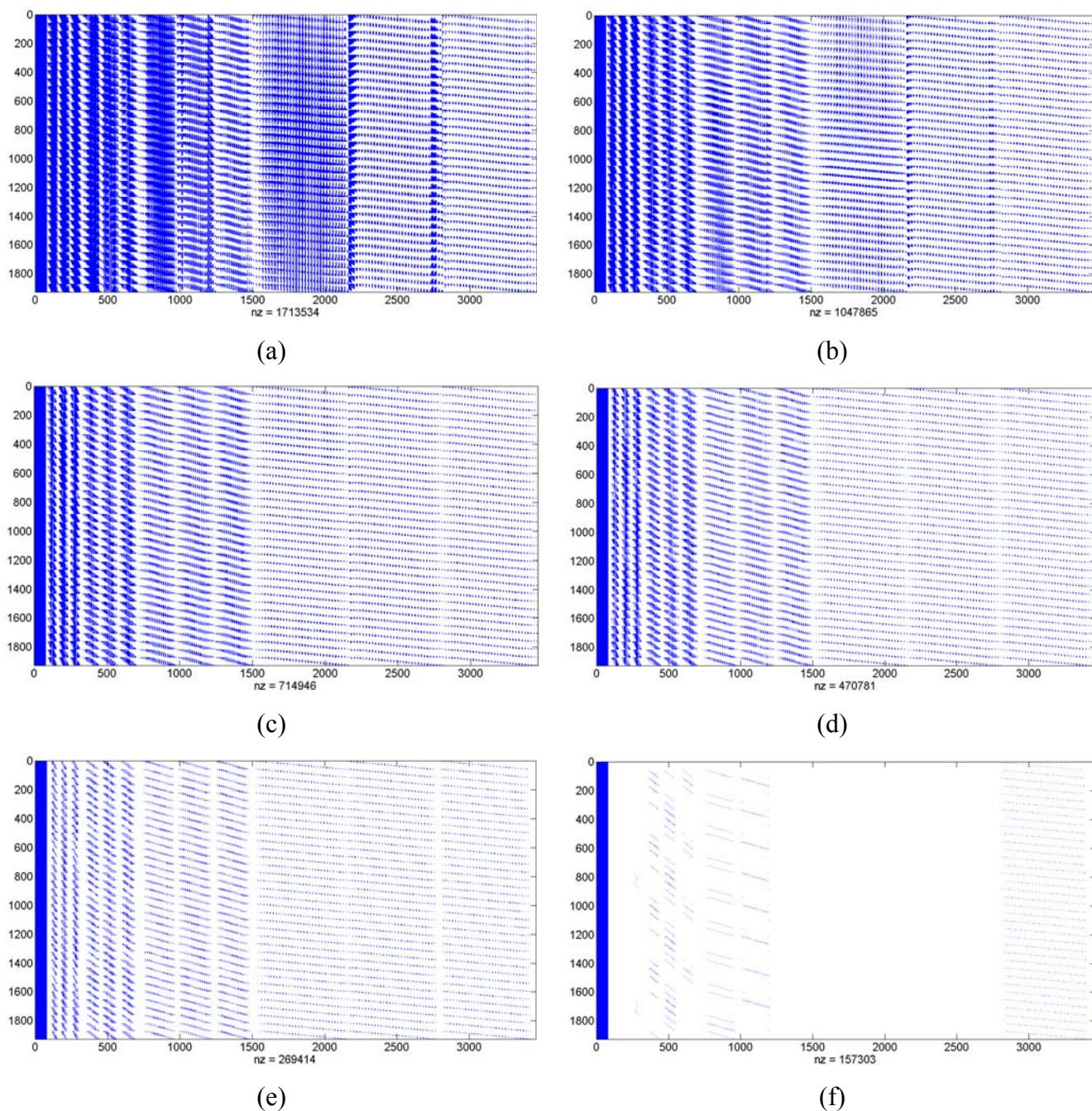


Figure 5.25: A matrix at six thresholding values (6.7×10^{-6} , 6.7×10^{-5} , 6.7×10^{-4} , 6.7×10^{-3} , 6.7×10^{-2} and 6.7×10^{-1}); each blue spot represents a nonzero value in the terrain correction kernel.

Figure 5.27 shows a comparison among the six cases of the global thresholding and their modifications using level/direction-wise thresholding. The optimal case is almost at the intersection of the two approaches, with a 93% compression level and a 0.13 mGal RMSE, which is very close to the target accuracy.

Table 5.11: Level/direction-wise for case (c) global thresholding

Level/direction-wise	Horizontal	Diagonal	Vertical
Level 1	6.7×10^{-3}	6.7×10^{-3}	6.7×10^{-3}
Level 2	6.7×10^{-3}	6.7×10^{-3}	6.7×10^{-3}
Level 3	6.7×10^{-4}	6.7×10^{-3}	6.7×10^{-4}
Level 4	6.7×10^{-4}	6.7×10^{-3}	6.7×10^{-4}
RMSE (mGal)	0.09		
Comp. %	92.7%		
Storage (MB)	7.2		

Table 5.12: Level/direction-wise for case (e) global thresholding

Level/direction-wise	Horizontal	Diagonal	Vertical
Level 1	6.7×10^{-2}	6.7×10^{-2}	6.7×10^{-2}
Level 2	6.7×10^{-3}	6.7×10^{-3}	6.7×10^{-3}
Level 3	6.7×10^{-3}	6.7×10^{-3}	6.7×10^{-3}
Level 4	6.7×10^{-3}	6.7×10^{-3}	6.7×10^{-3}
RMSE (mGal)	0.21		
Comp. %	94.5%		
Storage (MB)	4.8		

Table 5.13: Level/direction-wise for case (f) global thresholding

Level/direction-wise	Horizontal	Diagonal	Vertical
Level 1	6.7×10^{-1}	6.7×10^{-1}	6.7×10^{-1}
Level 2	6.7×10^{-2}	6.7×10^{-1}	6.7×10^{-2}
Level 3	6.7×10^{-3}	6.7×10^{-2}	6.7×10^{-3}
Level 4	6.7×10^{-3}	6.7×10^{-3}	6.7×10^{-3}
RMSE (mGal)	1.35		
Comp. %	96.1%		
Storage (MB)	3.8		

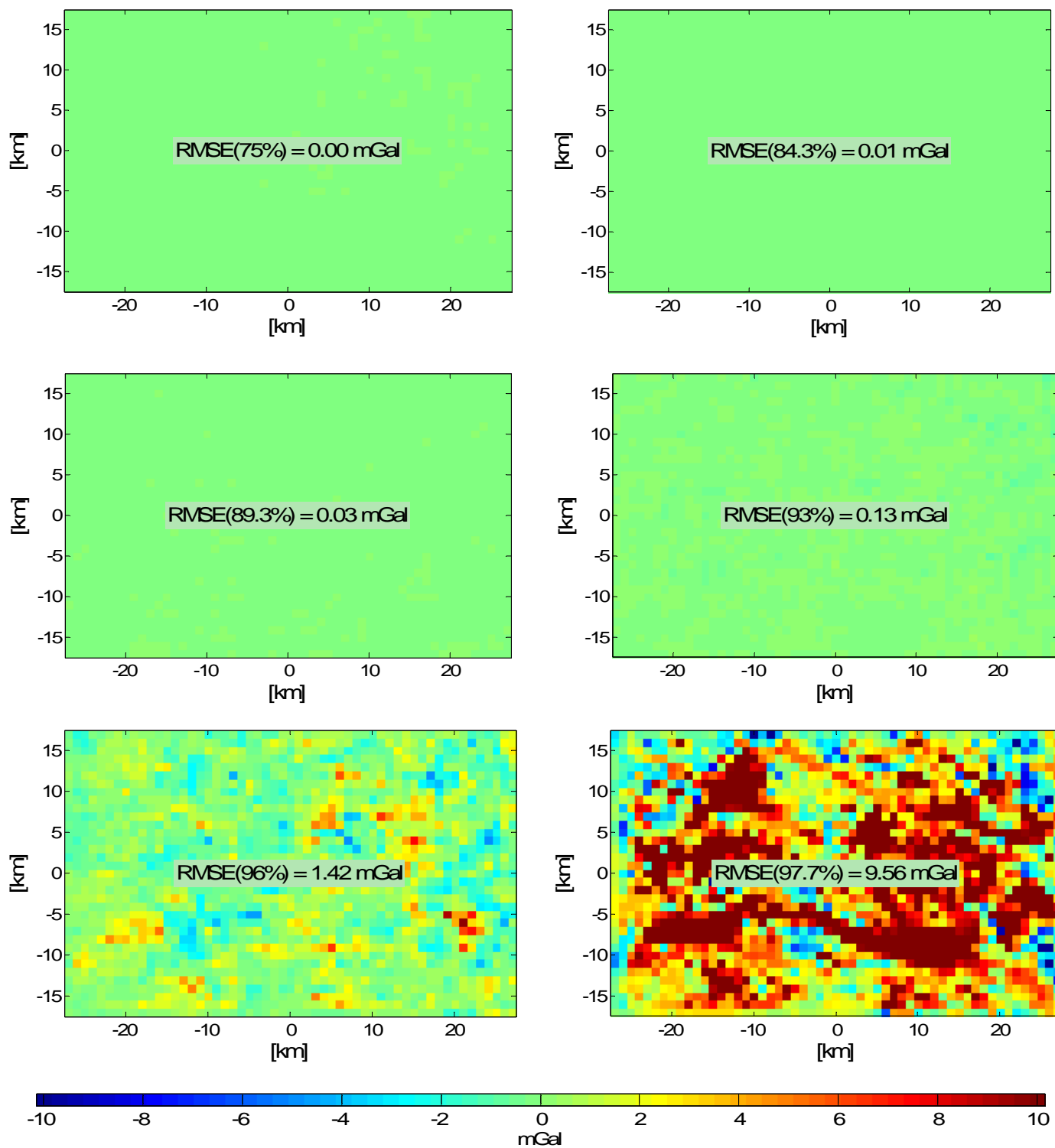


Figure 5.26: Wavelet global thresholding fixed solution in comparison to numerical integration solution for the terrain correction integral

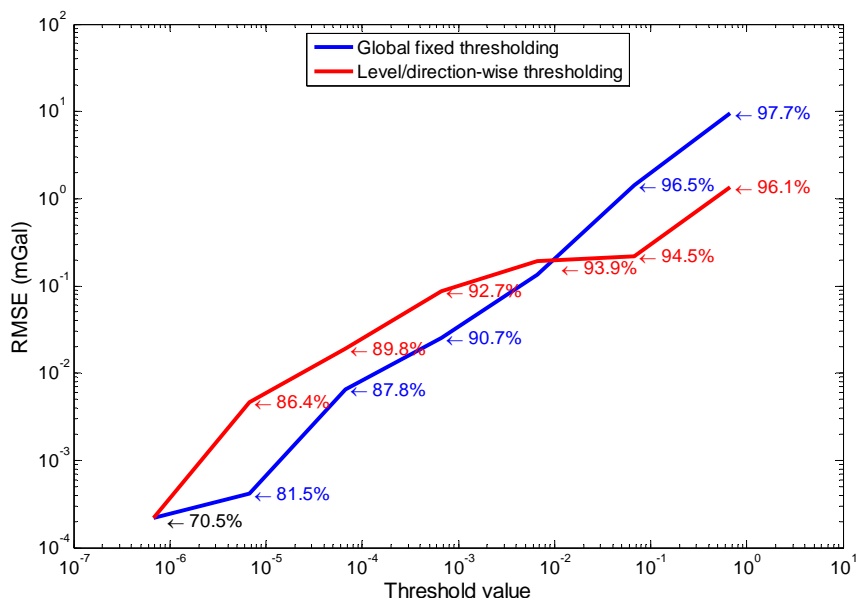


Figure 5.27: Global fixed thresholding versus level/direction-wise thresholding for the terrain correction integral

5.4 Evaluation of the upward continuation integral

The main aim of this section is the evaluation of the Poisson integral using the new developed wavelet algorithm (Section 3.5). The upward continuation integral is evaluated using the wavelet full matrix solution, FFT, and numerical integration. The methodology of investigation introduced in Section 3.6 is followed.

5.4.1 Data and wavelet used

The data are gravity disturbances created from upward continued data for the Kananaskis region [Glennie and Schwarz, 1997]. The data is created at two altitudes: 4370 m and 7288 m. The two sets of data are shown in Figure 5.28. They are on the same grid with 30" spacing in the North-South direction and 60" spacing in the East-West direction. The data at the 4370 m altitude is upward continued to the 7288 m altitude using the Poisson integral. The data at 7288 m is used as reference data for the evaluation of the upward continuation integral. The Daubechies wavelet with four vanishing moments is used.

5.4.2 Wavelet full matrix solution

The design matrix built from the two-dimensional wavelet transform of the kernel is shown in Figure 5.29. The wavelet full matrix solution is obtained using Equation (3.61); see Figure 5.30. The difference between the full matrix solution and the reference data, shown in Figure 5.31, has an RMSE of 8.525 mGal. The upward continuation integral is also solved by both the numerical integration and the FFT approaches. The wavelet full matrix, FFT, and the numerical integration solutions are identical; the difference between the numerical integration and the wavelet full matrix solution is shown in Figure 5.31, with an RMSE equal to zero mGal.

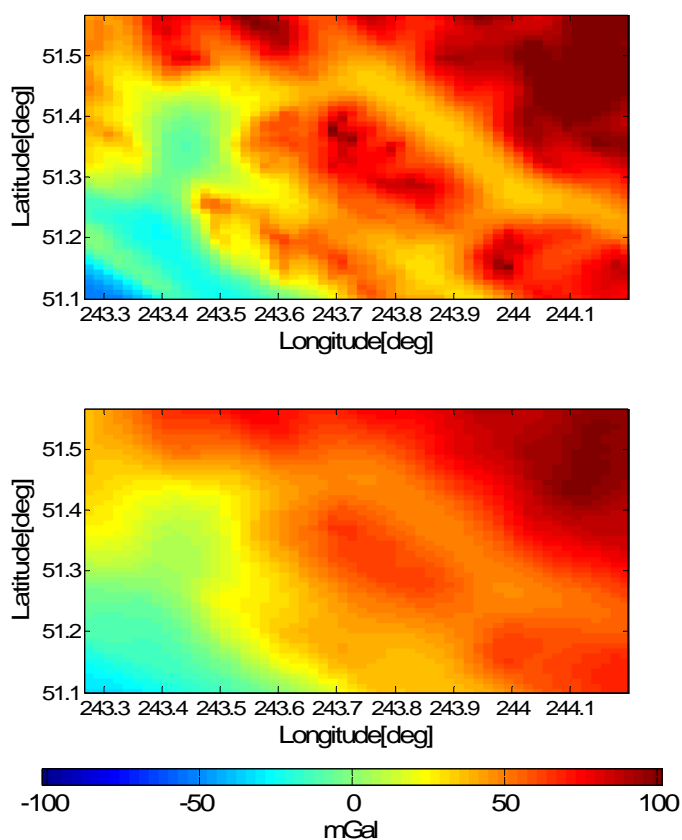


Figure 5.28: Gravity disturbances at the Kananaskis region at 4370 m (up) and 7288 m (down) altitudes.

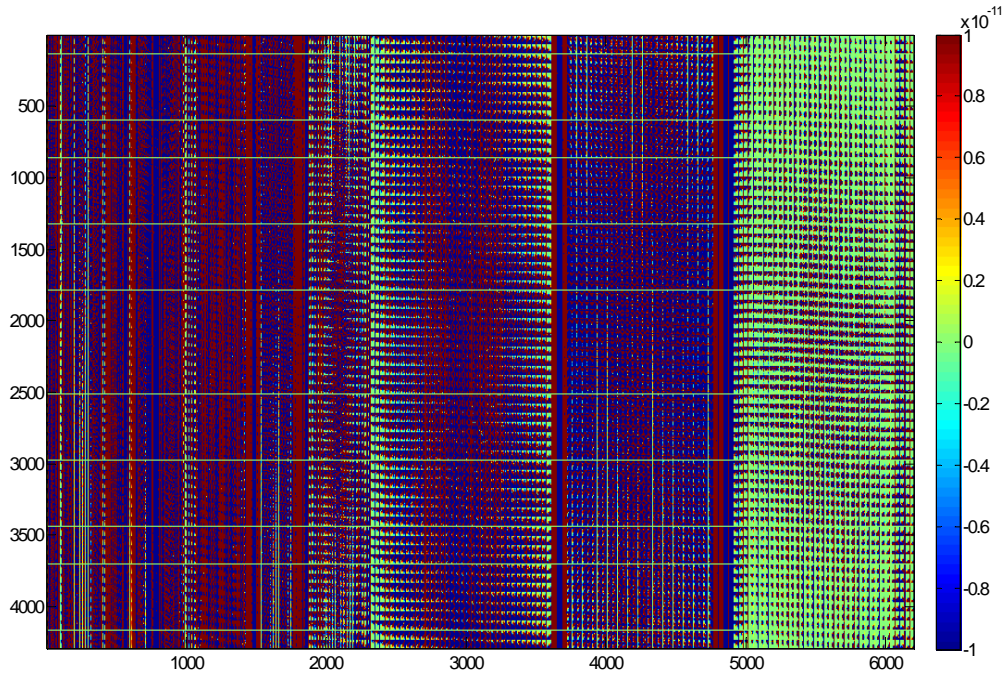


Figure 5.29: Poisson kernels' A design matrix (unitless)

5.4.3 Wavelet global fixed thresholding solution

First, the global thresholding value is computed from the Equation (3.41) or (3.42). A compression level equal to 76% is achieved (Figure 5.32), with no loss of accuracy in comparison to the numerical integration solution (Figure 5.33). Starting with the reference thresholding value (6.3×10^{-8}), it is increased four times by an order of magnitude (6.3×10^{-7} , 6.3×10^{-6} , 6.3×10^{-5} , and 6.3×10^{-4}); see Table 5.14. The use of higher thresholding values (four global cases) leads to a dramatic decrease in the size of the matrix, as shown in Figure 5.34.

The first three cases have RMSE less than the target accuracy (0.1 mGal); see Figure 5.35. For case (d), a higher compression level is achieved but with a large degradation in the accuracy (0.308 mGal). The degradation occurs because part of the main energy of the A matrix is removed.

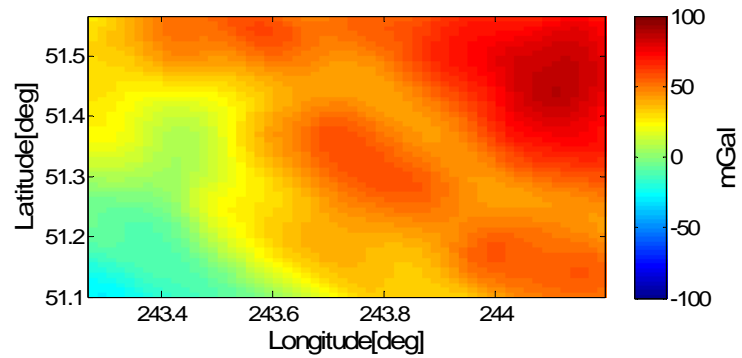


Figure 5.30: Wavelet full matrix solution for upward continuation (Poisson integral) from 4370 m to 7288 m

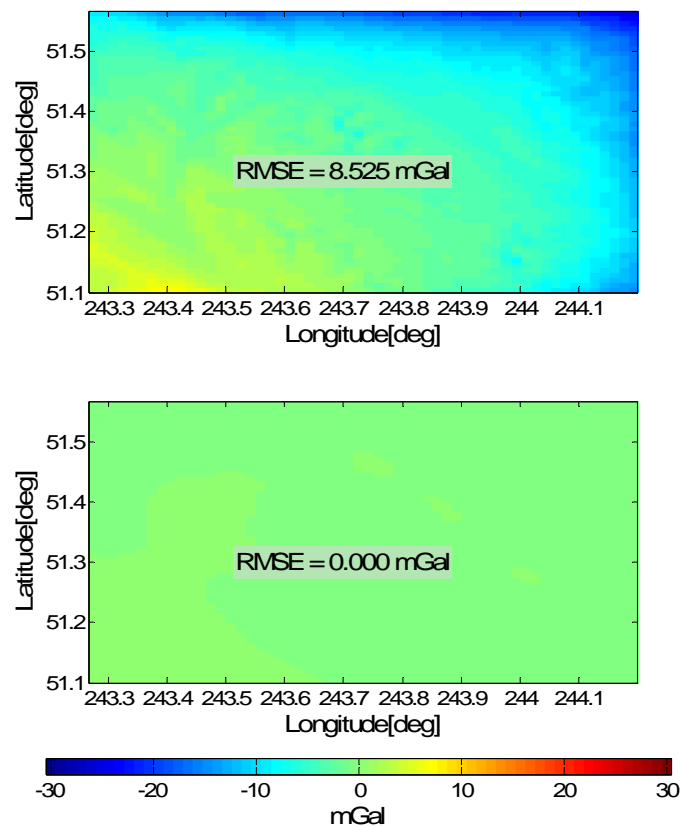


Figure 5.31: Wavelet full matrix solution differences from reference data (up) and numerical integration solution (down)

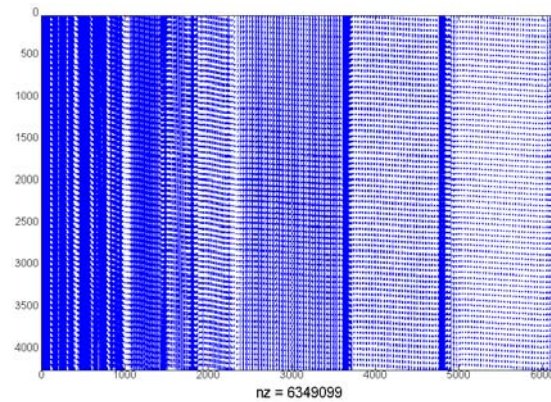


Figure 5.32: Design matrix A of the global thresholding values (6.3×10^{-8}); each blue spot represents a nonzero value for the upward continuation integral

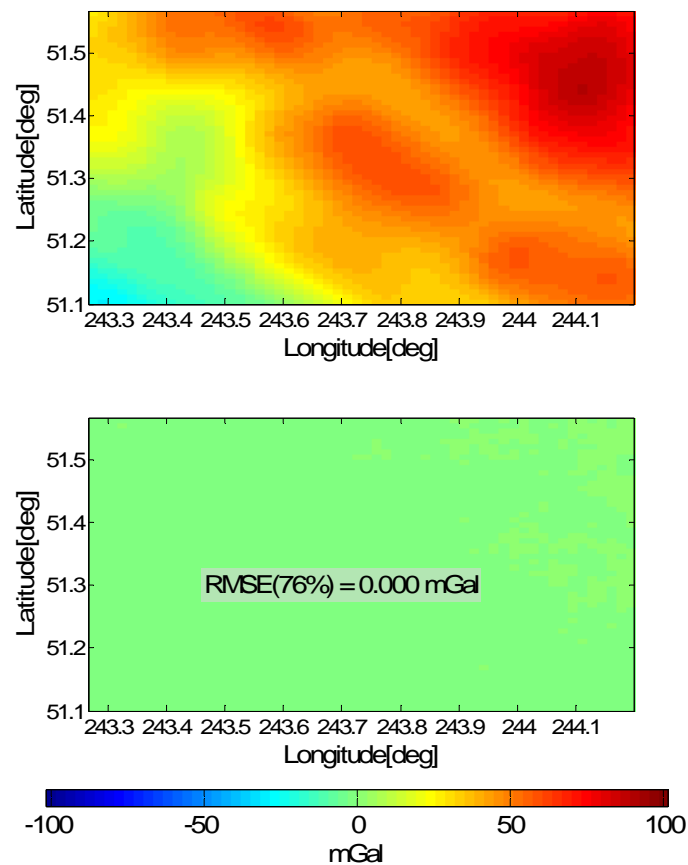


Figure 5.33: Global hard thresholding solution (up) and difference from numerical integration solution (down) for the upward continuation integral

Table 5.14: Wavelet global fixed thresholding versus wavelet full matrix solution for the evaluation of the upward continuation integral

Hard thresholding	Full matrix	Global eq. (3.41) or (3.42)	(a)	(b)	(c)	(d)
Thresholding value	-	6.3×10^{-8}	6.3×10^{-7}	6.3×10^{-6}	6.3×10^{-5}	6.3×10^{-4}
Storage (MB)	186	72.6	60.41	30.94	16.5	9.14
RMSE (mGal)	-	0.000	0.001	0.018	0.098	0.308
No. of elements	26190775	6349099	5276895	2702207	1441172	797085
Comp%	0%	76%	79.8%	89.7%	94.5%	97%

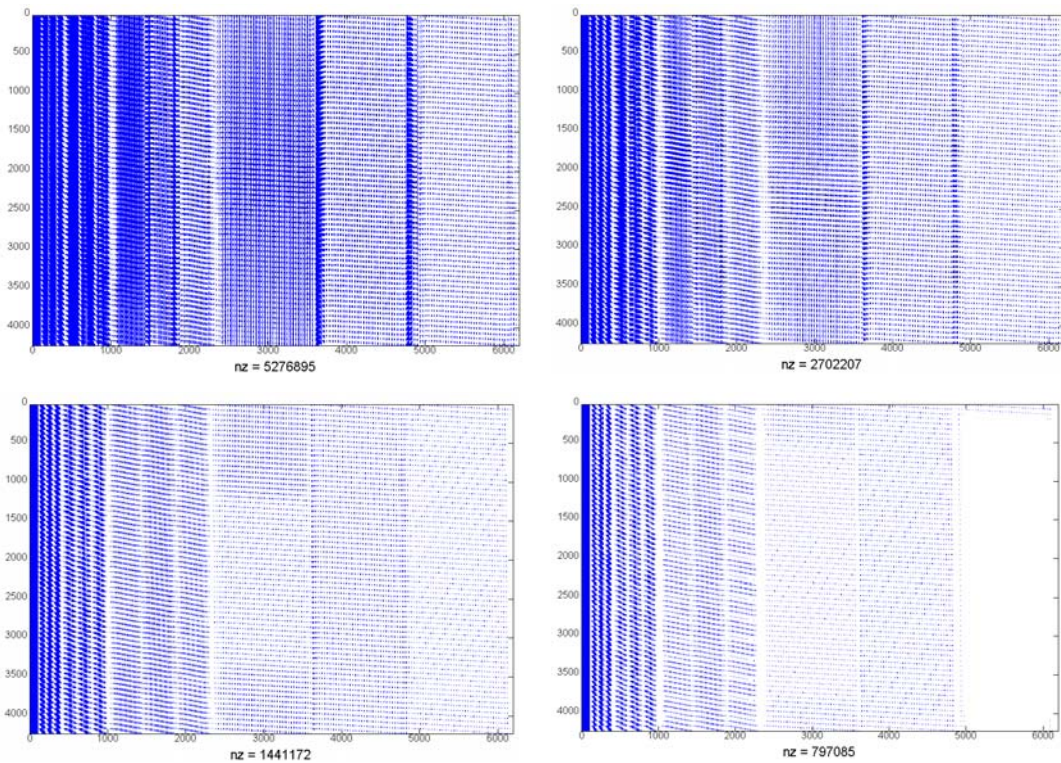


Figure 5.34: A matrix at different thresholding values (6.3×10^{-7} , 6.3×10^{-6} , 6.3×10^{-5} , and 6.3×10^{-4}); each blue spot represents a nonzero value in the Poisson kernel.

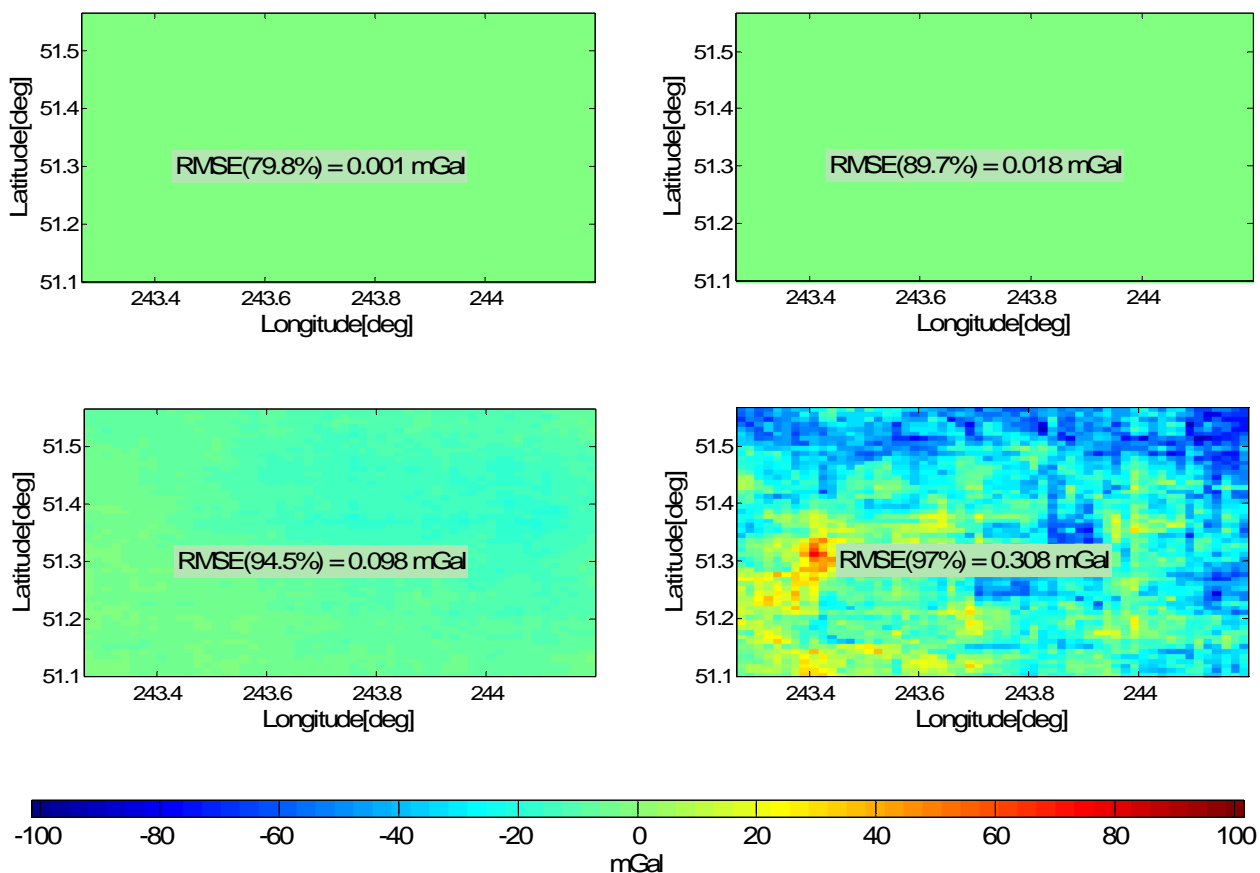


Figure 5.35: Global thresholding solutions at four compression levels in comparison to the numerical integration solution for the upward continuation integral

5.4.4 Level/direction-wise thresholding solution

Different combinations of the thresholding values for the improvement of the four global thresholding cases, (a), (b), (c), and (d), are tested. Two examples are illustrated in detail. The first combination is shown in Table 5.15 for the global thresholding case (a). This combination increases the compression level from 79.8% to 90.8%, with almost no loss of accuracy (RMSE is equal to 0.01 mGal). The achieved accuracy is better than the targeted practical one (0.1 mGal). Cases (b) and (c) are similar to case (a), where the level direction-wise thresholding approach is used to increase the compression level and maintain the RMS accuracy.

For case (d), the target is to improve the RMS accuracy without a significant loss in the compression percentage; see Table 5.16. The level/direction-wise thresholding decreased the compression level by 0.3% (97% to 96.7%) with an RMSE equal to 0.18 mGal instead of 0.308 mGal, which is still an acceptable practical accuracy. The comparison between the global fixed thresholding approach and the level/direction-wise thresholding is summarized in Figure 5.36. The red curve is almost horizontal between cases (c) and (d), which indicates that the optimum compression level with an acceptable accuracy is at the intersection of the two curves, with almost 96.5% compression level.

Table 5.15 Level/direction-wise for case (a) global thresholding

Level/direction-wise	Horizontal	Diagonal	Vertical
Level 1	6.3×10^{-6}	6.3×10^{-6}	6.3×10^{-6}
Level 2	6.3×10^{-6}	6.3×10^{-6}	6.3×10^{-6}
Level 3	6.3×10^{-7}	6.3×10^{-6}	6.3×10^{-7}
Level 4	6.3×10^{-7}	6.3×10^{-6}	6.3×10^{-7}
RMSE (mGal)	0.01		
Comp. %	90.8%		
Storage (MB)	29		

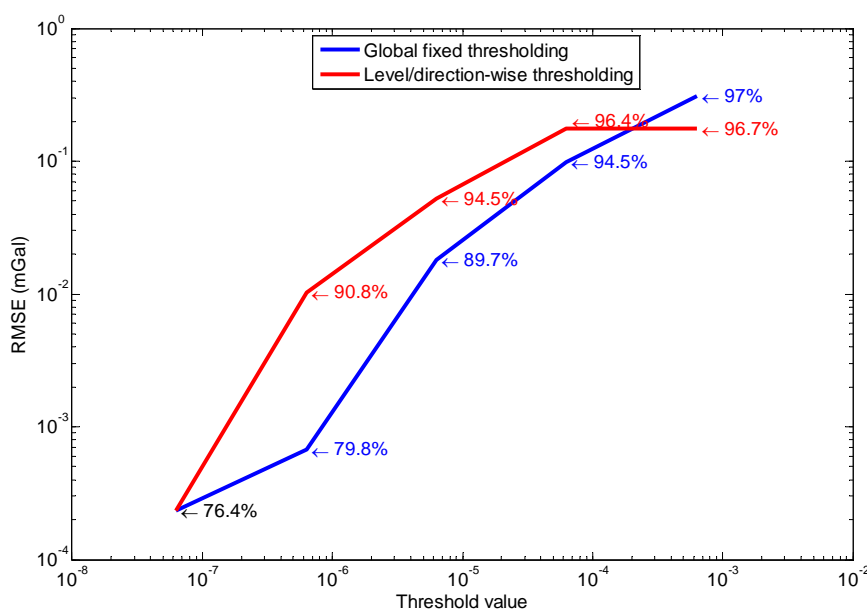


Figure 5.36: Global fixed thresholding versus level/direction-wise thresholding for the evaluation of the upward continuation integral

Table 5.16: Level/direction-wise for case (d) global thresholding

Level/direction-wise	Horizontal	Diagonal	Vertical
Level 1	6.3×10^{-4}	6.3×10^{-3}	6.3×10^{-4}
Level 2	6.3×10^{-4}	6.3×10^{-3}	6.3×10^{-4}
Level 3	6.3×10^{-4}	6.3×10^{-4}	6.3×10^{-4}
Level 4	6.3×10^{-5}	6.3×10^{-5}	6.3×10^{-5}
RMSE (mGal)	0.18		
Comp. %	96.7%		
Storage (MB)	11		

5.5 Summary

New two-dimensional wavelet transform evaluations of several geodetic integrals were introduced. Three wavelet transform implementations were introduced: wavelet full matrix approach, wavelet global fixed thresholding, and level/direction-direction wise thresholding. The wavelet full matrix approach achieved identical results to the FFT and the numerical integration approaches when evaluating the Stokes, Vening Meinesz, terrain correction, and upward continuation integrals. The automated thresholding approach reached compression levels between 70% and 78% for all four integrals, with no loss in accuracy in comparison to the numerical integration solution. High compression levels were achieved using the global fixed thresholding approach. A significant loss in the accuracy occurred when the main energy of the kernel was thresholded.

The level/direction-wise thresholding reached very high compression levels with an acceptable accuracy in all cases. The Stokes integral reached a 95.2% compression level with 1.3 cm RMSE. In the case of the Vening Meinesz integral, 96.4% were achieved with 0.07 arc-second RMS accuracy. The terrain correction integral achieved 92.7% with 0.1 mGal RMSE. Finally, the upward continuation integral reached a 96.7% with 0.18 mGal RMS accuracy. The success of the new wavelet transform algorithm in achieving high compression levels with an acceptable accuracy for all the four integrals, which have different data sets, different grid size, and spacing, verifies its effectiveness in the evaluation of geodetic integrals in planar approximation.

From the previously mentioned results, the main outcomes of this chapter can be summarized as follows:

- The level/direction-wise thresholding can achieve a maximum compression level with an acceptable practical accuracy, which can be used effectively in pre-processing the data and decreasing the amount of computer memory and storage required for allocating and saving the data and the kernels, respectively. This can open the door for field checks during the measuring phase of different projects.
- As an example of these applications is the upward continuation integral and the terrain correction integral that can be used in airborne gravimetry applications and the computation of geoid undulations for GPS and levelling networks. Due to the high compression levels achieved, which are at least 90% for all cases, the corresponding kernels for each application can be pre-computed and stored for a large number of computational points and then applied whenever needed.

Chapter Six: Wavelet evaluation of inverse geodetic problems

Modern observation methods increase the amount of data available for solving inverse geodetic problems. Previously, not a lot of attention was drawn to this kind of problem, but with the invention of the spaceborne and airborne techniques, such as satellite altimetry and airborne gravimetry, inverse problems became more important. In this chapter, the evaluation of the different inverse problems will be studied. The inverse Vening Meinesz integral, the deflection-geoid formula, the inversion of the Stokes integral, and the inversion of the Poisson integral (downward continuation) will be evaluated.

The inverse Vening Meinesz integral and the deflection-geoid formula will be solved using wavelet full matrix, wavelet global thresholding, and wavelet level/direction-wise thresholding solutions. All these solutions will be compared to the reference data and the numerical integration solution. A new method for inverting the geodetic integrals will be tested on both the Stokes integral and the Poisson integral. Wavelet de-noising will be introduced as a regularization method for solving the noise amplification problem. The solution found by inverting the Stokes and the Poisson integrals will be compared with the reference data. Global fixed thresholding will be used to decrease the size of the matrices required for inverting the geodetic integrals.

6.1 Evaluation of the inverse geodetic integrals

In this section, the wavelet evaluation of inverse geodetic problems with modeled direction convolution formulae will be solved. Two integrals will be evaluated: the inverse Vening Meinesz integral and the deflection-geoid integral, using the methodology introduced in Section 3.6. The Daubechies wavelet with four vanishing moments will be used in both cases.

6.1.1 Evaluation of the inverse Vening Meinesz integral

The same data introduced in Sections 5.1.1 and 5.2.1 are used in the evaluation.

6.1.1.1 Wavelet full matrix solution

The procedure mentioned in Section 3.5 is used for the evaluation of the inverse Vening Meinesz integral (Equation (2.33)). First, the two-dimensional wavelet transform is applied to the vertical and horizontal components of the deflection of the vertical, after removing the long wavelength using the EGM96 geopotential model (degree 360). Each signal is decomposed into four levels of decomposition. Then, each of the two components' wavelet coefficients is transformed to a column vector (a_j^η and a_j^ξ) and the coefficients are arranged as shown Figure 3.11. Second, the two-dimensional wavelet transform with four levels of decomposition is applied to both kernels of the two components of the deflection of the vertical corresponding to all the computational points. The two design matrices A_{ij}^η and A_{ij}^ξ are built using the wavelet coefficients of the geodetic integral kernels; each line corresponds to one kernel (Figure 3.10). The solution is achieved by applying Equation (3.61) twice and summing up, as follows:

$$\Delta g_i = A_{ij}^\eta a_j^\eta + A_{ij}^\xi a_j^\xi \quad (6.1)$$

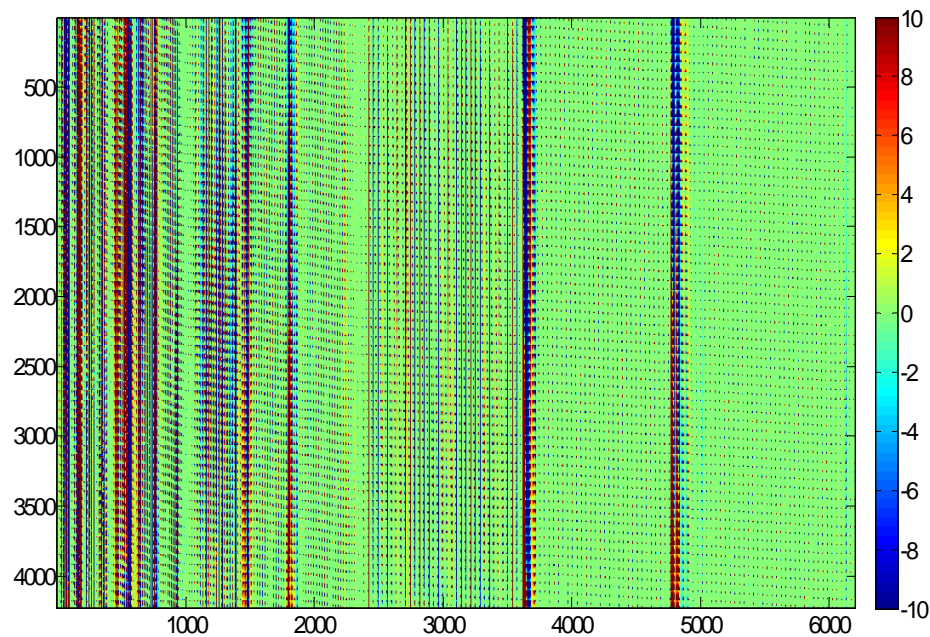


Figure 6.1: Inverse Vening Meinesz kernels' A design matrix (vertical component)

The comparison between Figure 6.1 and Figure 5.14 shows that there is an almost identical distribution of the values of the two-dimensional wavelet coefficients of the kernels. The main difference is the magnitude of these coefficients. As expected, the ratio between the values of the two color bars is of the order of γ^2 .

The wavelet full matrix solution is done by Equation (6.1) and the solution is shown in Figure 6.2. The difference of the wavelet full matrix solution from the reference data has an RMSE 36.78 mGal. As mentioned in Section 5.2.2, part of this difference is caused by the inconsistency of the gravity anomalies and the vertical component of the deflection of the vertical.

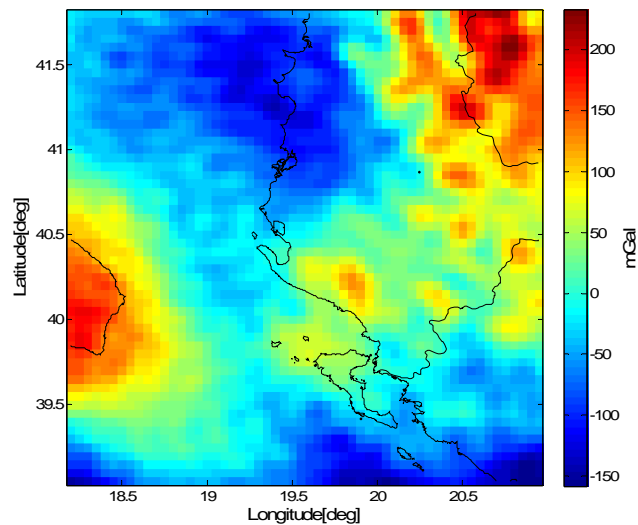


Figure 6.2: Wavelet full matrix solution of the inverse Vening Meinesz integral

The inverse Vening Meinesz problem is also evaluated using both the FFT and the numerical integration algorithms; both solutions are numerically identical. Figure 6.3 shows that the wavelet full matrix solution and the numerical integration approach are identical numerically with an RMSE equal to 0.00 mGal. This shows that the wavelet solution is accurate and at the same level of accuracy as the FFT and the numerical integration. Again, the only drawback of the wavelet approach is the size of the design matrices A_{ij}^n and A_{ij}^g , which are equal to 372 MB.

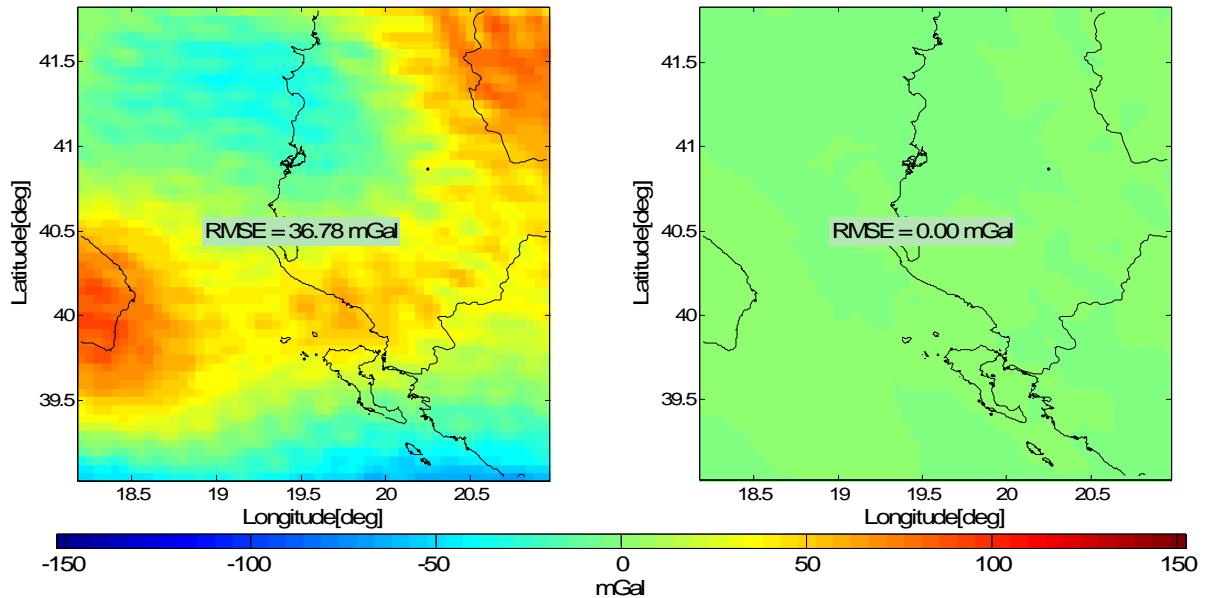


Figure 6.3: Wavelet full matrix solution differences from and the reference data (left) and the numerical integration solution (right) for the inverse Vening Meinesz integral

6.1.1.2 Wavelet global fixed thresholding solution

The global fixed thresholding approach, which is discussed in Section 4.3.1, is implemented in the wavelet evaluation of the inverse Vening Meinesz integral. As mentioned in Subsection 6.1.1.1, the difference between the design matrices A of the direct and the inverse Vening Meinesz integrals is mainly the magnitude of the two-dimensional wavelet coefficients. These values are larger in the case of the inverse Vening Meinesz integral by a factor of γ^2 . The thresholding value estimated from Equations (3.41) or (3.42) will increase by the same factor. The value is increased from 7.2×10^{-13} to 3.2×10^{-1} , which is roughly proportional to γ^2 in mGal. The solution corresponding to the estimated value is shown in Figure 6.4.

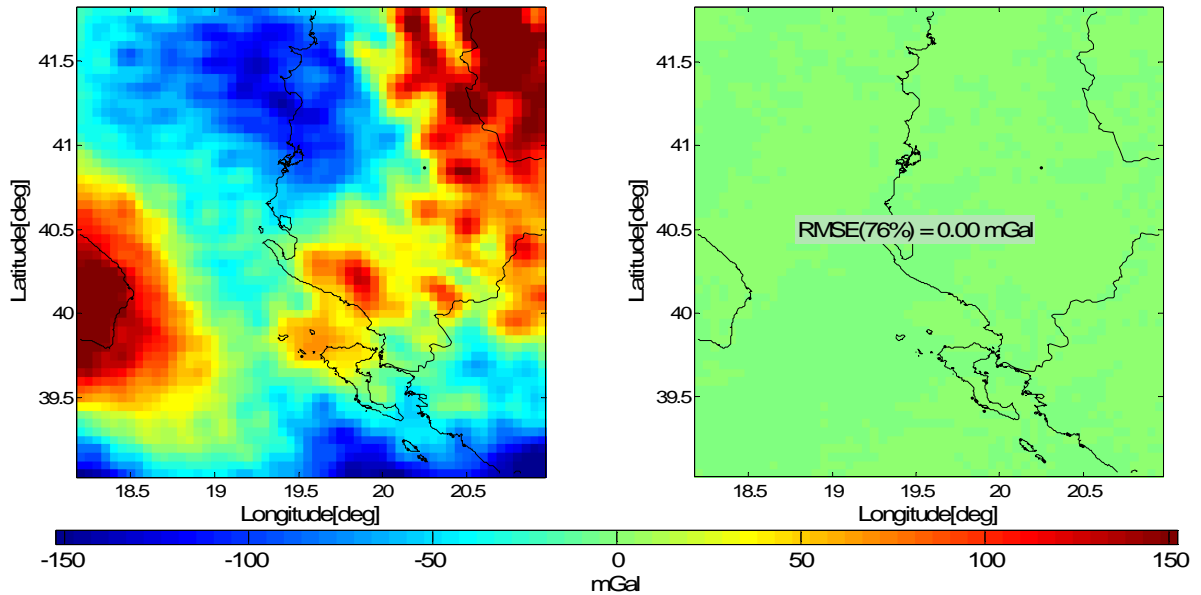


Figure 6.4: The wavelet global fixed thresholding solution with 76% compression (left) and the difference from the numerical integration solution (right) for the inverse Vening Meinesz integral

The same procedure is followed by increasing the thresholding values estimated from Equations (3.41) or (3.42) each time by one order of magnitude higher from the previous one. The memory size required for allocating the design matrices decreases dramatically with the increase of the thresholding values (Table 6.1). The target accuracy is 0.1 mGal RMS; this accuracy is satisfied until the global thresholding case (c) with an RMSE equal to 0.14 mGal and 94.4% compression level, as shown in Table 6.1 and Figure 6.4. For case (d), there is a dramatic degradation in the accuracy (RMSE of 1.23 mGal) at a compression level of 96.8%.

Although the two kernels of the inverse Vening Meinesz and the direct Vening Meinesz integrals are identical except for the constants outside the integral, the compression percentages in Table 6.1 and Table 5.4 are not identical. The difference is in the range of 1% and 3 as a result of the rounding error after multiplying with γ^2 (mGal).

Table 6.1: Wavelet global fixed thresholding versus wavelet full matrix solution for the inverse Vening Meinesz integral

Hard thresholding	Full matrix	Global Eq. (3.41) or (3.42)	(a)	(b)	(c)	(d)
Thresholding value	-	0.32	3.2	32	320	3200
Storage (MB)	372	102	96	52	29	19
RMSE (mGal)	-	0.000	0.00	0.01	0.14	1.23
No. of elements	52381550	12516592	11763474	5941194	2931310	1656424
Comp%	0%	76.1%	77.5%	88.7%	94.4%	96.8%

6.1.1.3 Level/direction-wise thresholding solution

The level/direction-wise thresholding effectiveness in improving the accuracy of the global fixed thresholding approach is tested. The level/direction-wise thresholding application to case (a) leads to a 13.4% increase in the compression level with no loss in the accuracy; see Table 6.2.

Table 6.2: Level/direction-wise for case (a) global thresholding

Level/direction-wise	Horizontal	Diagonal	Vertical
Level 1	32	32	32
Level 2	32	32	32
Level 3	3.2	32	3.2
Level 4	3.2	32	3.2
RMSE (mGal)	0.05		
Comp. %	90.9%		
Storage (MB)	43		

Another example is the application of the level/direction-wise thresholding to global thresholding case (d) by a combination of five different values (Table 6.3). Although the RMSE accuracy is higher than the target accuracy (0.1 mGal) and equal to 0.22 mGal, the improvement from the global case (1.23mGal) is significant (82%). The equivalent loss in the compression level is small and equal to 2.1% (96.8% to 94.7%). The comparison between the global fixed case and level/direction-wise thresholding is

shown in Figure 6.6 for all four cases (a), (b), (c), and (d). Figure 6.6 shows that the maximum compression level is in the range of 94.5% for the target accuracy.

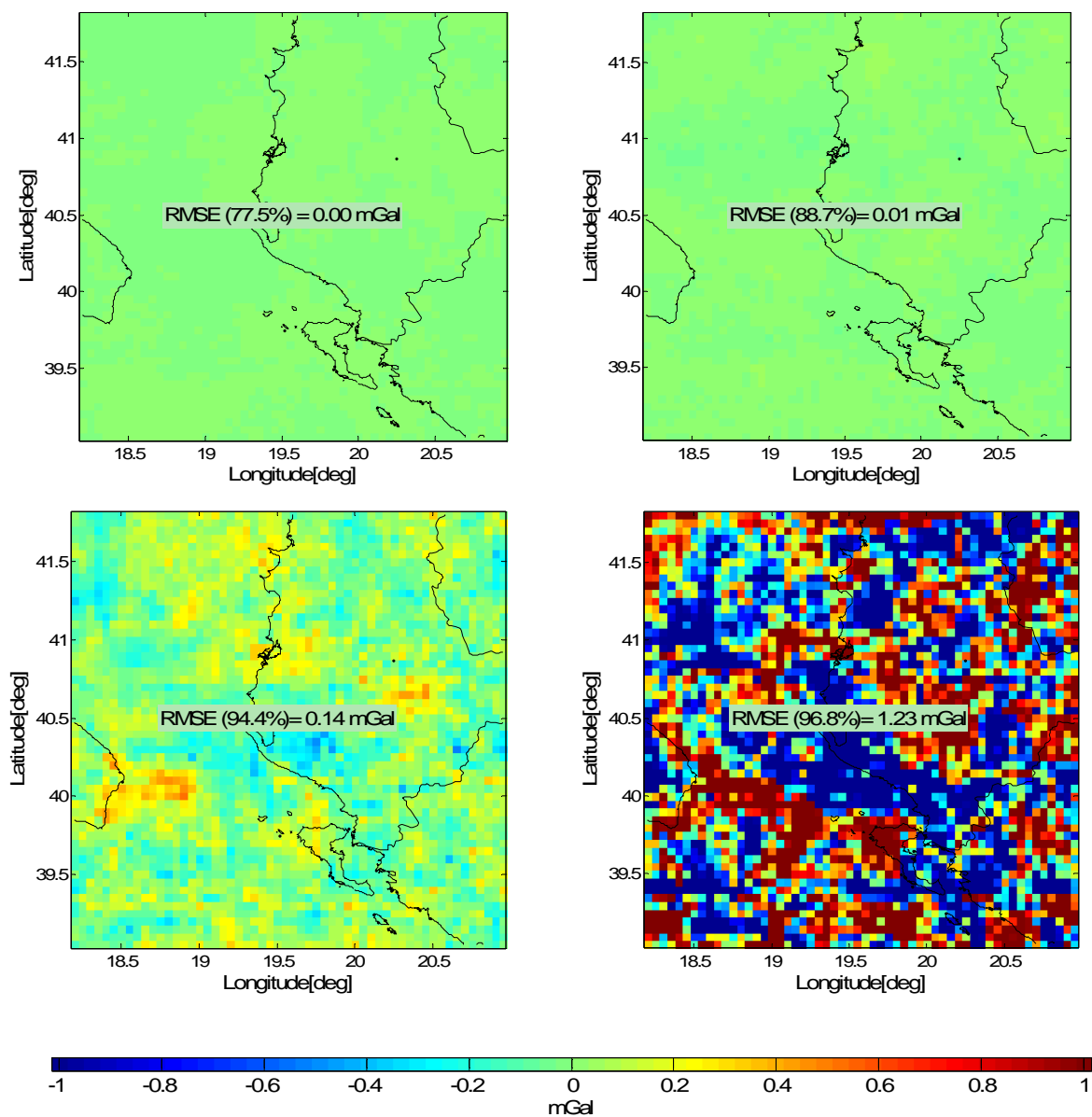


Figure 6.5: The difference between the wavelet global fixed thresholding solutions and numerical integration solution for the inverse Vening Meinesz integral

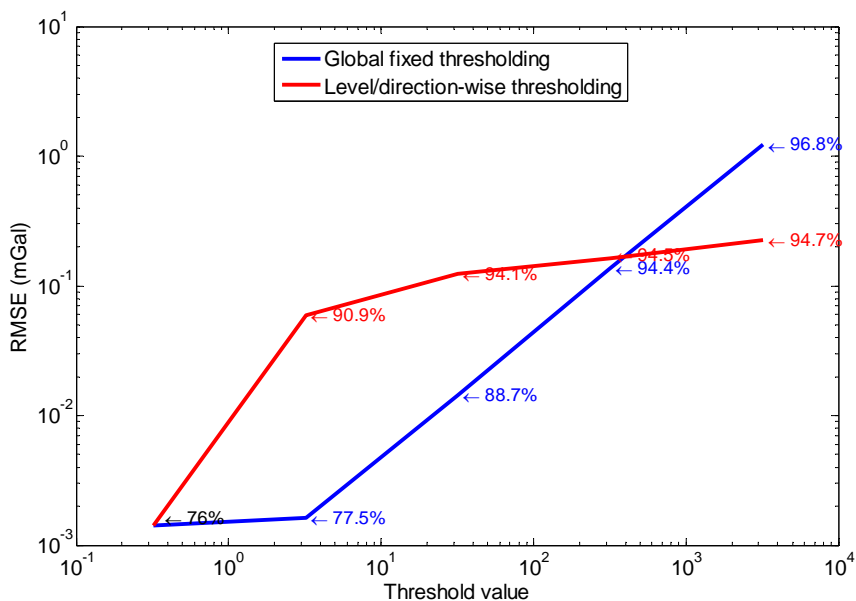


Figure 6.6: Global fixed thresholding versus level/direction-wise thresholding for the evaluation of the inverse Vening Meinesz integral

Table 6.3: Level/direction-wise for case (d) global thresholding

Level/direction-wise	Horizontal	Diagonal	Vertical
Level 1	320	32000	320
Level 2	160	3200	160
Level 3	32	320	32
Level 4	32	160	32
RMSE (mGal)	0.22		
Comp. %	94.7%		
Storage (MB)	28		

6.1.2 Evaluation of the deflection-geoid formula

The deflection-geoid formula (Equation (2.36)) is evaluated by the wavelet algorithm. The same two components of the deflection of the vertical introduced in Figure 5.13 are used.

6.1.2.1 Wavelet full matrix solution

The deflection-geoid formula design matrix A is shown in Figure 6.7. The wavelet full matrix solution is shown in Figure 6.8. The wavelet full matrix solution and

the numerical integration are almost identical numerically (Figure 6.9), with an RMSE equal to 0.00 m.

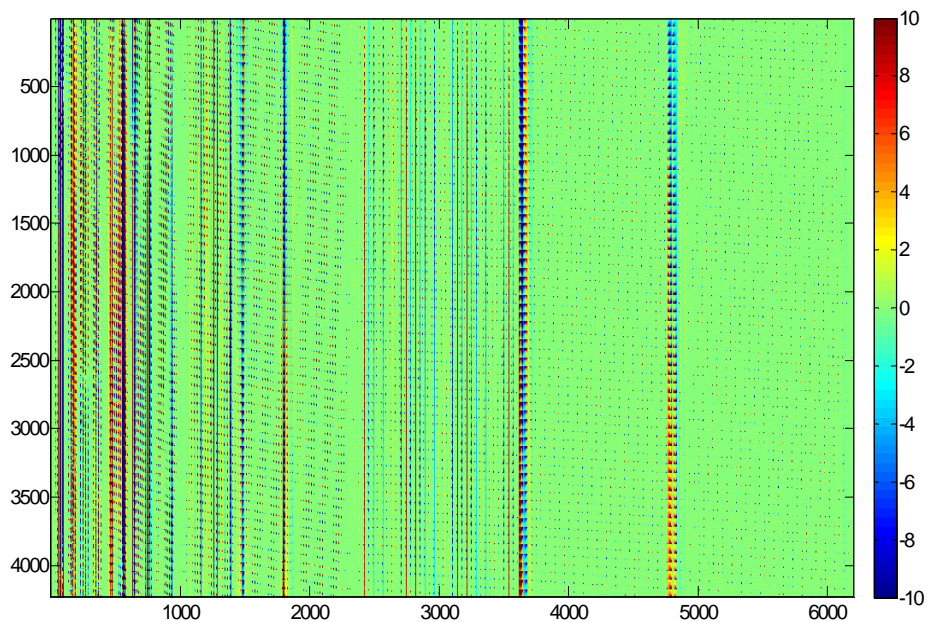


Figure 6.7: Deflection-geoid kernels' A design matrix

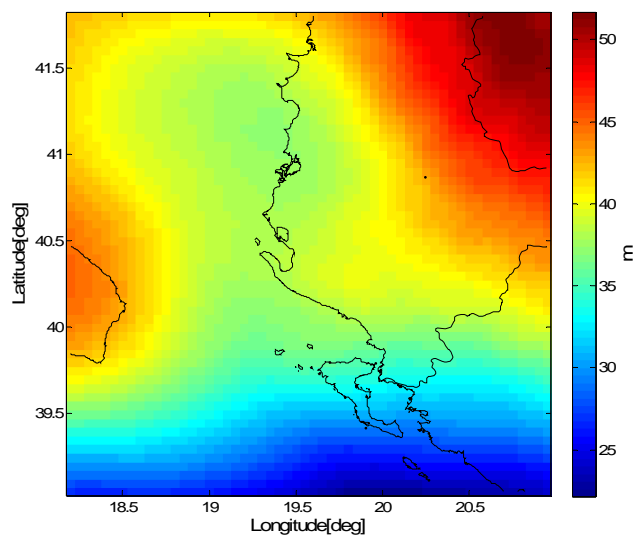


Figure 6.8: Wavelet full matrix solution of the deflection-geoid formula

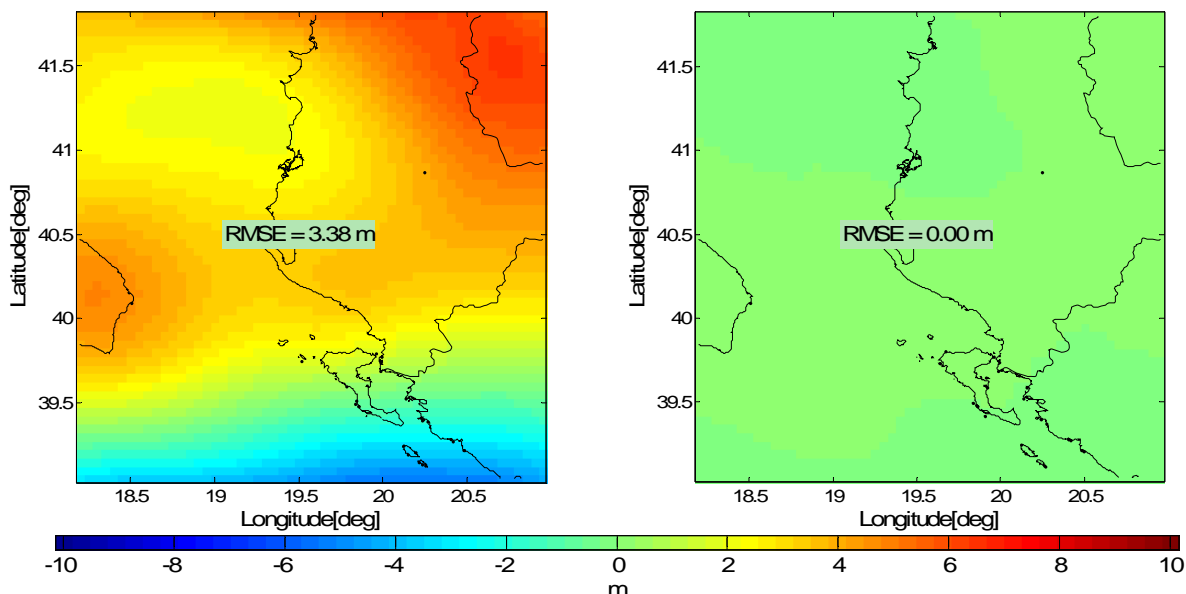


Figure 6.9: Difference between wavelet full matrix solution and the reference data (left), and numerical integration solution (right) for the deflection-geoid formula

The difference from the reference data (Figure 5.1) has an RMS accuracy of 3.38 m, which is not acceptable. This difference was expected because of the problem in the vertical component of the deflection of the vertical used in this solution. The main problem again is the size of the two design matrices, which is equal to 372 MB.

6.1.2.2 Wavelet global fixed thresholding solution

First, the wavelet thresholding value is estimated from Equation (3.41) or (3.42). A compression level equal to 76.6% (Figure 6.10) is obtained with no loss of accuracy (RMSE equal to zero m) in comparison to the numerical integration solution; see Figure 6.11.

Other higher thresholding values are tested; the compression levels achieved and the distribution of the values left after the thresholding are shown in Figure 6.12 and

Table 6.4. It can be recognized that the method used in all the previous cases (Stokes, Vening Meinesz, etc.) for increasing the thresholding value works only for case (a). For the rest of the cases, case (b), (c), and (d), the degradation in the accuracy is huge

and is far away from the target accuracy, which is one centimetre (Figure 6.13). The main reason for the sudden degradation in the accuracy, which reaches almost half a metre in case (d), is the removal of the main energy of the A matrix. For example, in case (d), all the detail wavelet coefficients of all the decomposition levels are removed and only the approximation coefficients are left.

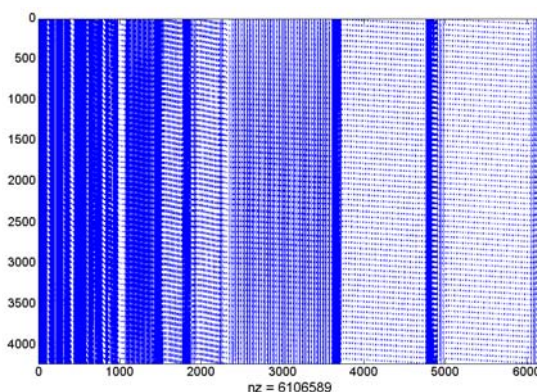


Figure 6.10: Design matrix A of the global fixed thresholding (0.12); each blue spot represents a nonzero value in the vertical component kernel (deflection-geoid)

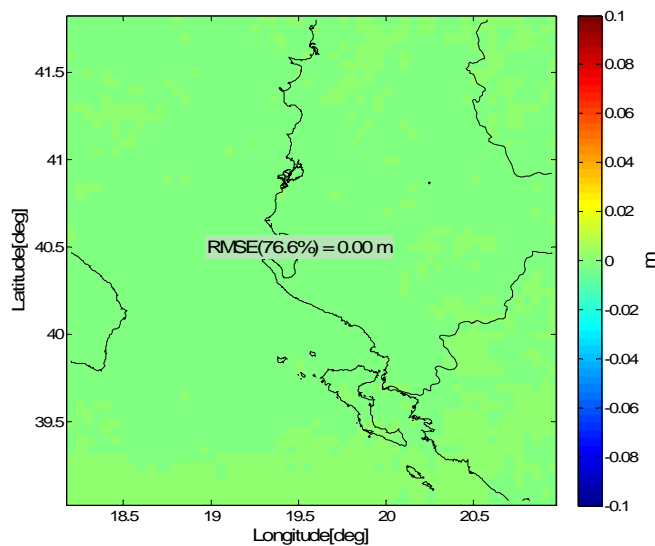


Figure 6.11: Difference between wavelet global fixed solution and numerical integration solution for the deflection-geoid formula

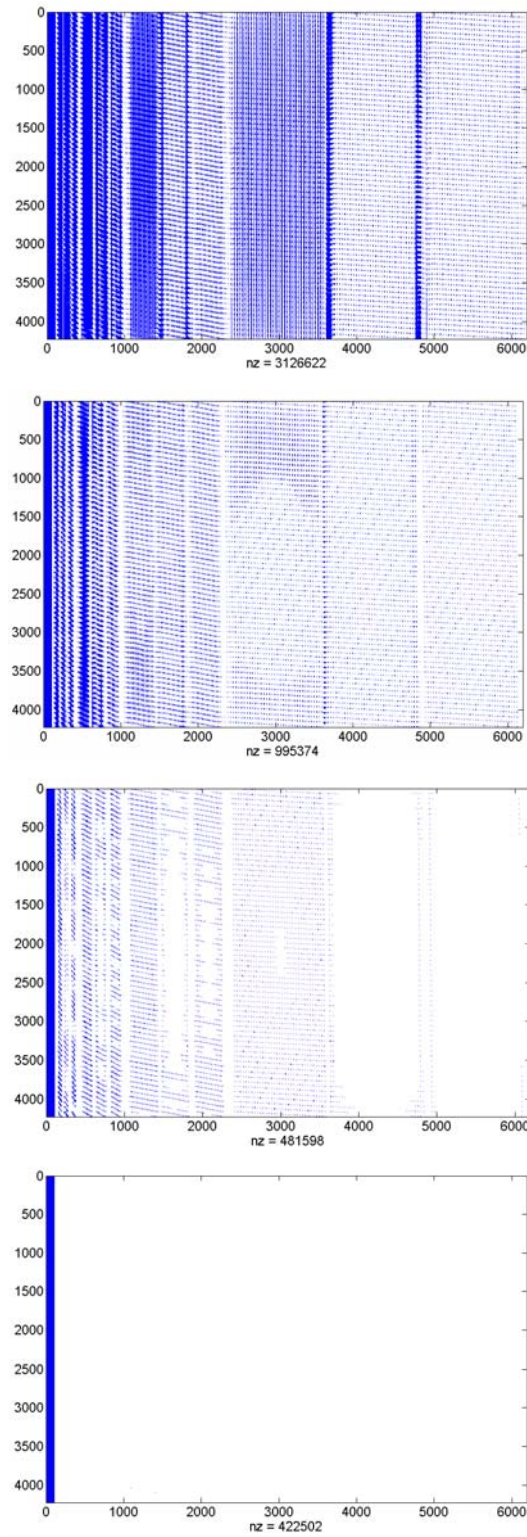


Figure 6.12: A matrix at four different thresholding values (1.23, 12.3, 123.3, and 1233.5); each blue spot represents a nonzero value in the vertical component kernel

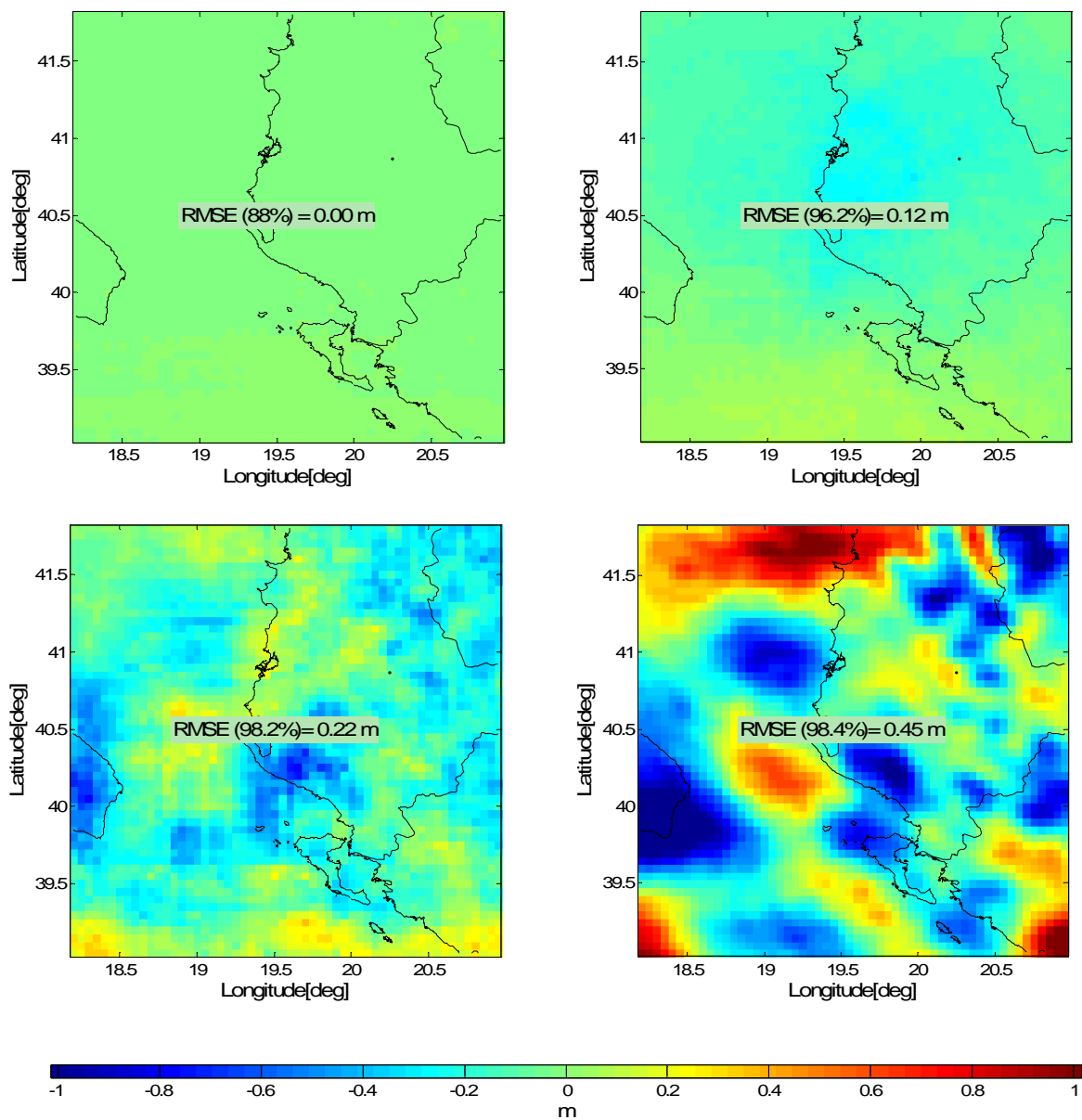


Figure 6.13: The difference between the wavelet global fixed thresholding and numerical integration solutions for the deflection-geoid formula

Table 6.4: Wavelet global fixed thresholding versus wavelet full matrix solution for the deflection-geoid formula

Hard thresholding	Full matrix	Global Eq. (3.41) or (3.42)	(a)	(b)	(c)	(d)
Thresholding value	-	0.12	1.23	12.3	123.3	1233.5
Storage (MB)	372	48.5	26.4	10.4	6.21	5.62
RMSE (m)	-	0.00	0.00	0.12	0.22	0.45
No. of elements	52381550	12213178	6253244	1990748	963196	845004
Comp%	0%	76.6%	88%	96.2%	98.2%	98.4%

6.1.2.3 Level/direction-wise thresholding solution

Four global thresholding cases are introduced in the previous section; cases (b), (c), and (d) require improvement in the accuracy. Global thresholding case (a) requires improvement in the compression level while maintaining an acceptable accuracy (RMSE equal to 1 cm). Two examples are illustrated in this section in detail. For global case (a), the compression level improved by 1% with an acceptable accuracy. The thresholding values combined for this improvement are given in Table 6.5. It is worth mentioning that the values are different from the values introduced in global cases (b), (c), and (d) because it is clear from

Table 6.4 that these values are over threshold and cut part of the main energy of the design matrices A.

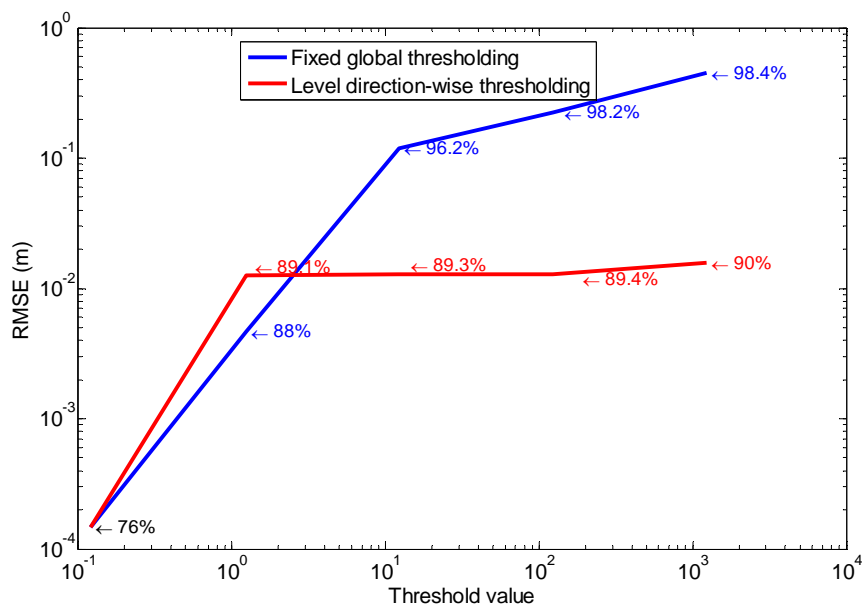
Four thresholding values are implemented for improving global case (d). As seen in Table 6.6, the accuracy improved dramatically from 45 cm to 1.5 cm (96% improvement) with an 8.4% loss in the compression level (from 98.4% to 90%). Consequently, the level/direction-wise approach effectively improved the accuracy with a high compression level. From Figure 6.14, it is seen that the maximum compression level that can be achieved with acceptable accuracy (1 cm) is between 89% and 90%.

Table 6.5: Level/direction-wise for case (a) global thresholding

Level/direction-wise	Horizontal	Diagonal	Vertical
Level 1	2.4	12	2.4
Level 2	1.2	1.2	1.2
Level 3	1.2	1.2	1.2
Level 4	1.2	1.2	1.2
RMSE (m)	0.01		
Comp. %	89.1%		
Storage (MB)	23		

Table 6.6: Level/direction-wise for case (d) global thresholding

Level/direction-wise	Horizontal	Diagonal	Vertical
Level 1	3	12	3
Level 2	1.2	12	1.2
Level 3	1.2	12	1.2
Level 4	1.2	1.2	1.2
RMSE (m)	0.015		
Comp. %	90%		
Storage (MB)	20		

**Figure 6.14: Global fixed thresholding versus level/direction-wise thresholding for the deflection-geoid formula**

6.2 Inversion of geodetic integrals

In the previous sections, inverse geodetic integrals were evaluated. In this section, another approach is introduced for solving inverse geodetic problems. The solution will be through inverting the direct integrals introduced in Chapter Five. The solution is obtained by means of a combination of the two-dimensional wavelet evaluation based on Mallat's algorithm and an optimization procedure. The Stokes and the Poisson integrals are inverted numerically by the combined wavelet-optimization algorithm. This algorithm is combined with the global thresholding technique.

6.2.1 Wavelet inversion of the Stokes integral

The Stokes integral, Equation (2.7), is inverted in the wavelet domain to obtain gravity anomalies from geoid undulations. The same synthetic data shown in Figure 5.1 is reused. The Daubechies wavelet family with four vanishing moments is implemented for the wavelet evaluation. The Stokes integral is inverted in the wavelet domain by the wavelet full matrix approach and global fixed thresholding. The methodology of investigation summarized in Figure 3.12 is used. Finally, the wavelet transform is used as a regularization tool for de-noising stationary and non-stationary noise during the inversion of the Stokes integral.

6.2.1.1 Wavelet full matrix solution

The design matrix A shown in Figure 5.4 is used in the inversion of the Stokes integral. The wavelet full matrix solution has an RMSE equal to 4.03 mGal in comparison to the gravity anomaly reference data (Figure 5.1); see Figure 6.15. The tolerance value used is equal to 1×10^{-6} . The solution converged after 101 iterations with relative residual equal to 9.3×10^{-7} (Table 6.7), but the main problem is the size of the design matrix A (186 MB). The solution CPU time on a PC was approximately 0.21 second.

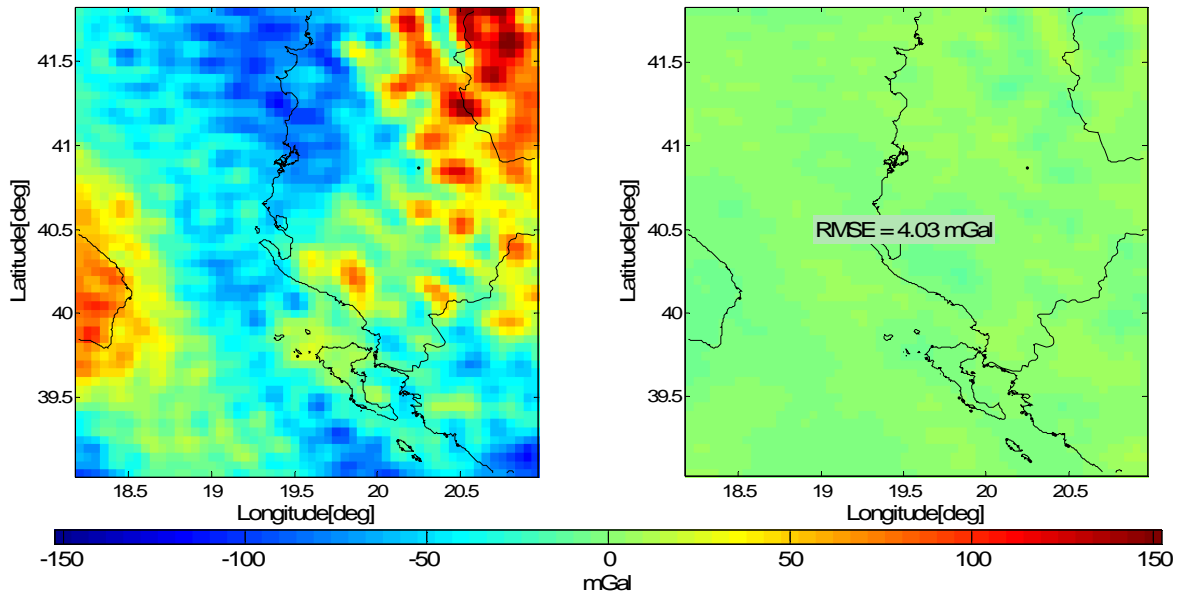


Figure 6.15: Wavelet full matrix solution for the inversion of the Stokes integral (left) and the difference from the reference data (right)

6.2.1.2 Wavelet global fixed thresholding solution

Global hard thresholding is applied to the design matrix. The matrix introduced in Section 5.1.3 and Figure 5.8 is used for the inversion of the Stokes integral. There is no loss of accuracy at a compression level equal to 75% (RMSE of 4.03 mGal) in comparison with the reference data and in comparison to the full matrix solution (RMSE equal to zero mGal); see Figure 6.16.

The same thresholding values introduced in Section 5.1.3 and the corresponding four matrices shown in Figure 5.10 are tested for inverting the Stokes integral with the wavelet–optimization algorithm. As shown in Figure 6.17, the first two solutions (cases (a) and (b)) converged after 102 and 105 number of iterations, respectively. The third solution, case (c), converged but with more iterations (134 iterations) and 8.6×10^{-7} relative residual. The fourth solution diverged and did not reach a solution even after 188 iterations. The four cases are illustrated in Table 6.7. From Table 6.7 and Figure 6.18, it can be seen that cases (c) and (d) do not have acceptable accuracy in comparison to the full matrix case, with 7.7 and 24.72 mGal RMSE, respectively. For case (b) with a 93.5%

compression level, an RMSE of 0.12 mGal is achieved in comparison to the full matrix solution.

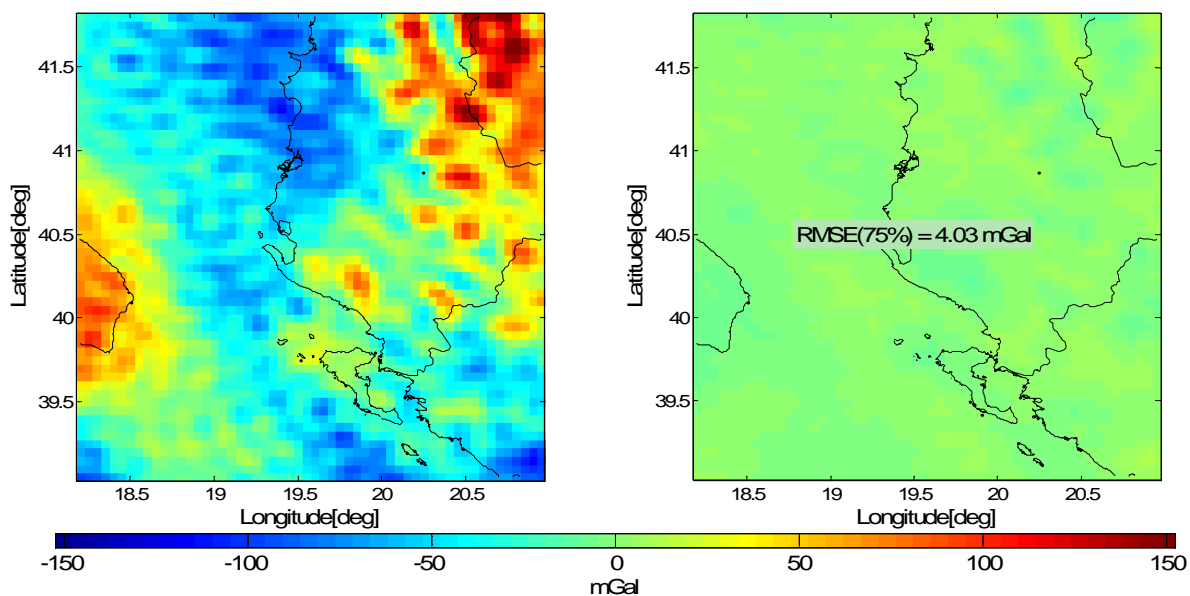


Figure 6.16: Global fixed thresholding wavelet solution (left) and difference from reference data (right) for the inversion of the Stokes integral

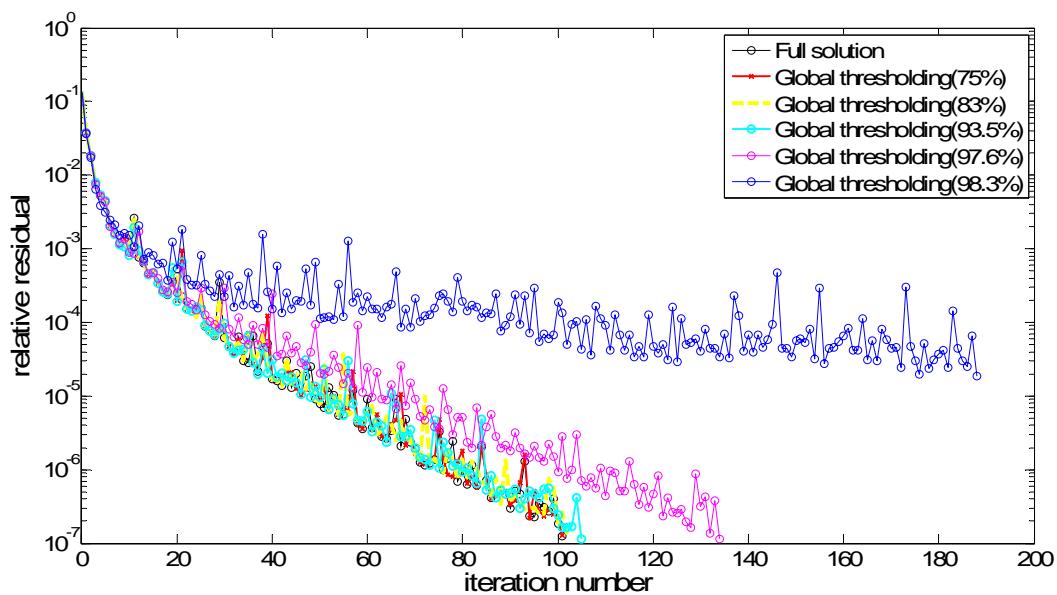


Figure 6.17: Conjugate gradient iterations versus relative residuals (inversion of the Stokes integral)

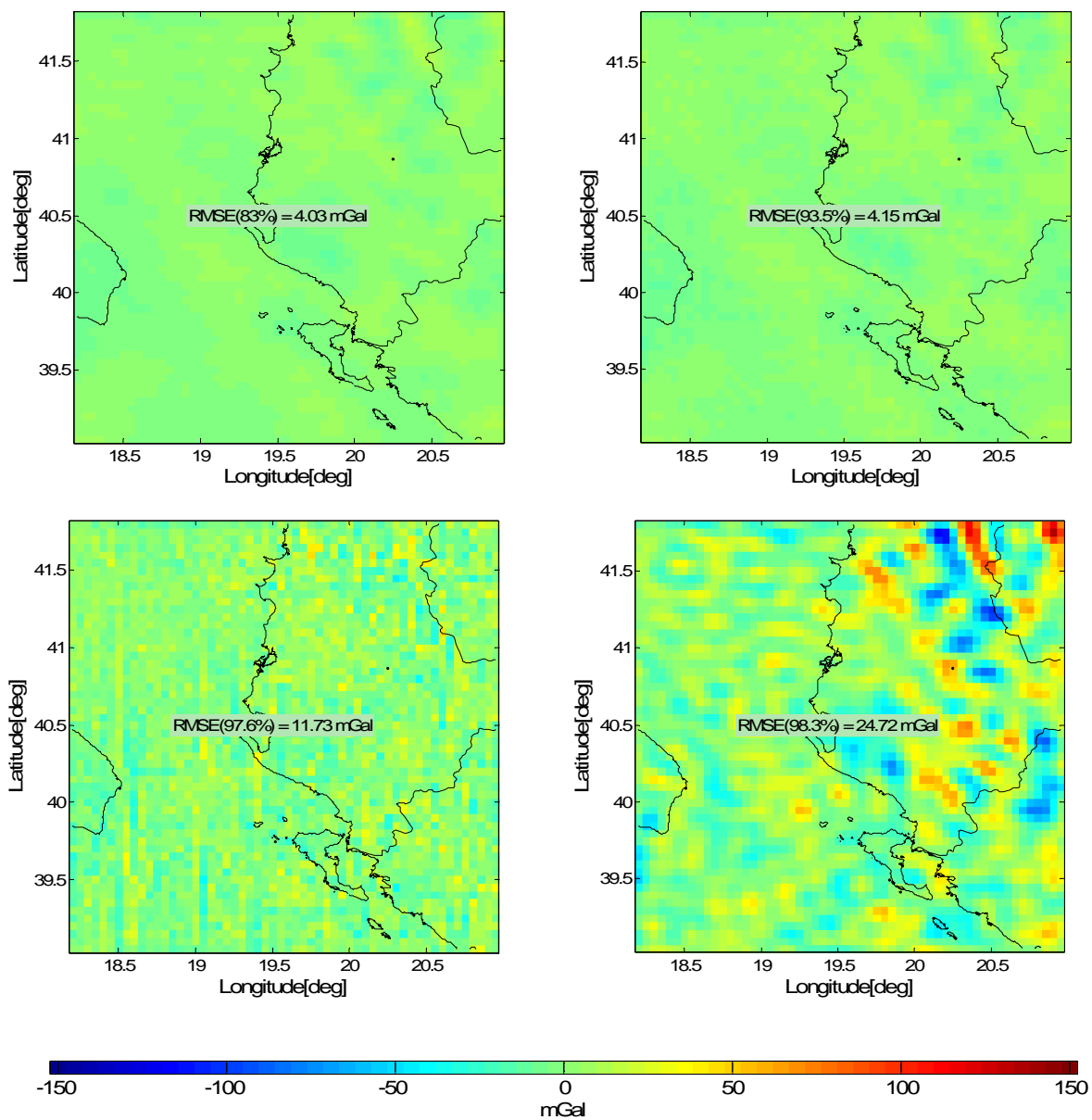


Figure 6.18: The difference between the wavelet global fixed thresholding and reference data for the inversion of the Stokes integral

Table 6.7: Global thresholding versus full matrix solution for the inversion of the Stokes integral

Hard thresholding	Full matrix	Global Eq. (3.41) or (3.42)	(a)	(b)	(c)	(d)
Thresholding value	-	1.5×10^{-7}	1.5×10^{-6}	1.5×10^{-5}	1.5×10^{-4}	1.5×10^{-3}
Storage (MB)	186	50	36	16	8	6
RMS (mGal)	4.03	4.03	4.03	4.15	11.73	24.72
No. of elements	26190775	6506135	4460519	1696296	629575	445852
Comp%	0%	75%	83%	93.5%	97.6%	98.3%
No. of iterations	101	101	102	105	134	188
Relative residual	9.3×10^{-7}	9.3×10^{-7}	9.7×10^{-7}	8.4×10^{-7}	8.6×10^{-7}	1×10^{-4}

6.2.1.3 Wavelet as a regularization tool

The wavelet full matrix solution, Subsection (6.2.1.1), is repeated after adding stationary and non-stationary noise to the geoid undulations. The stationary random noise is simulated with a standard deviation equal to 50 cm as shown in Figure 4.16. The solution is obtained with the contaminated data and is shown in Figure 6.19. It can be recognized that there is a significant degradation in the accuracy of the solution from an RMSE of 4.03 mGal to an RMSE of 290 mGal.

The soft thresholding technique is applied to the contaminated geoid undulations. The RMSE of the recovered geoid undulations is 17 cm in comparison to the clean data (Section 4.4.2). The solution is repeated with the de-noised geoid undulations and a significant improvement in the solution is obtained. The RMSE decreased from 290 mGal to 25 mGal, a 90% improvement. This shows the effectiveness of the soft thresholding technique, Equations (3.43) and (3.44), in handling and de-noising stationary random noise.

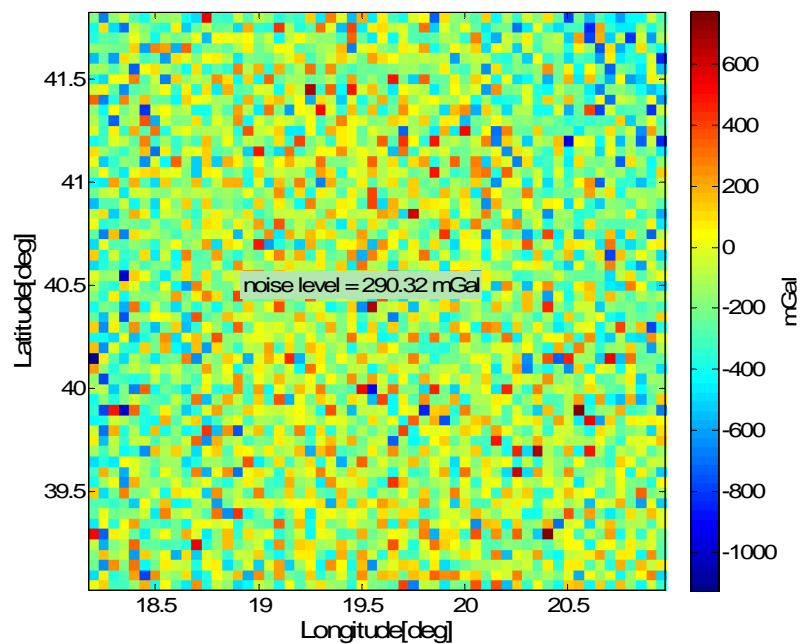


Figure 6.19: Difference between the solution from the noisy geoid undulations (stationary) and the reference data for the inversion of the Stokes integral

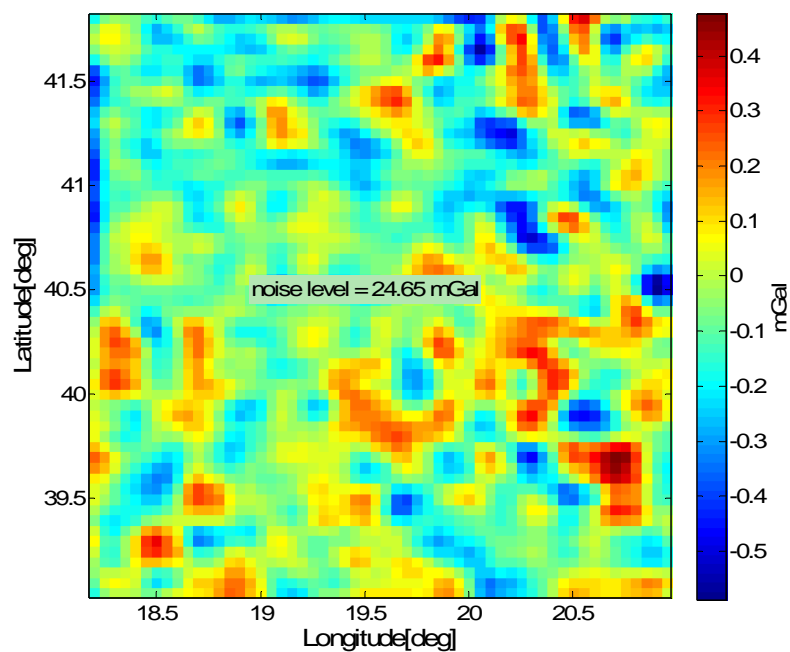


Figure 6.20: Difference between the solution from the de-noised geoid undulations (stationary) and the reference data for the inversion of the Stokes integral

The non-stationary noise is simulated using four different noise levels (± 5 cm, ± 15 cm, ± 35 cm, and ± 55 cm). Each noise level is used for a quarter of the clean undulations matrix. A bias of 10 cm is added to the first noise level and a bias of 5 cm is added to the second. The simulated non-stationary noise and the geoid undulation after the addition of the non-stationary noise are shown in Figure 4.9. With the non-stationary noisy data, a huge degradation occurs in the solution, with an RMSE equal to 221 mGal (Figure 6.21).

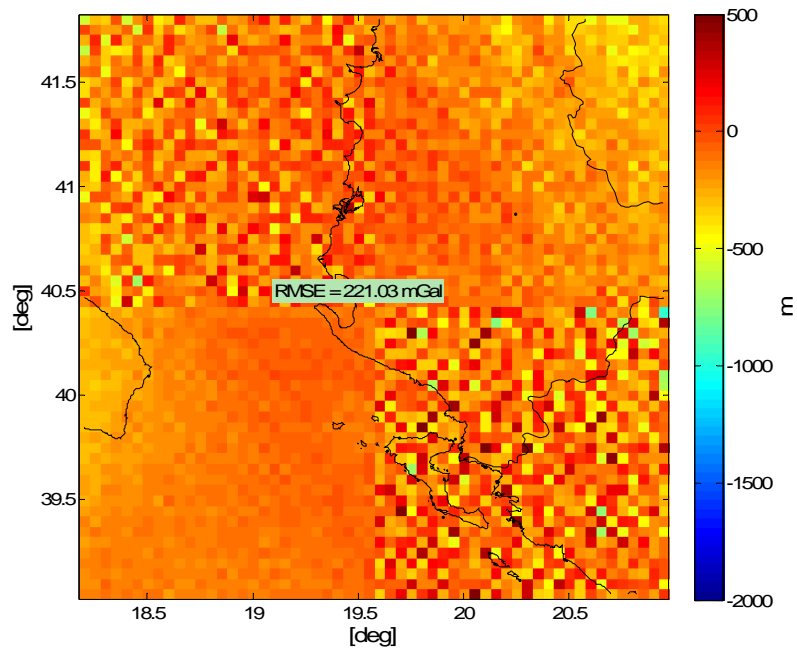


Figure 6.21: Inversion of the Stokes integral with non-stationary noise

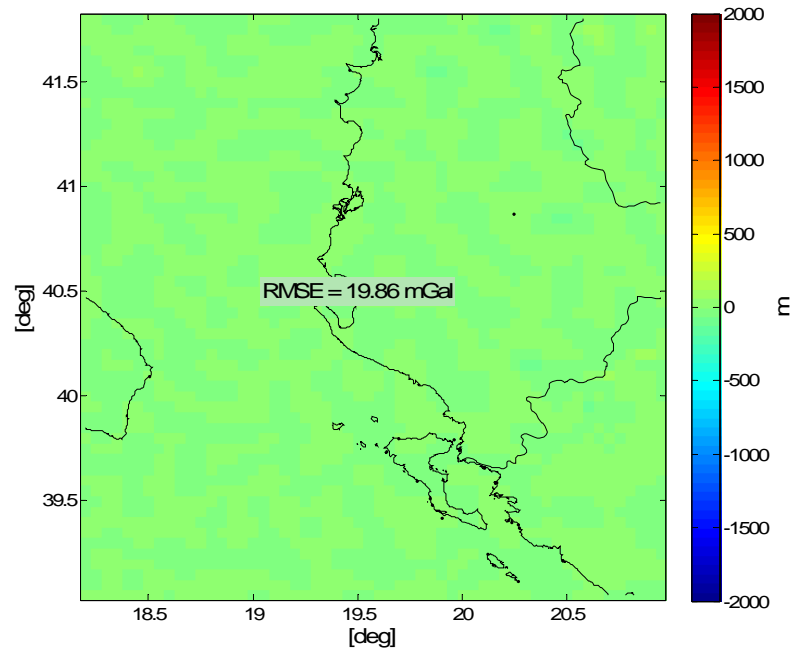


Figure 6.22: Inversion of the Stokes integral after de-noising the non-stationary noise

After applying the wavelet de-noising algorithm, Equations (3.43) and (3.44), the recovered undulations have an RMSE equal to 13 cm (Figure 4.20), and the solution improved to an RMSE equal to 20 mGal (Figure 6.22). The use of the wavelet soft thresholding filtering technique leads to a 90% improvement in the accuracy of the estimated gravity anomalies. This finding proves that the wavelet filtering technique is an efficient regularization method (de-noising) in solving inverse geodetic integrals.

6.2.2 Wavelet inversion of the Poisson's integral (downward continuation)

The Poisson integral in Section 2.2 is used for downward continuation. Equation (2.31) is inverted by the combined optimization-wavelet algorithm introduced in Section 3.5. The same data shown in Section 5.4.1 and Figure 5.28 is used. The data is downward continued from 7288 m to 4370 m altitude.

6.2.2.1 Wavelet full matrix solution

The Poisson integral is inverted numerically with the full matrix without any thresholding. The iteration diverged with a tolerance value equal to 1×10^{-6} . The difference between the diverged solution and the reference data (Figure 5.28) is shown in Figure 6.23.

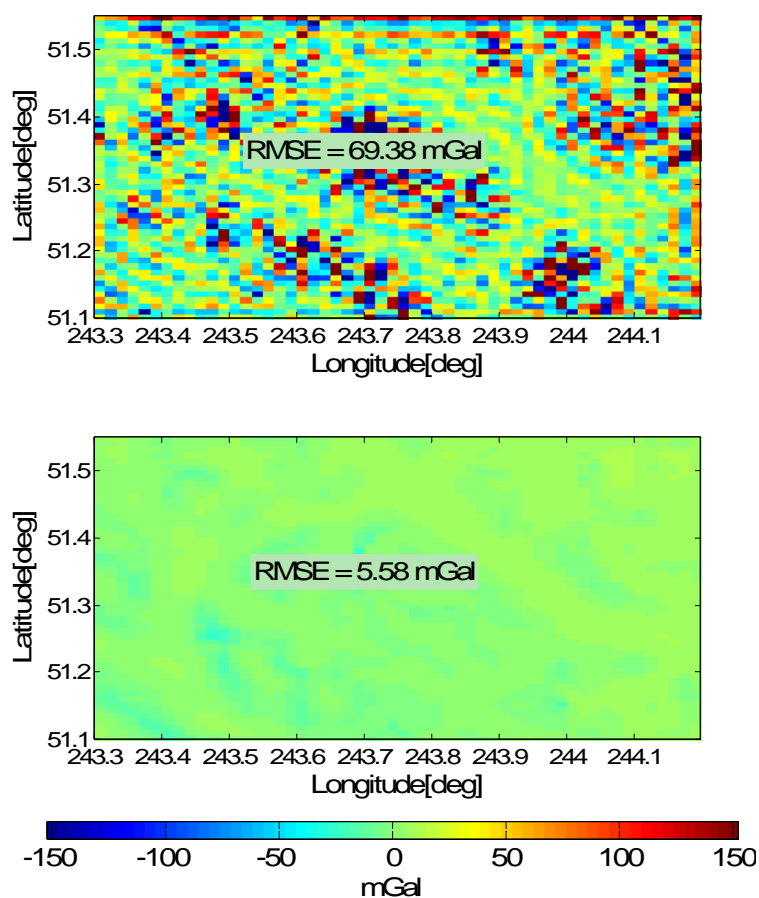


Figure 6.23: The wavelet full matrix inversion of the Poisson integral (downward continuation) before regularization (up) and after regularization (down)

The condition number of the normal matrix was computed for the determination of the instability of the problem and was equal to 7.02×10^{28} , which is huge. The singular value decomposition was done for the normal matrix. The L-curve between the residual and solution norms to determine the regularization parameter to be used in Tikhonov regularization is shown in Figure 6.24 [Hansen, 1998]. The regularization parameter from Figure 6.24 is added to the diagonal of the normal matrix, and the solution is repeated. The solution converged after the regularization with 28 steps. The difference between the regularized wavelet full matrix solution (Figure 6.25) and the reference data was shown in Figure 6.23, with an RMSE equal to 5.58 mGal.

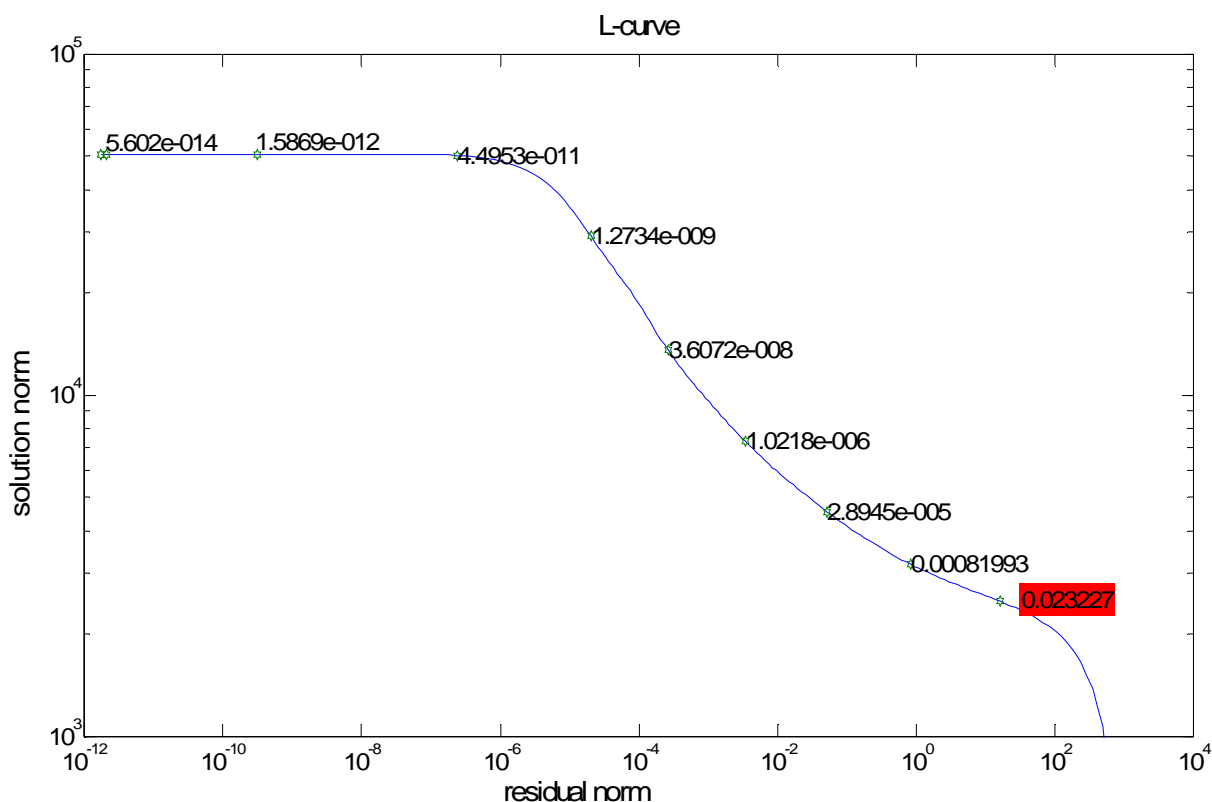


Figure 6.24: L-curve of the normal matrix for the choice of the optimal regularization parameter

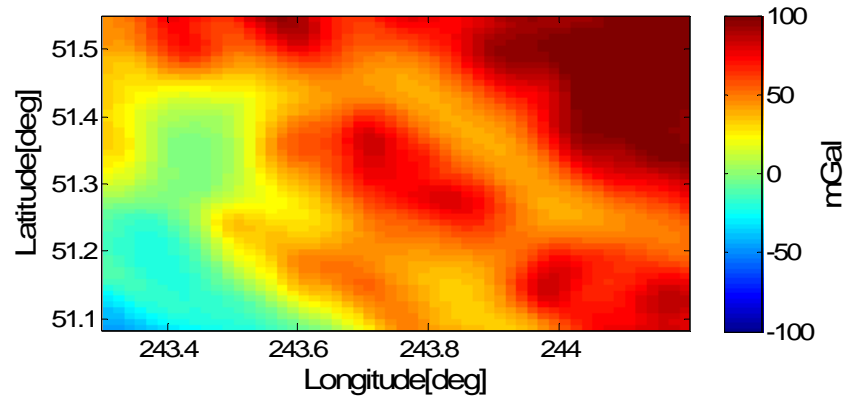


Figure 6.25: Wavelet full matrix regularized solution for the downward continuation operator

6.2.2.2 Wavelet global fixed thresholding solution

The design matrix shown in Figure 5.32 is used in the inversion of the Poisson integral. With a 76% compression level, there is almost no loss in accuracy in comparison to the full matrix regularized solution (same RMSE of 5.58 mGal); see Figure 6.26.

The four global thresholding values with their corresponding matrices shown in Figure 5.34 are used for the inversion of the Poisson integral (downward continuation). The four cases converged after 28 iterations with a tolerance value equal to 1×10^{-6} (Figure 6.27). The same regularization parameter was used in the four cases. The four solutions converged with RMSE 0.001, 0.01, 0.11, and 0.37 mGal for 79.9%, 89.7%, 94.5%, and 97%, respectively; see Figure 6.28 and Table 6.8. The target accuracy is 0.1 mGal and this is satisfied by cases (a), (b) and (c). For case (d), a sudden degradation in the accuracy occurred to 0.37 mGal. In contrast to the inversion of the Stokes integral case (d), Table 6.7, the downward continuation case (d) converged, which could be related to the regularization parameter used in this case.

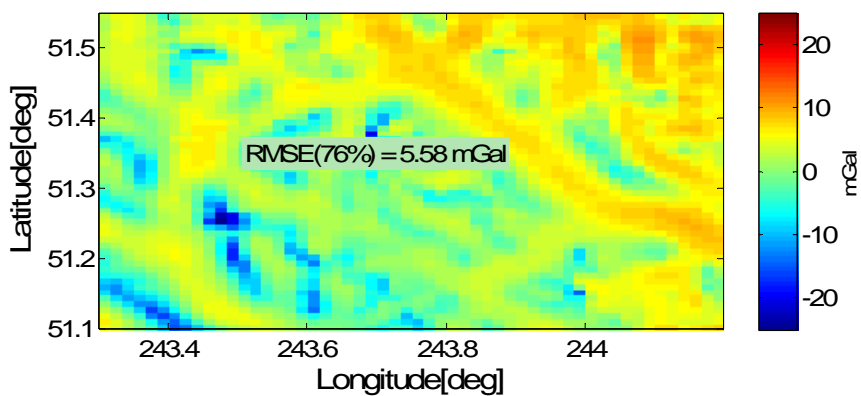


Figure 6.26: Difference between regularized global fixed solution and reference data for the downward continuation operator

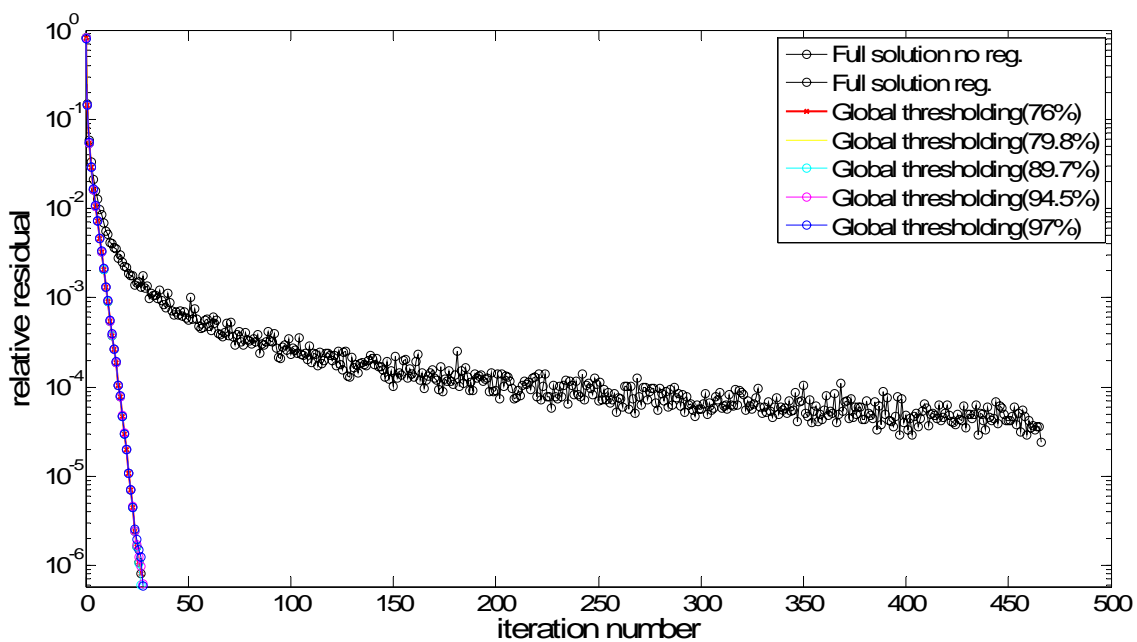


Figure 6.27: conjugate gradient iterations versus relative residuals for the inversion of Poisson integral (downward continuation)

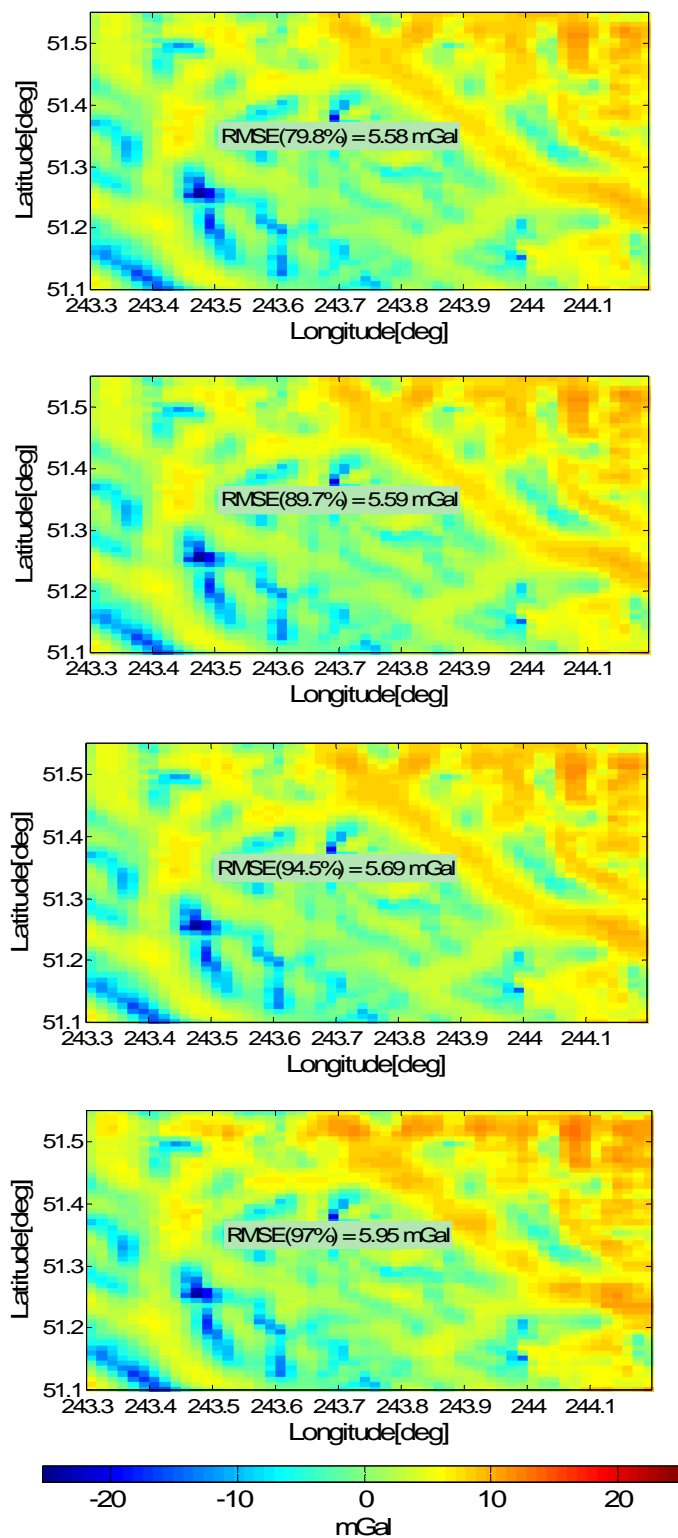


Figure 6.28 The difference between the regularized wavelet global fixed thresholding solutions and reference data for the downward continuation operator

Table 6.8: Wavelet global fixed thresholding versus wavelet full matrix solution for the evaluation of the downward continuation operator

Hard thresholding	Full matrix	Global Eq. (3.41) or (3.42)	(a)	(b)	(c)	(d)
Thresholding value	-	6.3×10^{-8}	6.3×10^{-7}	6.3×10^{-6}	6.3×10^{-5}	6.3×10^{-4}
Storage (MB)	186	72.6	60.41	30.94	16.5	9.14
RMSE (mGal)	-	0.000	0.001	0.01	0.11	0.37
No. of elements	26190775	6349099	5276895	2702207	1441172	797085
Comp%	0%	76%	79.8%	89.7%	94.5%	97%
No. of iterations	27	27	28	28	28	28
Relative residual	9.9×10^{-7}	9.9×10^{-7}	6.7×10^{-7}	7.5×10^{-7}	7.7×10^{-7}	7.2×10^{-7}

6.3 Summary

In this chapter, the inverse geodetic problems were evaluated by the two-dimensional wavelet transform algorithm. They were formulated in two different ways: first, as direct geodetic integrals, such as the inverse Vening Meinesz and the deflection-geoid formula; and, second, as the numerical inversion of the Stokes integral and the Poisson integral (downward continuation).

In the case of the inverse Vening Meinesz and the deflection-geoid formula, three wavelet transform implementations were introduced: the wavelet full matrix approach, wavelet global fixed thresholding, and level/direction-wise thresholding. The wavelet full matrix approach achieved identical results to the FFT and numerical integration. The automated thresholding approach reached a 76% compression level in both cases, with no loss in accuracy in comparison to the numerical integration solution. The level/direction-wise thresholding achieved very high compression levels with an acceptable accuracy in both cases. The inverse Vening Meinesz reached a 94% compression level with 0.12

mGal RMSE. In the case of the deflection-geoid formula, 90% were achieved with 0.015 m RMS accuracy.

The new wavelet two-dimensional representation of the geodetic operators introduced in this thesis was combined with the conjugate gradient method for the inversion of the integrals. The Stokes and the Poisson integrals were numerically inverted by this combined wavelet-optimization algorithm. The main drawback of this approach is that it requires a large computer memory.

The Stokes integral was inverted successfully with the wavelet full design matrix with an RMSE 4.03 mGal for the difference from the reference data. A compression level of 93.5% is achieved by the global fixed thresholding with RMSE equal to 0.13 mGal in comparison to the full matrix solution. Simulated noise was used to contaminate the geoid undulations. For this case study, the use of wavelet de-noising led to a 90% improvement in the accuracy of the estimated gravity anomalies.

The inversion of the Poisson integral failed: because the ill-condition of the normal matrix, the conjugate gradient solution diverged. A regularization parameter was determined from the L-curve of the normal matrix and was added to the diagonal of the normal matrix (Tikhonov regularization). The solution successfully converged with the regularized full matrix and reached a solution with RMSE equal to 5.5 mGal in comparison to the reference data. The global fixed thresholding algorithm achieved 0.11 RMSE with a 94.5% compression level in comparison to the full matrix solution.

The main findings of this chapter led to the following outcomes:

- The success of the new wavelet transform algorithm to achieve high compression levels with an acceptable accuracy in the inversion of geodetic integrals that have different data sets, different grid sizes, and spacing verifies its effectiveness in the inversion of geodetic integrals in planar approximation.
- The level/direction-wise thresholding method is very useful for geodetic operators with two integrals, such as the deflection-geoid formula and the inverse Vening Meinesz integral, because it decreases the computer

memory and storage required for allocating the design matrices significantly, which helps in the simple implementation of these types of operators on simple PC's.

- The power of wavelets to localize different features with different properties in the frequency domain and in the spatial domain, allows the effective determination of noisy data with different properties and noise levels. Consequently, this determination will help in more efficient handling and de-noising of these types of data with non-stationarity noise. These findings will open the door for using this wavelet technique in a number of applications with a very high non-stationarity environment, such as airborne gravimetry and satellite altimetry.

Chapter Seven: Conclusions and recommendations

New developments in the application of the two-dimensional wavelet transform for the evaluation of geodetic operators have been presented. Eight geodetic operators have been evaluated by the wavelet algorithm. The algorithm accuracy is numerically identical to the well-established fast Fourier transform and the numerical integration. The main drawbacks of the algorithm, which are the size of the matrices and the memory required, are overcome by an automated adaptive thresholding algorithm. The localization and de-noising properties of the wavelet transform have been used efficiently as regularization tools for the inversion of geodetic integrals.

7.1 Summary

In this thesis, eight geodetic operators have been evaluated using the new wavelet algorithm implemented. The results obtained are summarized below:

- The Stokes integral with the wavelet full matrix solution achieved identical results to the FFT and numerical integration. The target accuracy for this application was 1 cm. The modified fixed global thresholding achieved a 93.5% compression level with an acceptable accuracy of 6 mm, with a 1.5×10^{-5} thresholding value. The level/direction-wise thresholding technique improved the compression level to 95.2% with an RMSE equal to 1.3 cm.
- The Vening Meinesz integral with the full matrix solution also achieved identical results as FFT and numerical integration. The global fixed thresholding yielded a 95.5% compression with a 0.07 arc-second RMSE. The level/direction-wise increased the compression level by an extra 1% with no loss in the accuracy.
- The terrain correction integral wavelet solution was the same as the numerical integration and FFT. The target accuracy for this application was 0.1 mGal. A 93% compression level was reached by global fixed

thresholding with an RMSE of 0.13 mGal. The level/direction-wise approach optimized the compression level and the accuracy to 92.7% and 0.09 mGal, respectively.

- The upward continuation integral evaluation gave similar results to the FFT and the numerical integration algorithm. The target accuracy for this application was 0.1 mGal. In the case of global fixed thresholding, 94.5% compression was achieved with an RMSE of 0.09 mGal. The level/direction-wise thresholding increased the compression level by 1.2% with an RMSE equal to 0.18 mGal.
- The inverse geodetic operators were treated in two different ways. The inverse Vening Meinesz and deflection-geoid were treated as geodetic integrals. The inversions of the Stokes and Poisson integrals (downward continuation) were done numerically by combining the new wavelet algorithm implemented and the iterative conjugate gradient method.
- The inverse Vening Meinesz evaluated with the full matrix solution achieved identical accuracies to the FFT and the numerical integration solution. The global fixed thresholding reached a 94.4% compression level with an RMSE of 0.14 mGal. The level/direction-wise modification improved the accuracy by 80% at high compression levels.
- The deflection-geoid formula evaluation done by the wavelet full matrix had the same accuracy as FFT and numerical integration. An 88% compression was achieved with no loss of accuracy. The level/direction-wise thresholding improved the compression level by an additional 2%, with an RMSE of 1.5 cm.
- The Stokes' integral was inverted successfully using the full wavelet matrix without regularization. The solution achieved an RMSE of 4.03 mGal in comparison to the reference data. The solution with the conjugate gradient method converged after 101 iterations. The global

thresholding approach achieved a 93.5% compression level with 0.12 mGal loss in accuracy in comparison to the full matrix solution.

- The Poisson integral was inverted numerically. The solution diverged by using the wavelet full matrix approach. Tikhonov regularization was used, and the regularization parameter was chosen from the L-curve. The conjugate gradient method converged to the solution after 28 iterations with an RMS accuracy equal to 5.5 mGal in comparison to the reference data. The global fixed thresholding led to a 94.5% compression level with 0.1 mGal loss in the accuracy in comparison to the full matrix solution.

7.2 Conclusions

A new implementation of two-dimensional wavelet transform for the evaluation of geodetic operators was developed. The five main accomplishments of this thesis can be summarized as follows:

1. The direct and inverse geodetic integrals (Stokes, Vening Meinesz, upward continuation, terrain correction, inverse Vening Meinesz, and deflection-geoid formula) were efficiently evaluated by the new wavelet algorithm with an accuracy identical to the FFT and numerical integration solutions. The new wavelet algorithm requires a 30% less computational effort in comparison to the standard wavelet algorithm, because the step of inverse wavelet transform is done implicitly.
2. A new combined wavelet-optimization technique is used for the inversion of geodetic integrals. Two integrals (Stokes and Poisson) were successfully inverted with an acceptable practical accuracy in comparison to reference data.
3. Two new thresholding techniques, global fixed and level/direction-wise thresholding, were successfully applied and high compression levels of the matrices were achieved for the eight operators with no loss of accuracy.

4. Efficient filtering of stationary and non-stationary noise was implemented, with a 90% improvement in the inverse solutions accuracy.
5. The thresholding value was estimated automatically from the set of equations introduced in this thesis for both compression and de-noising applications.

As a general conclusion, the new wavelet algorithm developed in this thesis is an efficient algorithm for the evaluation of different geodetic operators with high accuracy, de-noising efficiency, and reduced computational effort. More detailed conclusions are summarized in the following paragraphs.

The thresholding value for Stokes-type kernels (direct and inverse) and the deflection-geoid formula are 1×10^{-4} ; the direct and inverse Vening Meinesz integrals are 1×10^{-6} ; for the terrain correction, upward and downward continuation are 1×10^{-8} .

The corresponding compression levels are in the range of 78% to 84% with no loss in accuracy depending on the operator. This finding shows that the hard thresholding technique is adaptive to the rate of decay of the kernel to zero.

Two modifications were successfully implemented for the compression of the wavelet transform algorithm design matrices. In some cases, the first modification (global fixed thresholding) achieved a 90% compression with high accuracies. The second modification (level/direction-wise) successfully reached compression levels in the range of 90% to 95% with no loss in accuracy depending on the operator. It can be concluded that these two modifications achieved maximum compression levels with an accepted accuracy.

In the case study tested in this thesis, the soft thresholding de-noising technique can be successfully applied to filtering of stationary and non-stationary noise. The de-noising technique removed 60% of the data noise in both cases. This technique efficiently improved the solution of the inverted Stokes integral by 90%.

As final conclusions, the wavelet transform algorithm will be efficient in handling geodetic problems with non-stationary environments. These types of problems will benefit from the analysis and de-noising effectiveness of the wavelet algorithm.

Examples of these applications are airborne gravimetry and satellite altimetry. Also, the new, efficiently developed wavelet representation algorithm of geodetic operators implemented and evaluated in this study will open the door for more applications and studies in the use of the wavelet transform in different geodetic problems.

7.3 Recommendations and open problems

The following is a list of some of the areas requiring future work and further investigation:

- A small edge effect was detected in the wavelet solution of the geodetic integrals. This effect was amplified in the case of the inversion of these integrals. It was minimized by the application of zero padding, but further investigation is required to identify its cause and propose a way for treating it.
- The Daubechies wavelet family was used in this study. The choice of this family relied on suggestions from the author's experience, other studies, and the wavelet literature. It is recommended to test other orthogonal wavelets, especially since there are a large number of wavelet families available.
- Although the thresholding value is automatically estimated in both the compression and de-noising cases, the decision on the number of levels of decomposition was made through trial and error. It will be very beneficial if further studies develop techniques to automate the estimation of the number of levels of decomposition.
- Other thresholding techniques, such as penalized thresholding [Birge and Massart, 1997], should be tested for de-noising in order to improve the extraction of the signal from noise, more than the 60% achieved here.
- The regularization method and the parameter estimation technique used for the stabilization of the inverse problems require more investigation

to ensure the choice of the most suitable method and optimal parameter, such as using the probabilistic method [Rauhut, 1992].

- The wavelet algorithm introduced in this thesis requires modifications for its application on irregular grids and testing non-stationary kernels and their effects; an example is the use of second generation wavelets [Soltanpour et al., 2006].

The introduced wavelet representations of different geodetic operators are in planar approximation. Further research is required for the implementation of the new wavelet algorithm on a sphere suitable for the representation of different geodetic operators. The main problem in this implementation is performing the convolution on a sphere. The following three methods are suggested for doing future research on this problem:

- Gridding the data on an equidistant grid on the sphere in the local area of interest [Freedon et al., 1998].
- Combining the wavelet algorithm with a least-squares procedure for the estimation of the wavelet coefficients point-wise [Schmidt et al., 2005].
- The combination of numerical integration in the meridian direction and wavelet transform in the parallel direction for the wavelet evaluation of the different geodetic operators on a sphere.

Given the current state of technology of the new LEO missions dedicated to gravity field research, there is a new era in geodetic research offering many challenges and promising applications. The implementation of spherical wavelets and an efficient multi-resolution analysis with orthogonal properties and a fast computational scheme will produce computational tools for many applications, such as monitoring temporal variations of numerous global geophysical signals all over the globe. For example, the multi-resolution analysis of monthly gravitational field models derived from GRACE satellite observations provide temporal variations, such as from hydrological effects that can be observed clearly in certain wavelet scales [Fengler et al., 2006]. Therefore, temporal gravity field modeling, at scales from local to global, could benefit by the

analysis, de-noising, localization, and evaluation capabilities provided by wavelet-based methods both on the plane and sphere.

References

Barrett R., M. Berry, T. F. Chan, J. Demmel, J. Donato, J. Dongana, V. Eijkhout, R. Pozo, C. Romine, and H. van der Vorst (1994). *Templates for the solution of linear systems: building blocks for iterative methods*. Society for Industrial and Applied Mathematics (SIAM), Philadelphia, Pennsylvania.

Barthelmes F., L. Ballani, and R. Klees (1994). On the application of wavelets in geodesy. In: *Geodetic Theory Today*, convened and ed. by Sansò, F., Springer-Verlag Berlin, Heidelberg (International Association of Geodesy Symposia 114, L'Aquila, Italy, May 30 - June 3), pp. 394-403.

Beylkin G. (1992). On the representation of operators in bases of compactly supported wavelets. *SIAM Journal on Numerical Analysis*, 29(6), pp.1716–1740.

Beylkin G., R. Coifman, and V. Rokhlin (1991). Fast wavelet transforms and numerical algorithms I., *Communications in Pure and Applied Mathematics*, 44, pp.141-183.

Birge L., and P. Massart (1997). From model selection to adaptive estimation. In *Festschrift for L. Le Cam*, D. Pollard, Editor, Springer, New York, pp. 55–88.

Bláha T., M. Hirsch, W. Keller, and M. Scheinert (1996). Application of a spherical FFT approach in airborne gravimetry. *Journal of Geodesy* 70, pp. 663-672, Springer-Verlag.

Bracewell R. (1986). *The Fourier transform and its applications*. Second edition. McGraw-Hill, New York.

Brigham E. O. (1988). *The fast Fourier transform and its applications*. Prentice Hall, Upper Saddle River, New Jersey, USA.NJ, USA.

Chan Y. T. (1995). *Wavelet basics*. Kluwer Academic, Dordrecht.

Chui C. K., L. Montefuscoand, and L. Puccio (1994). *Wavelets: theory, algorithms, and applications*. *Wavelet analysis and its applications*, Vol. 5, Academic Press, INC.

Chui C. K. (1992). *An introduction to wavelets*, Academic Press, San Diego, CA.

Daubechies I. (1992). *Ten lectures on wavelets*. Society for Industrial and Applied Mathematics (SIAM), Philadelphia, Pennsylvania.

Daubechies I. (1990). The wavelet transform, time-frequency localization and signal analysis. *IEEE Transaction on Information Theory*, 36(5), pp. 961-1005.

Daubechies I. (1988). Orthonormal bases of compactly supported wavelets. *Communications in Pure and Applied Mathematics*, 41, pp. 909-996.

Donoho D.L. (1995). De-noising by soft-thresholding. *IEEE Transaction on Information Theory*, 41, 3, pp. 613-627.

Donoho D. L. and I. M. Johnstone (1994). Ideal spatial adaptation via wavelet shrinkage, *Biometrika*, 81, pp. 425-455.

Donoho D. L. and I. M. Johnstone (1998). Minimax estimation via wavelet shrinkage. *The Annals of Statistics*, 26, pp.879-921.

Elhabiby M. and M.G. Sideris (2006a). Wavelet thresholding technique for local geoid and deflection determination in planar approximation. Accepted in *Geophysical Journal International*, 31 pages, September, 2006.

Elhabiby M. and M. G. Sideris (2006b). On the potential of wavelets for filtering and thresholding airborne gravity data. *Newton's Bulletin of the International Gravity Field Service*, No.3, section 1.

Fengler J., W. Freeden, A. Kohlhaas, V. Michel, and T. Peters (2006). Wavelet modeling of regional and temporal variations of the earth's gravitational potential observed by grace. *Journal of Geodesy*, doi: 10.1007/s00190-006-0040-1.

Forsberg R. (2002). Downward continuation of airborne gravity. 3rd Meeting of the International Gravity and Geoid Commission Gravity and Geoid 2002 proceedings.

Forsberg R. (1985). Gravity field terrain effect computations by FFT. *Bulletin géodésique*, 59, pp. 342-360.

Freeden W. (1999). Multiscale modeling of spaceborne geodata. European Consortium for Mathematics in Industry. B.G. Teubner Stuttgart. Leipzig, Germany.

Freeden W., T. Gerven, and M. Schreiner (1998). Constructive approximation on the sphere (with application to geomathematics). Oxford Science Publications, Clarendon.

Gao H. Y. (1997). Choice of thresholds for wavelet shrinkage estimate of the spectrum. *Journal of Time Series Analysis*, 18, pp. 231-251.

Gilbert A. and W. Keller (2000). Deconvolution with wavelets and vaguelettes. *Journal of Geodesy*, 74 (3-4), pp. 306-320.

Glennie C. (1999). An analysis of an airborne gravity by strapdown INS/GPS. Ph.D. Thesis, UCGE Report #20125, Department of Geomatics Engineering, University of Calgary, Calgary, Canada.

Glennie C. and K. P. Schwarz (1997). Airborne gravity by strapdown INS/DGPS in a 100 km by 100 km Area of the Rocky Mountains. In: Proceedings of International Symposium on Kinematic Systems in Geodesy, Geomatics and Navigation (KIS97), Banff Canada, June 3-6, pp. 619-624.

Griffiths D., D. Higham, and A. Watson (1997). The search for a good basis. Proceedings of the 17th Dundee Biennial Conference, June 24-27, Addison Wesley Longman.

Goswami J. C. and A. K. Chan (1999). Fundamentals of wavelets: Theory, algorithms, and applications. Wiley series in microwave and optical engineering, Wiley-Interscience, New York, USA.

Haagmans R., E. de Min, and Martin van Gelderen (1993). Fast evaluation of convolution integrals on the sphere using 1D FFT, and a comparison with existing methods for Stokes' integral. *Manuscripta geodaetica*, 18, pp. 227-241.

Hansen P. C. (1998). Rank-deficient and discrete ill-posed problems: Numerical Aspects of Linear Inversion. SIAM, Philadelphia.

Harris F. J. (1978). On the use of windows for harmonic analysis with the discrete Fourier transform. *Proceedings of the IEEE*, 66, No. 1, pp. 51-83.

Heil C. E. and D. F. Walnut (1989). Continuous and discrete wavelet transforms. *Society for Industrial and Applied Mathematics (SIAM) Review*, 31(4), pp. 628-666.

Heiskanen W. A. and H. Mortiz (1967). *Physical geodesy*. W. H. Freeman and Company, San Francisco.

Hwang C., H.-Y. Hsu and R.-J. Jang (2002). Global mean sea surface and marine gravity anomaly from multi-satellite altimetry: applications of deflection-geoid and inverse Vening Meinesz. *Journal of Geodesy*, 76, pp.407-418, Springer-Verlag

Hwang C. (1998). Inverse Vening Meinesz formula and deflection-geoid formula: application to prediction of gravity and geoid determination over South China Sea. *Journal of Geodesy*, 72, pp.113-130.

Keller W. (2004). *Wavelets in geodesy and geodynamics*. Walter de Gruyter.

Keller W. (2002). A wavelet approach for the construction of multi-grid solvers for large linear systems. In: Adam, J., K. P. Schwarz (eds.), pp. 265-271.

Keller W (1995). Harmonic downward continuation using a Haar wavelet Frame. XXI General Assembly of IUGG, Boulder, Colorado, USA.

Li Y. C. (1993). Optimized spectral geoid determination. UCGE Rep 20050. M.Sc. thesis, Department of Geomatics Engineering, University of Calgary, Canada.

Liu Q. and M. G. Sideris (2003). Wavelet evaluation of the Stokes and Vening Meinesz integrals. *Journal of Geodesy* 77, pp.345-356, Springer-Verlag.

Liu Q. W., Y. Cai Li, and M. G. Sideris (1997). Evaluation of deflections of the vertical on the sphere and the plane: a comparison of FFT techniques. *Journal of Geodesy*, 71, pp.461-468, Springer-Verlag.

Mallat S. (1998). *A wavelet tour of signal processing*. Academic Press, New York, USA.

Mallat S. (1989). A theory for multi-resolution signal decomposition: the wavelet representation. *IEEE Transactions on Pattern Analysis and Machine Intelligence*, 11(7), pp. 674-693.

Meissl P. (1971). A study of covariance functions related to the earth's disturbing potential. Rep no 151, Department of Geodetic Science and Surveying, Ohio State University, Columbus.

Meyer Y. (1992). *Wavelets and operators*. Cambridge University Press.

Moritz H. (1980). *Advanced physical geodesy*. H. Wichmann Verlag, Karlsruhe.

Nawab S. H. and T. F. Quatieri (1988). Short time Fourier transform advanced topics in signal processing. Lim, J.S. and Oppenheim, A.V. Eds, Prentice Hall, pp. 289-337.

Novák P., P. Vaníček, M. Véronneau, S. Holmes, W. Featherstone (2001). On the accuracy of modified Stokes's integration in high-frequency gravimetric geoid determination. *Journal of Geodesy*, 17, pp. 644-654, Springer-Verlag.

Ogden R. T. (1997). *Essential wavelets for statistical applications and data analysis*, Birkhäuser, Boston, USA.

Osman A. (2003). *Transmission lines protection technique based on wavelet transform*. PhD thesis submitted to the faculty of the Graduate Studies, Department of Electrical and Computer Engineering, University of Calgary.

Rauhut A. C. (1992). *Regularization methods for the solution of the inverse Stokes problem*. UCGE reports, No. 20045, PhD thesis, Department of Geomatics Engineering, University of Calgary.

Robertson D. C., O. I. Camps, J. S. Mayer and W. B. Gish (1996). Wavelets and electromagnetic power system transients. *IEEE Transactions on Power Delivery*, 11, No. 2, April, pp. 1050-1056.

Salamonowicz R. H. (2000). A wavelet based gravity model with an application to the evaluation of Stokes' integral. *Gravity, Geoid and Geodynamics 2000* (M. G. Sideris, ed.), IAG Symposium, 123, Springer, Berlin etc., pp. 85-90.

Sandwell D. T. and W. H. F. Smith (1997). Marine gravity anomaly from Geosat and ERS 1 satellite altimetry. *Journal of Geophysical Research*, 102: B5, pp. 10,039-10,054.

Schaffrin B., R. Mautz, C. Shum and H. Tseng (2003). Toward a spherical pseudo-wavelet basis for geodetic applications. *Computer-Aided Civil and Infrastructure Engineering*, 18, pp. 369-378.

Schmidt M., S.-C. Han, J. Kusche, L. Sanchez, and C. K. Shum (2006). Regional high-resolution spatiotemporal gravity modeling from GRACE data using spherical wavelets. *Geophysical Research Letters*, 33, L08403, doi:10.1029/2005GL025509.

Schmidt M., O. Fabert, and C.K. Shum (2005). On the estimation of a multi-resolution representation of the gravity field based on spherical harmonics and wavelets. *Journal of geodynamics*, 39, 5, pp. 512-526.

Schwarz K. P. and N. El-Sheimy (1998-2002): KINGSPAD (KINematic Geodetic System for Positions and Attitude Determination) Software. Geomatics Engineering Department, University of Calgary, Calgary, Alberta, Canada.

Schwarz K. P., M. G. Sideris, and R. Forsberg (1990). The use of FFT techniques in physical geodesy. *Geophysical Journal International*, 100, pp. 485-514.

Sideris M. G. (2005). Geoid determination by FFT techniques. Lecture notes, International School for the determination and use of the geoid, Budapest, Hungary, Jan. 31-Feb. 4.

Sideris M. G. and YC. Li (1993). Gravity field convolutions without windowing and edge effects. *Bulletin Géodésique*, 67, pp. 107-118.

Sideris, M.G. (1990). Rigorous gravimetric terrain modelling using Molodensky's operator. *Manuscripta Geodaetica*, 15, No. 2, pp. 97-106.

Sideris M. G. and I. N. Tziavos (1988). FFT-evaluation and applications of gravity-field convolution integrals with mean and point data. *Bulletin Géodésique*, 62, No. 4, pp. 521-540.

Sideris M. G. (1987). Spectral methods for the numerical solution of Molodensky's problem. UCGE Report No. 20024, PhD thesis, Department of Geomatics Engineering, University of Calgary, Calgary, AB, Canada.

Sideris M. G. and K. P. Schwarz (1986). Solving Molodensky's series by fast Fourier transform techniques. *Bulletin Géodésique*, 60, pp. 51-63.

Sideris M. G. (1984). Computation of gravimetric terrain corrections using fast Fourier transform techniques. UCSE Reports, No. 20007, M.Sc. Thesis, University of Calgary, Calgary, Alberta, Canada.

Soltanpour A., H. Nahavandchi, and W. Featherstone (2006). The use of second-generation wavelets to combine a gravimetric quasigeoid model with GPS-levelling data. *Journal of Geodesy*, 80(2), pp.82-93.

Strang van Hees G. (1990). Stokes formula using fast Fourier transform techniques. *Manuscripta Geodaetica*. 60, pp. 51-63.

Strang G. (1989). Wavelets and dilation equations: A brief introduction. *Society for Industrial and Applied Mathematics (SIAM) Review*, 31(4), pp. 614-627.

Torrence C. and G. P. Compo (1998). A practical guide to wavelet analysis. *Bulletin of the American Meteorological Society*, 79, pp. 61-78.

Vaníček P. and N. Christou (1994). *Geoid and its geophysical interpretations*. CRC Press, Boca Raton, Florida, USA.

Wei M. and K. P. Schwarz (1998). Flight test results from a strapdown airborne gravity system. *Journal of Geodesy*, 72, pp. 323-332.

Wu L. (1996). Spectral methods for post processing of airborne vector gravity data. M.Sc. Thesis, UCGE Report #20104, Department of Geomatics Engineering, University of Calgary, Calgary, Canada.